Development of a parameter identification strategy using Finite Element Model Updating on Digital Image Correlation measurements : towards the application to a non-local model

Francesco Bettonte

THÈSE DE DOCTORAT

de l'Université de recherche Paris Sciences et Lettres
PSL Research University

Préparée à MINES ParisTech

Development of a parameter identification strategy using Finite Element Model Updating on Digital Image Correlation measurements: towards the application to a non-local damage model

Développement d'une stratégie d'identification des paramètres par recalage de modèle éléments finis à partir de mesures par corrélation d'images: vers l'application à un modèle d'endommagement non local

École doctorale n°432
SCIENCES ET MÉTIERS DE L'INGÉNIEUR

Spécialité SCIENCE ET GÉNIE DES MATÉRIAUX

COMPOSITION DU JURY :

Mme Véronique DOQUET
Président du jury
Laboratoire de Mécanique des Solides

Mme Anne-Sophie CARO
Rapporteur
Centre des Matériaux des Mines d'Alès

M. Marc GEERS
Rapporteur
TU Eindhoven

M. Jean-Noël PÉRIÉ
Examinateur
Institut Clément Ader

M. Jacques BESSON
Examinateur
Centre des Matériaux Mines ParisTech

Mme Sylvia FELD-PAYET
Examinateur
ONERA

M. David LÉVÊQUE
Invité
ONERA

Soutenue par **Francesco BETTONTE**
le 13 novembre 2017

Dirigée par **Jacques BESSON**
Encadrée par **Sylvia FELD-PAYET**

MINES ParisTech | PSL RESEARCH UNIVERSITY PARIS

À tous ceux qui font de la curiosité la clé de leur réussite.

Remerciements

Ce manuscrit rassemble le travail de ces trois dernières années de thèse. Bien que j'en sois l'auteur, cette réussite n'aurait pas été possible sans le support et la collaboration de nombreuses personnes, que je souhaite remercier ici.

Je remercie les membres du jury, pour avoir examiné mon travail et mené une discussion intéressante au cours de la soutenance. Merci en particulier à Marc Geers et Anne-Sophie Caro pour avoir accepté le rôle de rapporteur.

Je tiens ensuite à remercier infiniment mes encadrants Sylvia, Jacques et David, pour m'avoir accompagné tout au long de ce parcours, mais aussi pour m'avoir soutenu dans mes décisions. J'ai pris un vrai plaisir à travailler à leur côté. Je n'oublierai jamais la confiance qu'ils m'ont accordée en me choisissant pour cette mission quand l'apprentissage de la langue française aurait pu être considéré comme un frein. J'ai aussi un remerciement particulier pour Jean-Didier, qui a véritablement été mon Virgile de la programmation informatique. Merci pour tous ses conseils et nos discussions autour d'un café. Merci également à Yves et Guy, pour leur aide précieuse dans le domaine du traitement d'images.

Merci à tous mes collègues du bâtiment E4 à l'ONERA, pour leur sympathie et leurs remarques de qualité sur mon travail au cours des différentes présentations. Je remercie également mes collègues doctorants, à l'ONERA comme au du Centre des Matériaux, pour leur bonne humeur.

Merci à mes parents et ma famille, pour m'avoir toujours encouragé dans mes études, et pour tous leurs efforts pour me permettre de réussir jusqu'ici. Je remercie de la même manière Martine et Patrick pour m'avoir accueilli et m'avoir aidé à démarrer ma vie en France. Enfin et surtout, je tiens à remercier ma petite amie, Audrey, de m'avoir soutenu inconditionnellement pendant ces trois années.

TABLE OF CONTENTS

INTRODUCTION

General context

The use of numerical simulation into the industrial domain allows both to fasten the product development process and to reduce the prototyping costs. As a transfer institute, ONERA[1], the French aerospace lab, has notably the mission of developing accurate numerical models for the simulation of damage and fracture. In particular, a recent research axis has been the development of regularized damage models. Their use is essential to the correct simulation of the softening behaviour of a structure. Indeed, regularization allows to overcome the well known problem of spurious localization with standard finite element formulations. This problem has been tackled notably through the doctoral works of Germain [49] and Feld-Payet [44], which mainly focused on the numerical aspects. In parallel, the doctoral works of Cuvilliez [35] and Zhang [136] were carried out at Electricité de France (EdF R&D), addressing more the constitutive behaviour aspects. The present work is complementary to the mentioned theses. It aims at investigating the identification of the regularized model parameters.

It is possible to find within the literature several references aiming at characterizing damage models. However, the majority of applications concerns local damage models and so, the identification leads to results specific to a particular mesh. Moreover, in most cases the identification is based on punctual or macroscopic measurements, without using the potential of modern measurement techniques, as Digital Image Correlation (DIC), which provide full-field measurements. The interest of full-field measurements for the identification of damage resides in the possibility to measure phenomena occurring at a relatively small scale, as in the localization band. Furthermore, full-field measurements can be used to drive a finite element simulation by prescribing measured displacements as boundary conditions, ensuring a consistent comparison between simulation and experiment. Advanced techniques as the Integrated Digital Image Correlation (I-DIC) use a finite element mesh to perform the digital image correlation while ensuring the consistency of the result with an associated constitutive models. But in the present study, the idea is to work on DIC results previously obtained, independently of any assumption on the behaviour, by any DIC software algorithm.

This study is part of the 4-years long project PRF MECHANICS at ONERA, which aims at improving the dialogue between experiment and simulation by means of image analysis. The objective of this project is to build a modular software platform, called *escale*, dedicated to the dialogue between experiments and simulations. Thanks to the flexibility of the Python language, the platform provides a practical interface which allows the communication through NumPy data exchanges between DIC codes, finite element problem solvers and optimization algorithms.

[1] Office National d'Etudes et Recherches Aérospatiales

Objective

The objective of this study is to propose a robust strategy for the characterization of plastic behaviour and damage up to the onset of fracture. The strategy uses both load and DIC measurements. It is developed into a non-local damage framework. The identification is carried out considering a FEMU technique, according to which the parameters are identified by minimizing the discrepancy between the experimental measurements and their simulated counterparts, issued of a finite element model representative of the tests in terms of geometry and boundary conditions. Although several applications of FEMU for the characterization of a mechanical model can be found within the literature (see chapter 4), the novelty of this study consists in the complex context of application: the ductile failure process. Indeed, the large deformations involved are challenging both for the measurement system and for the finite element simulation, which are run up to the onset of failure. To assess the validity of the approach, the technique is applied to perform parameter identification on relatively simple specimens, and the parameters are used to simulate the response of complex geometries, which are then validated by comparison with the experimental responses.

Numerical tools

The DIC results are obtained by means of an efficient stereo correlation algorithm, FOLKI-D developed at ONERA [76]. Beyond the performances of the GPU implementation, the choice of FOLKI-D is motivated by the possibility of interacting with its developers to adapt the code in a relatively short delay. In fact, thanks to the necessities of parameter identification, the DIC software has been improved on several occasions.

The Finite Element results are obtained by means of Zebulon, an implicit solver co-developed by the École des Mines and ONERA. The finite strain formulation and the damage model are completely inherited from the PhD work of Zhang, mentioned above. It had been implemented within Zebulon at the beginning of the PhD and has been tested thanks to the identification needs.

The FEMU technique itself is implemented within *escale*. The development of *escale* was parallel to this thesis (no prior implementations of FEMU were available). Furthermore, the development of FEMU required the development of both the DIC and FE interfaces. Figure 0.1 illustrates the graphical interface of the platform, resulting from 3 years of developments, together with a significant result issued from the dialogue between experiment and simulation.

Approach of the thesis

Although the present work intends to provide a general approach for parameter identification applicable to any ductile metal undergoing large deformations, a unique material is considered in this work: the nickel-based superalloy Inconel 625. Ten different geometries (axisymmetric and flat) are selected to perform tensile tests, which are described in chapter 1. The choice of the geometries aims at obtaining heterogeneous displacement fields, in order to collect a maximum of information from Digital Image Correlation measurements. The selected geometries are tested up to failure, to create an experimental database adapted to the developments of this work.

The plastic behaviour of Inconel 625 is modelled using an Hosford yield criterion and a Voce-like isotropic hardening law, while damage evolution is modelled using a GTN damage model. The

finite element formulation is defined within the finite strain framework, considering a locking-free regularized formulation. Globally, the simulation of Inconel 625 relies on 16 parameters, including the regularization parameter of the non-local model, described in chapter 2.

The consistency of the comparison between experiment and simulation is ensured by the application of measured displacements as boundary conditions for the finite element problem, imposing the real kinematics of the deformation. However, the measured displacements need to be filtered, since the measurement uncertainty distorts the finite element solution, as described in chapter 3. An innovative filtering technique based on the Robin boundary condition is proposed and tested together with classical filtering approaches, as the moving least squares and polynomial approximations.

The discrepancy between experiment and simulation is quantified by means of a cost function, as described in chapter 4. The cost function, which represents the core difference between alternative FEMU approaches, is chosen to minimize both displacement and load. This is possible thanks to a proper normalization of each term. Before trying to minimize this cost function to identify the parameters, a preliminary sensitivity analysis is performed to determine a priori the feasibility of the identification by FEMU. Indeed, there might be a possible interaction between the parameters, leading to an indetermination on the result. The details of this analysis are presented in appendix E for both the plasticity parameters and the damage parameters.

Finally, the proposed identification approach is used to identify the GTN parameters on a flat geometry, as detailed in chapter 5. The resulting set of parameters is then used to obtain satisfactory simulations up to the onset of fracture for different geometries, confirming the validity of the approach.

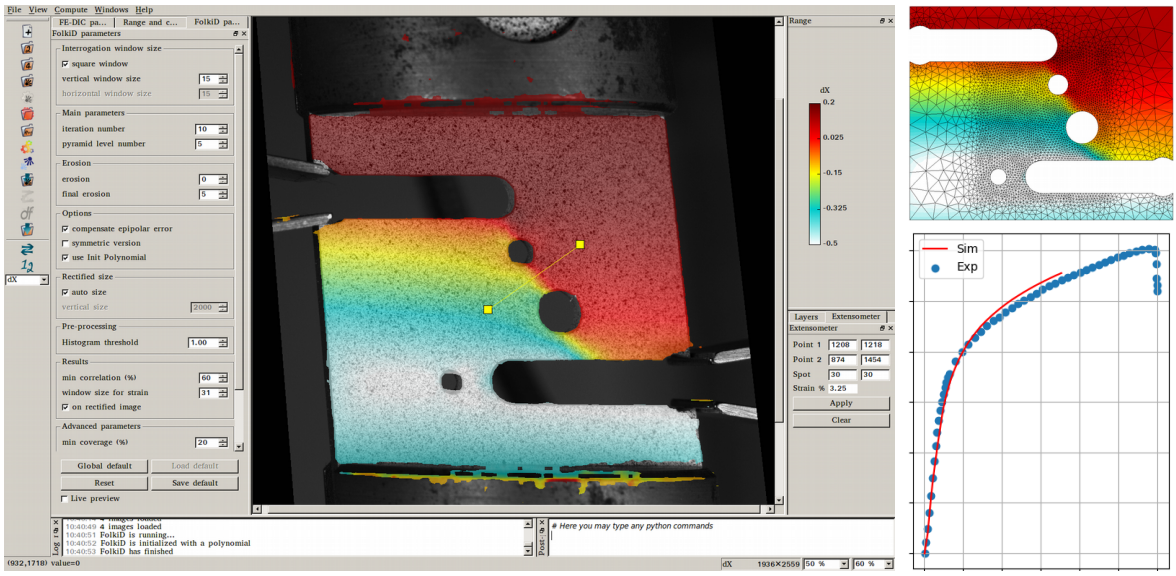

Figure 0.1: The image shows 3 synchronized results: a DIC displacement field (left image) and its simulated counterpart obtained by prescribing measured displacements as boundary conditions on the top and bottom edges of the mesh (top right image), plus a comparison between the experimental force versus time curve and the simulated one (bottom right image) issued from a set of optimized parameters (see chapter 5).

Résumé

L'utilisation de la simulation numérique dans le domaine industriel permet d'améliorer le processus de développement, ainsi que de réduire les coûts de prototypage. L'ONERA, en tant qu'institut de transfert, a pour mission le développement de modèles numériques prédictifs pour la simulation de l'endommagement et de la rupture. Les thèses menées au cours de la dernière décennie se sont intéressées à la modélisation de l'endommagement dans un formalisme régularisé.
L'objectif de cette thèse, complémentaire aux précédentes, est de développer et mettre en œuvre une approche d'identification des paramètres pour un modèle d'endommagement régularisé. Cette approche utilise à la fois les efforts et les mesures de champ denses issues de la corrélation d'images. L'idée est d'utiliser la richesse des informations de ces mesures afin d'identifier des paramètres dont l'influence sur une structure est locale. L'approche d'identification proposée est fondée sur le recalage de modèle éléments finis (FEMU): les paramètres sont identifiés en minimisant l'écart entre une mesure expérimentale et son pendant simulé.
Bien que la méthode proposée soit applicable à divers matériaux, les travaux présents ont été réalisés sur l'alliage Inconel625. Les essais effectués ainsi que le choix des géométries sont illustrés dans le premier chapitre. Le deuxième chapitre est dédié à la modélisation du comportement et à la formulation éléments finis, choisis afin de reproduire le comportement observé expérimentalement. Le troisième chapitre introduit le dialogue essai-calcul. Sa fiabilité est garantie par l'application des déplacements mesurés comme conditions au bord pour le calcul éléments finis. Le chapitre met en évidence les problèmes issus de l'utilisation d'une donnée polluée par l'incertitude de mesure, et compare différentes techniques de filtrage. La méthode d'identification est clairement développée dans le quatrième chapitre et elle est appliquée pour l'identification des paramètres plastiques afin d'être validée. Enfin, le cinquième chapitre montre une application de la stratégie FEMU pour l'identification des paramètres d'endommagement.

CHAPTER 1

MATERIAL AND EXPERIMENTAL METHODS

This chapter describes the experimental procedure and results that support the present PhD work. Parameter identification is performed using a FEMU technique on a set of tensile tests carried out at room temperature. The considered material, together with the motivations for its choice, are discussed in section 1. The kinematic full-field measurement considered in this work, are obtained using the Digital Image Correlation (DIC) technique described in section 2. The key point of the present work is the utilization of full-field measurements. In fact, they allow both to consider non-standard specimens for the characterization of the material and to get access to local variations of the kinematic response, such as those provoked by the damage phenomena. Hence, full-field measurements permit the identification of damage parameters, as done in [23, 110]. Moreover, the accuracy of the identification via FEMU is increased considering heterogeneous kinematic measurements as input for the inverse problem [7, 60]. Thus, the selection of the specimens geometry is an important phase, since the required kinematic heterogeneity is originated by means of geometrical heterogeneities such as notches and holes. Several works within the literature are focused on the determination of the more suitable geometries for parameter identification which maximize the heterogeneity of the kinematic fields (*e.g.* see [31, 37]). The choice of the geometries for the present tests is discussed in section 3, where the works of Dournaux [37] and Tanguy [126] are considered as guidelines. Finally, a micro-graphic analysis at the Scanning Electron Microscope (SEM) is performed on some selected specimens to evaluate the rupture mechanisms and to quantify the initial void volume fraction. The results are presented and discussed in section 4.

1.1 Material

Although the present work intends to provide a general approach for parameter identification applicable to any ductile metal undergoing large deformations, a unique material is considered in this work: the nickel-based superalloy Inconel 625. This alloy was developed in the early 1950's to satisfy a growing demand for high-strength piping material [39]. Since then, thanks to some modifications of the chemical composition, the domain of application has been extended to the marine, nuclear and aerospace industry. The main characteristics of this material, which

motivated its choice as the reference material for this thesis, are the high tensile strength and the high deformation at break. Moreover, Inconel 625 shows also an high resistance to oxidation, which is here an advantage to perform fractographic analysis. Appendix A reports the chemical composition of the considered alloy and illustrates the microstructure.

1.2 Digital Image Correlation

Several techniques for measuring full-field kinematic fields (*e.g.* displacement) have been proposed in the literature during the last decades. Their main difference relies on the physical phenomena involved into the measurement approach. References [51, 54] provide an extended review of such techniques. The present work considers Digital Image Correlation (DIC), a white light technique, developed since the early 70s, which is becoming a standard tool in experimental mechanics [134]. In particular, the present work is concerned with local DIC methods, which provide a measure of the displacement fields without any assumption on the kinematics (as done for global DIC methods). The principle of image correlation is quite intuitive to understand. It consists in identifying the displacement of a deforming object by measuring the variation of light flow (the gray-level) between two consecutive images. It comes down to an optimization problem that is solved subset by subset (see figure 1.1). Thus, the object into the image should be characterized by a recognizable pattern. For this reason, metallic tensile test specimens (which are generally bright and smooth) are painted to generate a random speckle as in figure 1.1. The matching

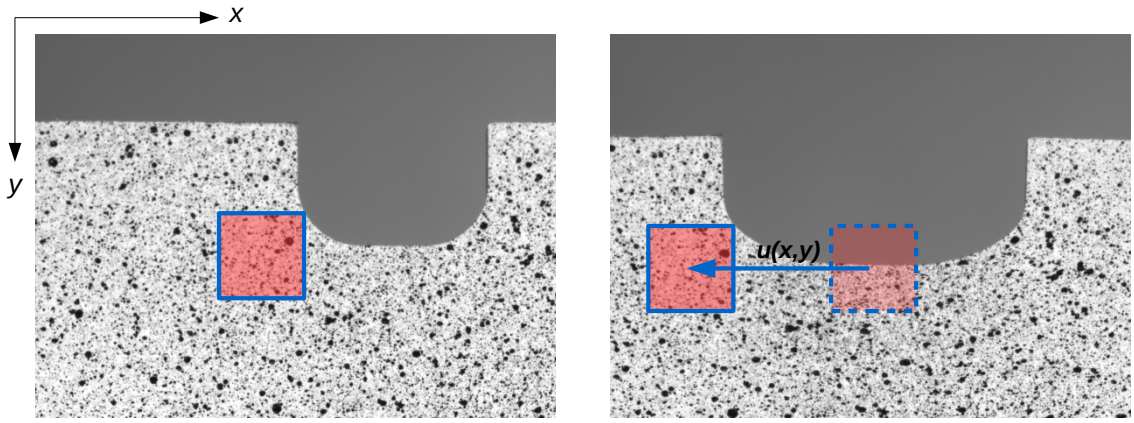

Figure 1.1: Principle of image correlation. The considered subset is the the red square. The measurement problem is solved when the pattern of all the subsets in the reference images is recognized within the deformed image (matching).

process is usually guided by a correlation measure, also referred to as *score*. A simple score would be the Sum of Squared Differences (SSD) which is the squared norm of the vector made by collecting the differences of gray-level between the pixels of each subset. Many references, as [105], use more robust scores, such as the Zero-centered Normalized Cross Correlation (ZNCC) to account for uncontrolled variations of the gray-scale level between images, for instance due to a difference of illumination. The measured displacement is then obtained by an optimization

process on the score (maximization or minimization depending on the chosen score). Several algorithms have been proposed for this optimization, which is an important computational burden considering the large images available nowadays. The image correlations of the present work are carried out using a correlation algorithm developed at ONERA, referred to as FOLKI-D[1] [76]. It is derived from a previously published algorithm for Particle Image Velocity (PIV), which in turn is derived from an algorithm for optical flow estimation [75]. The choice of FOLKI-D is motivated by the following (unordered) reasons:

- no post-filtering operations are carried out;
- the result is dense: displacement is estimated for each pixel of the image;
- the algorithm is well suited for parallel computation: the GPU implementation available within the *escale* platform at ONERA allows fast and accurate computing;
- the use of a non commercial software allows an ongoing development of the software and a better management of each step;
- the level of uncertainty of the measurement is generally low [76].

There are some major particularities that distinguish FOLKI-D from other correlation algorithms. In fact, only translation is considered as motion model between pixels. This might seem an heavy restriction, but the dense computation carried out allows to bypass the problem, leading to measure complex movements, as rotations, with a satisfactory accuracy [76]. Furthermore, FOLKI-D does not rely on an exhaustive research for the optimum, which would require a large number of score evaluations, often accelerated by FFT (Fast Fourier Transformation) in other algorithms. Instead, the score function is considered as a surface and a minimum (or maximum) is searched via a gradient-based approach. Furthermore, FOLKI-D uses a coarse-to-fine strategy based on a pyramid of images to avoid the optimization to stop on local minima (see figure 1.2). Starting from the original image (the largest one of the pyramid) low-pass filtering and downsampling is performed to obtain smaller images. The downsampled images form the levels of the pyramid. The first estimation of the displacement field is done at the highest level of the pyramid (smallest image), considering a null displacement as initialization. Afterwards, the previous displacement estimation is expanded (upsampling) and used to initialize the correlation at the lower level of the pyramid. This latter process is repeated until the lowest level (the original image) is reached. Further details about FOLKI-D and its parallel implementation are given in [76].

Measuring large displacements The subset matching is a local operation. Hence, in case the difference between the images is too important, the correlation might not succeed. However, the coarse-to-fine strategy native of FOLKI-D allows to estimate large displacements since the difference between the images at the top level of the pyramid is considerably reduced (of a factor $2^{(n-1)}$, where n is the number of levels of the pyramid). Thus, large displacements at the bottom level are seen as relatively small displacements at the top level.

Nevertheless, the coarse-to-fine strategy might still not be enough for very large displacements. This is the case for the current work. The solution to overcome this problem is to update the reference image (the zero load image) with an intermediary one and to perform an intermediary

[1] FOLKI is a French acronym for Iterative Lucas-Kanade Optical Flow.

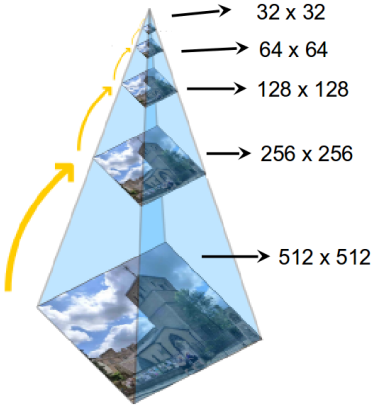

Figure 1.2: Pyramid of images. Starting from the lower level of the pyramid (the original image) the higher levels are obtained obtained by downsampling the image of the previous level. Once the pyramid is created, the correlation begins at highest level (the smallest image) and the result of each level is used to initialize the correlation at the lower level of the pyramid, until the bottom is reached.

correlation. Afterwards, this latter result is combined with the previous ones in order to obtain a Lagrangian description of displacement. However, the combining operation involves interpolation of data and so, it might be a source of errors. Therefore, it should be used only when necessary, *i.e.* when a direct correlation would not work. In order to assess the error introduced by the combining operation, the resulting DIC displacements have been compared with the displacements measured by a calibrated extensometer. A smooth cylindrical specimen was considered for this operation. Figure 1.3 shows that the relative error in the worst case scenario (the combining operation is performed for each image step) is lower than 1.2%.

Quality of the measure The quality of the measured displacement fields can be assessed using by-products of the FOLKI-D iteration. A first indicator is the final score coefficient, which is related to the validity of the matching operation. A correct matching indicator in experimental mechanics should be higher than 90%. A second indicator of the precision is the standard deviation, or uncertainty, of the displacement field. It can be computed using the final Hessian of the optimization procedure and the variance of the residual image, as described in [76]. Many factors influences the uncertainty, as the illumination or the distance of the specimen from the camera. However, the average uncertainty of the measures carried out during the present work is of the order of $\pm 1 \mu m$ for the in-plane displacements and $2 \mu m$ for the out-of-plane displacements.

Stereoscopic DIC Stereo DIC is used in the present work. In stereo DIC two images are recorded at each instant. Thanks to the geometrical calibration, conducted using the AFIX2 software available at ONERA [77, 78], the FOLKI-D algorithm is used to compute the disparity map, for each each time step. The disparity allows to reconstruct the 3D surface of the sample and also to project the images of the second camera onto the pixel grid of the first camera to perform a temporal correlation afterwards.

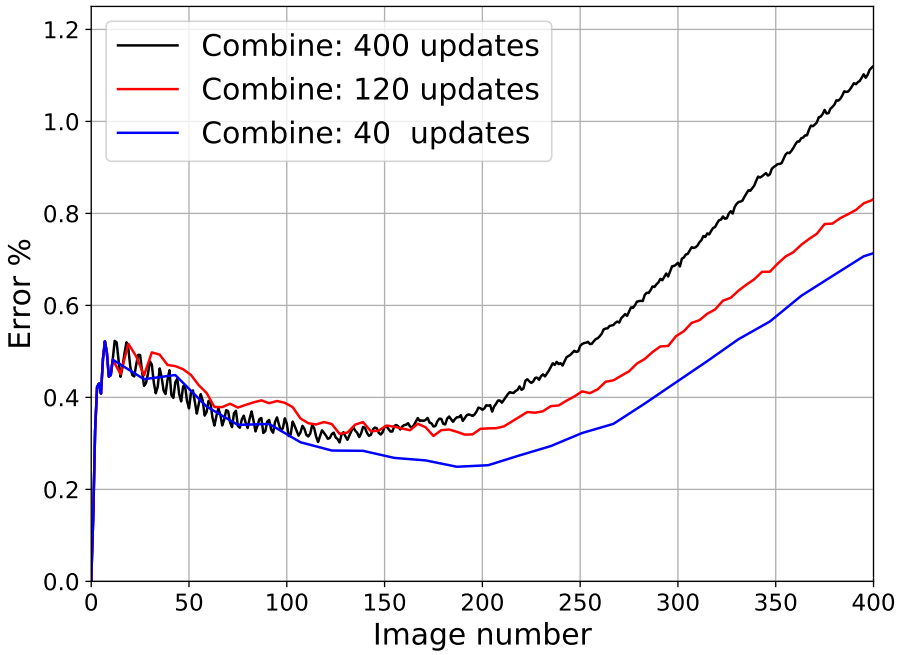

Figure 1.3: Evaluation of the error introduced by the combining operation. The reference image has been updated in different ways from an update at each step (400 for 401 images), unreasonable and unnecessary, to a more reasonable value (40 for 401 images). The relative error has a maximum value of around 1.2% for the worst case scenario.

1.3 Choice of the specimens geometries and test conditions

As introduced, the main guideline for the selection of the specimens geometries should be the level of heterogeneity of the kinematic fields. Furthermore, the stress triaxiality level should be taken into account while studying ductile failure, since it drives damage evolution [126, 135]. Therefore, the mechanical tests are here carried out on various geometries inspired from the previous works of Dournaux [37] and Tanguy [126]. Four flat geometries and four cylindrical geometries are retained. Nevertheless, flat (and relatively thin) specimens represent here the preferred choice to perform damage parameter identification from full-field measurements. Indeed, for flat specimens, it is possible to suppose the mechanical fields (and in particular the stress triaxiality) constant along the thickness direction. Hence, what is measured on surface by DIC is representative of the response at the specimen's core. However, cylindrical specimens are often used to study ductile failure [126] and including them in the present work allows to compare the results with previous works.

1.3.1 Selected geometries

The considered geometries are referred to by means of abbreviations which indicate their shape and notch severity. Notations **C** and **P** indicates whether the specimen is axisymmetric or flat, respectively. Notations **SMOOTH**, and **AE** indicates whether the specimen is smooth or notched, respectively. Finally, a number indicates the severity of the notch. Such a value is to be considered

as a relative quantity rather than an absolute one. One flat specimen differs considerably from the other since it induces a plain strain condition, and will be referred to as **PDP**. The sketches are reported in figures 1.4, 1.5 and 1.6. The dimension of the geometries has been computed by scaling and adapting the original dimensions to the 30 mm round bar available.

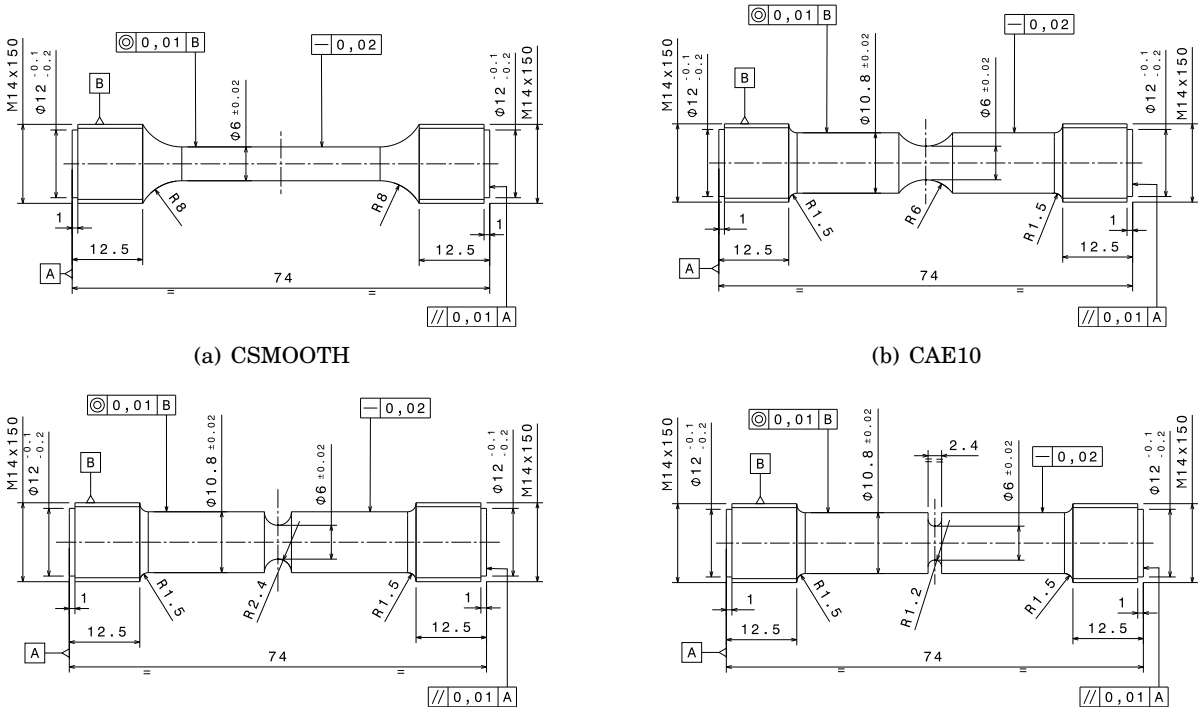

(a) CSMOOTH

(b) CAE10

(c) CAE4

(d) CAE2

Figure 1.4: Axisymmetric geometries, inspired from reference [126]. All the geometries have the same cross section area. They allow to study ductile failure because of the high stress triaxiality level reached at core. Cracks propagate from the core towards the surface.

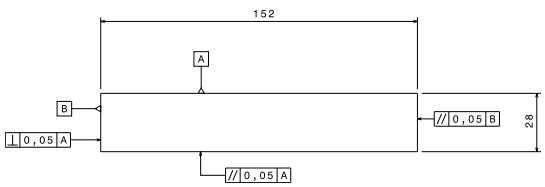

(a) PSMOOTH

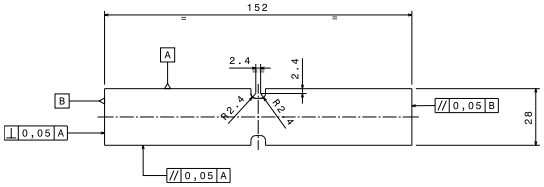

(b) PAE2

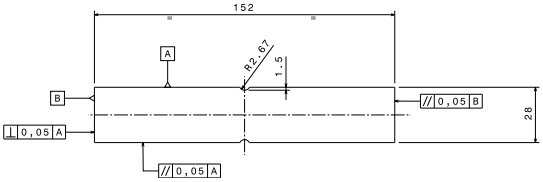

(c) PAE1

Figure 1.5: Flat geometries, inspired from reference [37]. All specimens are 2 mm thick. Flat specimens are characterized by a lower stress triaxiality level compared to the axisymmetric geometries, but it can be supposed constant along the thickness direction. Cracks propagate from the notches towards the center.

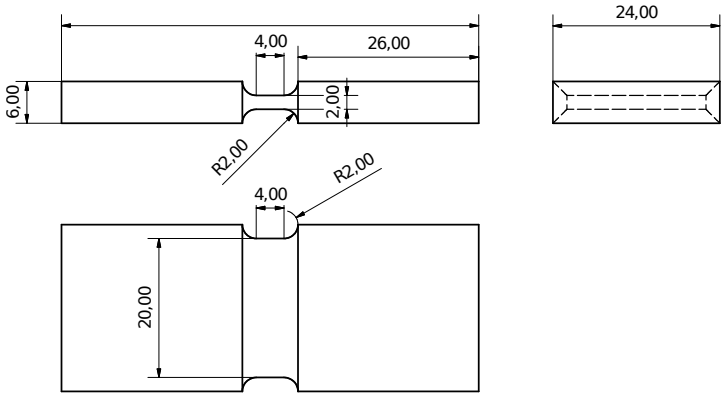

Figure 1.6: PDP Plain strain geometry, inspired from reference [126]. Cracks propagate from the center towards the notches.

1.3.2 Experimental procedure and setup

Two identical cameras, which characteristics are summed up in table 1.1, where placed in front of each specimen to realize a stereoscopic vision system, that is visible in figure 1.7. The speckle on the specimens was realized by means of an airbrush, rather than a spray bomb, in order to avoid the splintering of the paint because of an incohesive paint layer.

All the mechanical tests were performed at room temperature on servo-hydraulic testing machines. Specimens were monotonously loaded at various displacement rates that induced local strain rates within the range $10^{-3} - 10^{-4} s^{-1}$. In addition, specimens CSMOOTH-4 and PAE2-2 were equipped with a large strain extensometer and some elastic unloads were performed in order to observe a possible loss of stiffness due to damage. Image recording was synchronized with the testing machine data sampling by means of Mecanismes, a software developed at ONERA. Table 1.2 summarizes the performed tests and their respective loading conditions.

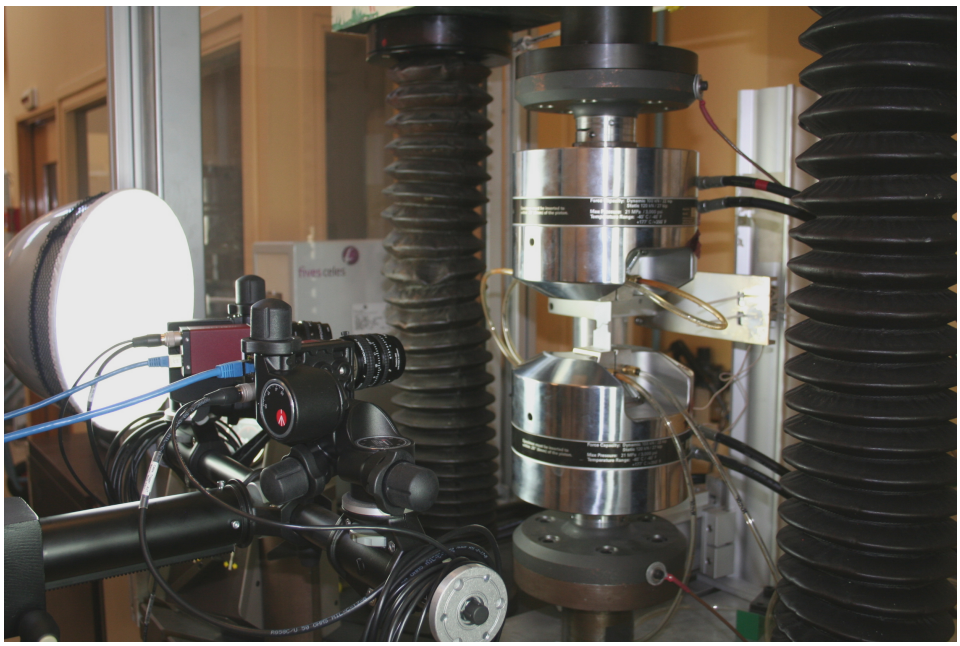

Figure 1.7: Experimental set-up for tensile tests. The 2 camera form the stereoscopic vision system, while the spot light ensures a constant light flow preventing erroneous correlations.

Camera	AVT MANTA G-235B
Sensor	CMOS
Resolution	1936×1216 pixels
Objective	Schneider-Kreuznach 50 mm
Dynamic range	8 bits

Table 1.1: Characteristics of the cameras used and their respective objectives.

Test			**Images**				**Machine**	
Geometry	Test number	Loading Rate mm/min - Mode	Sampling Hz	Integration ms	f mm	**f**	Name	Sampling Hz
Cylindrical Specimens								
C Smooth	1	0,8 - Monotonic	0,1	50 - 60	50		MTS 810	2
C Smooth	2	0,8 - Monotonic	0,2	50 - 60	50		MTS 810	2
C Smooth	3	5 - Monotonic	1	70	50		MTS 810	50
C Smooth	4	5 - Cycle 5 mm + 7 x (0,15 mm unload + 2 mm load)	1	70	50		MTS 810	50
C AE10	1	0,8 - Monotonic	0,3	50 - 60	50		MTS 810	2
C AE10	2	0,08 - Monotonic	0,2	50 - 60	50		MTS 810	2
C AE10	3	0,8 - Monotonic	1	50 - 60	60		MTS 810	10
C AE4	1	0,04 - Monotonic	0,2	50 - 60	50		MTS 810	2
C AE4	2	0,04 - Monotonic	0,2	50 - 60	50		MTS 810	2
C AE2	1	0,4 - Monotonic	0,5	50 - 60	60		MTS 810	10
C AE2	2	0,4 - Monotonic	1	50 - 60	60		MTS 810	10
Flat Specimens								
P Smooth	1	2 - Monotonic	1	50 - 60	50	f/4	LOS	10
P AE1	1	1,2 - Monotonic	0,5	50 - 60	50	f/4	LOS	10
P AE1	2	1,2 - Monotonic	0,5	50 - 60	50	f/4	Instron 5582	10
P DP	1	1,2 - Monotonic	1	50 - 60	50	f/4	LOS	10
P AE2	1	1,2 - Monotonic	0,5	50 - 60	50	f/4	LOS	10
P AE2	2	0,5 - Cycle 3 x (2 mm load + 0,2 mm unload)	1	50 - 60	50	f/4	LOS	10
P AE2	3	1,2 - Monotonic	0,5	50 - 60	50	f/4	MTS 810	10

Table 1.2: List of the tensile tests carried out. Some of the tests included a fixed number of elastic unloads to investigate damage evolution. The prescribed displacement rate induces a local strain rate within the range $10^{-3} - 10^{-4} s^{-1}$.

1.4 Experimental Results

The purpose of this section is to provide a first analysis of the tensile tests. The objective is to understand the behaviour of Inconel 625 to develop the identification protocol.

1.4.1 Identification of the elasticity parameters

The identification of the elasticity parameters, *i.e.* the elastic modulus and the Poisson's ratio, is not performed using FEMU in this study, although FEMU has already been successfully used for such a task [79, 121]. Therefore, the camera trig frequency was adapted for the plasticity and damage phenomena (see table 1.2), to concentrate the effort on the identification of the plasticity and damage parameters. The modulus of elasticity was measured by considering two of the tests on axisymmetric cylindrical specimens (CSMOOTH-2 and CSMOOTH-3). To do so, a small strain extensometer was used. The procedure involved 6 load cycles for each specimen (within the elastic regime). Three cycles were performed in displacement control (loading at a 0.8 mm/min rate up to an elongation of 0.08 mm) while the other three cycles were performed in load control (loading at a 0.85 kN/s up to an force of 5 kN). For each cycle, the elastic modulus were estimated by fitting a linear model (see figure 1.8) by means of the RANSAC[2] (random sample consensus) algorithm [45]. Finally, the average value of the 6 cycles was retained. The Poisson's

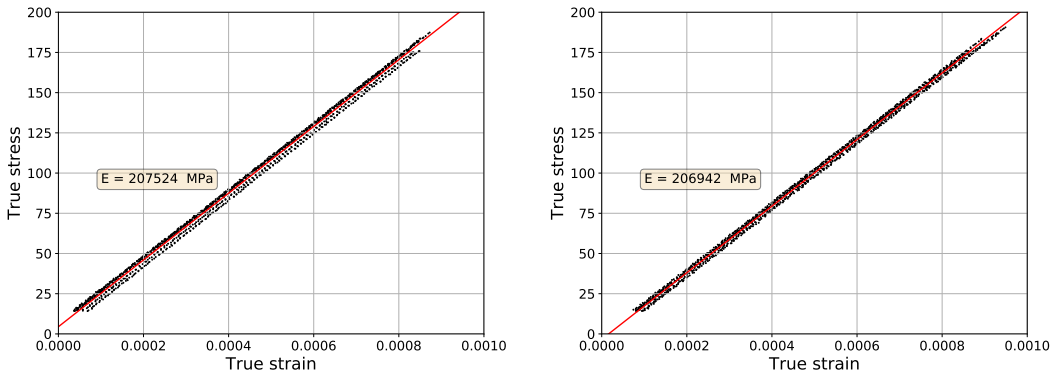

(a) CSMOOTH-2 (b) CSMOOTH-3

Figure 1.8: Stress versus strain response of 6 cycles within the elastic range.

ratio was simply taken from the literature [1] since it has a negligible effect on the plasticity and damage phenomena. Table 1.3 reports the considered value for the elasticity parameters.

Young's modulus E	Poisson's ratio ν
207 GPa	0.308

Table 1.3: Elastic properties of Inconel 625 at room temperature. Young's modulus is measured while the Poisson's ratio is taken from the literature.

[2]The RANSAC algorithm is used to exclude the experimental outliers from the optimization.

1.4.2 Analysis of the macroscopic response

The analysis of the macroscopic response provides information about the experimental scattering and any possible viscosity effect. Furthermore, damage could be quantified if a considerable variation of stiffness is measurable.

The large strain extensometer applied on specimens 3 and 4, together with a virtual extensometer for specimen PSMOOTH-1, provides the stress-strain curves of figure 1.9.

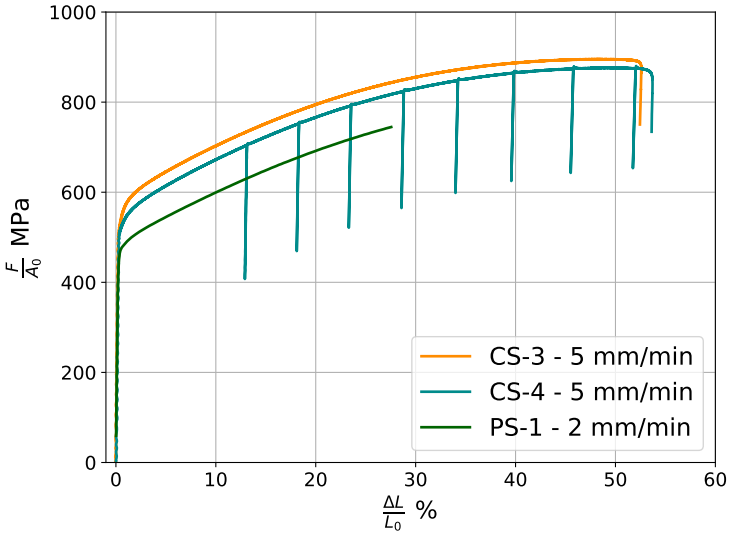

Figure 1.9: Tensile test response (stress versus strain) of smooth specimens. The experimental scattering due to the inhomogeneity of the raw material bars is considerable (the maximum discrepancy values approximatively 100 MPa).

Inconel 625 at the annealed state shows high deformation at break (over 50 %) at room temperature, a considerable hardening and a clear experimental scattering. Figure 1.10 shows the macroscopic responses of the axisymmetric specimens while figure 1.11 shows the macroscopic responses of the flat specimens. Let us first note that the experimental scattering observed on the smooth specimens is confirmed with the notched specimens. In fact, there is an obvious lack of repeatability of the experimental response for a test carried out twice (or more) at the same loading rate. A possible explanation of this scattering is that the various specimens comes from different slices of the original raw bar, for which the mechanical properties might be locally different. The second remark is about the viscous effect, which appears to be negligible at room temperature for the tested loading rates. In fact, as visible in figures 1.10(b) and 1.9, the same test carried out at different loading rates (of a factor 10 and 6 respectively) does not induce a significantly different macroscopic response. Let us observe that the number of tests performed is not high enough to precisely quantify the experimental scattering or to assess any viscous effect, which is not the purpose of the present work.

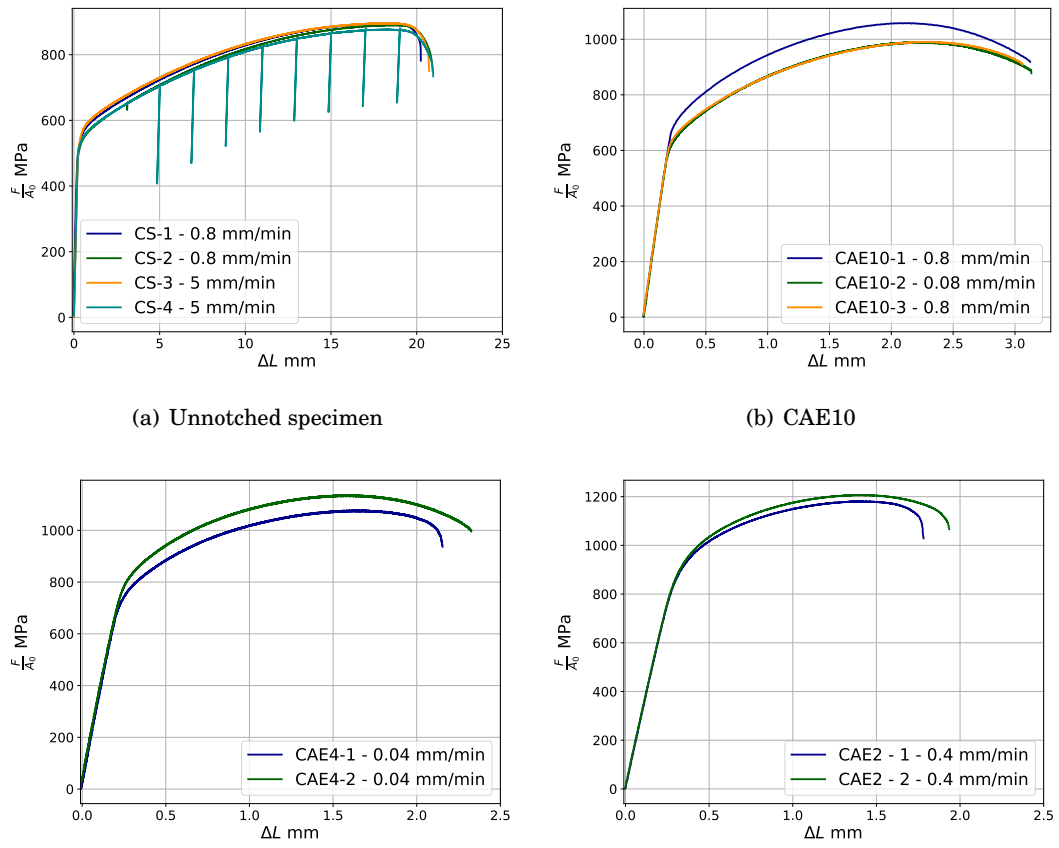

(a) Unnotched specimen

(b) CAE10

(c) CAE4

(d) CAE2

Figure 1.10: Mechanical response of the axisymmetric specimens. There is a observable lack of repeatability of the tests, especially within the plastic regime, and no evident viscous effects.

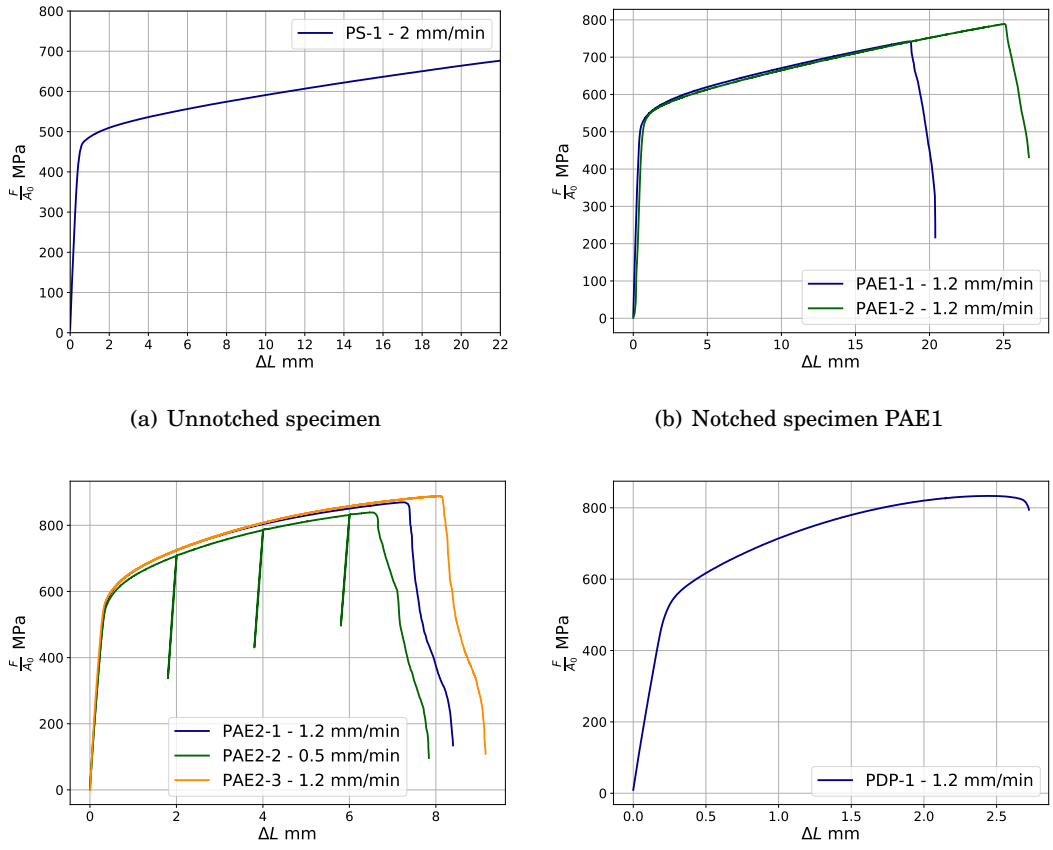

(a) Unnotched specimen

(b) Notched specimen PAE1

(c) Notched specimen PAE2

(d) Notched plain strain specimen PDP

Figure 1.11: Mechanical response of the flat and plain strain specimens. There is a remarkable scattering at failure. Let us note that the test on the smooth specimens was interrupted at a strain level of around 27% due to the machine maximum displacement restriction.

Measure of damage from loss of stiffness According to Lemaitre and Chaboche [81], any possible evolution of damage induces a loss of stiffness of the material. Therefore, the elastic unloads performed on test CSMOOTH-4 have been analysed. For each unload, the Young's modulus was calculated supposing a small perturbation. When analysing the loss of stiffness, it is important to distinguish the loss of stiffness of the material due to damage from the loss of stiffness of the structure due to the geometric change imposed by deformation (deformation causes a progressive reduction of the resistant section). This distinction is simply made by calculating the Young's modulus of the unloads respectively on the true and nominal stress-strain curve. Let us explicit the relations between nominal quantities and true quantities by means of the hypothesis of mass conservation, which is valid within the plastic regime. It will be shown that the stiffness of the structure decreases as a function of the nominal strain. In the following, notations ε indicates strain, notation σ indicates stress and suffix n indicates a nominal quantity. Notations S and l refers to the cross section and specimen's length respectively, while the suffix 0 denotes the initial value of the associated quantity. Hence, stress and strain are defined as:

$$\sigma_n = \frac{F}{S_0} \qquad \sigma = \frac{F}{S} \tag{1.1}$$

$$\varepsilon_n = \frac{\Delta l}{l_0} \qquad \varepsilon = \int_{l_0}^{l} \frac{1}{l}\,\mathrm{d}l = \ln\left(1 + \frac{\Delta l}{l_0}\right) \tag{1.2}$$

where imposing the mass conservation hypothesis $S_0 l_0 = S l$, it gives the following expressions for the actual length and the actual cross section:

$$l = l_0 + \Delta l = l_0(1+\varepsilon_n) \qquad S = \frac{S_0}{1+\varepsilon_n} \tag{1.3}$$

which, in turn, give the relations between nominal quantities and true quantities:

$$\varepsilon = \ln(1+\varepsilon_n) \qquad \sigma = \sigma_n(1+\varepsilon_n) \tag{1.4}$$

At this point, to obtain the relation between the nominal stiffness and the true stiffness it is necessary to explicit the response of the system to a small perturbation of strain $\delta\varepsilon = \frac{\Delta u}{l}$, supposing that it will induces a small perturbation of stress $\delta\sigma = \frac{\Delta F}{S}$:

$$E = \frac{\delta\sigma}{\delta\varepsilon} = \frac{\Delta F}{\Delta u}\frac{l}{S} = \frac{\Delta F}{\Delta u}\frac{l_0(1+\varepsilon_n)^2}{S_0} = \frac{\delta\sigma_n}{\delta\varepsilon_n}(1+\varepsilon_n)^2 = E_n(1+\varepsilon_n)^2 \tag{1.5}$$

hence, the structure's stiffness decreases, with respect to the material's stiffness, according to:

$$E_n = \frac{E}{(1+\varepsilon_n)^2} \tag{1.6}$$

Table 1.4 reports the stiffness for the performed unloads[3]. It is possible to note that while the nominal stiffness is decreasing because of the change of geometry, the true stiffness remains constant up to the last measured step. It means that it is not possible, in this case, to quantify damage by means of a variation of the elastic modulus. It may signify that failure happens mainly because of a strong late nucleation of voids.

[3]Let us note that the difference of the initial value with the previously measured value (see table 1.3) is to be attributed to the lack of precision for small increments of strain of the large strain extensometer used. However, the relative comparison between each unloads remains valid.

*	E MPa	E (nominal) MPa	ε_n [%]
Initial	192459	191791	0.1
Unload 1	189002	147572	13
Unload 2	188053	134126	18.2
Unload 3	189750	124061	23.4
Unload 4	189681	113738	28.7
Unload 5	189729	104995	34.1
Unload 6	190097	96863	39.7
Unload 7	190848	89481	45.6
Unload 8	191093	82350	51.9

Table 1.4: Elastic modulus for each elastic unload performed on the specimen CSMOOTH-4.

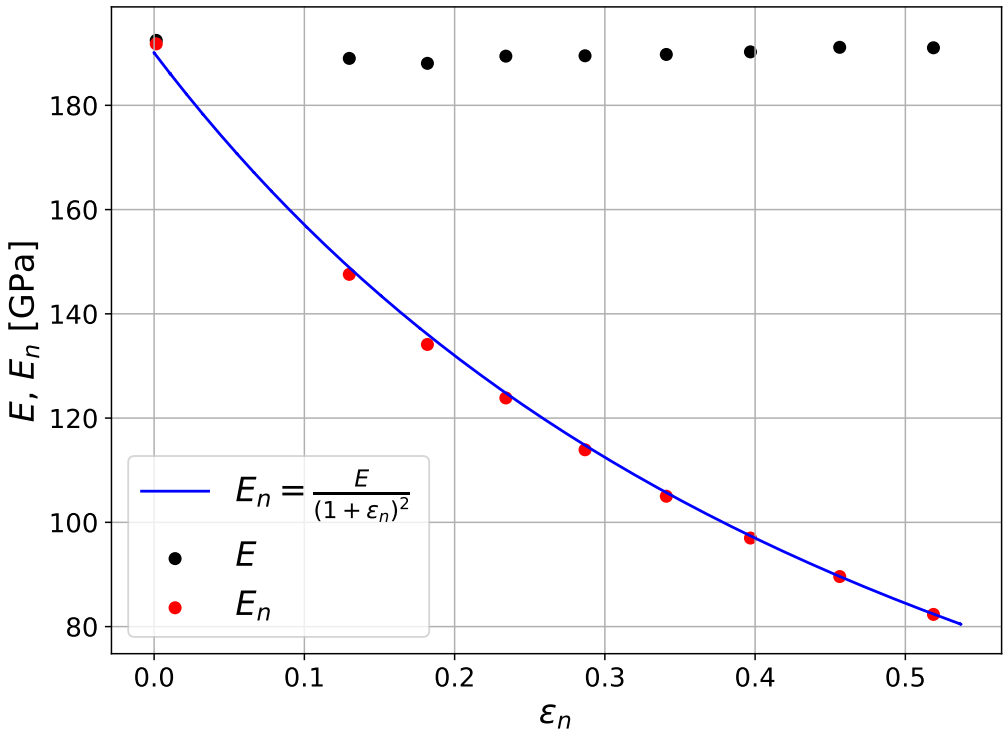

Figure 1.12: Evolution of the nominal elastic modulus (E_n) and true elastic modulus (E) versus the nominal strain level ε_n. There is no observable loss of stiffness of the material up to $\varepsilon \approx 52\%$, so that damage cannot be quantified in this manner. The apparent loss of stiffness showed by the nominal elastic modulus is attributed to the reduction of cross section due to deformation.

1.4.3 Microscopic analysis and initial void volume fraction

A part of the broken specimens was used to perform microscopic analysis. Both fracture surfaces and polished cross sections have been observed at the Scanning Electron Microscope (SEM). Fracture surfaces provide data about the rupture mechanisms, while cross sections allow to trace

the evolution of void volume fraction versus strain level. This latter analysis allows to determine an initial void volume fraction which is a key parameter for modelling damage evolution.

Fractography Let us begin the analysis with the fracture surfaces of CAE10-1 and CAE10-2, visible in figure 1.13. They show a cup cone surface typical of ductile metals [126]. Furthermore, the circular shape of the flat fracture zone confirms the isotropic behaviour of Inconel 625. It is

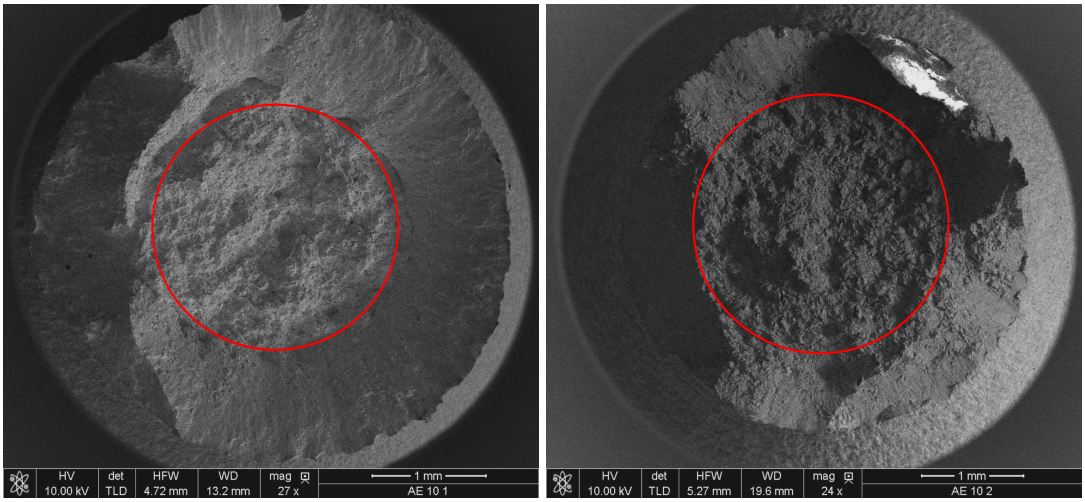

(a) CAE10 - 1 (0.8 mm/min) (b) CAE10 - 2 (0.08 mm/min)

Figure 1.13: Fracture surface at macro scale of specimens CAE10-1 and CAE10-2. The cup-cone aspect of the surface is typical of ductile failure. The circular shape of the flat zone indicates an isotropic behaviour.

now interesting to observe the fracture surface at the scale of the grain size, considering that specimens CAE10-1 and CAE10-2 were tested at different (one order of magnitude) displacement rates. The specimen loaded at a higher displacement rate (CAE10-1, figure 1.14(a), loaded at 0.8 mm/min which induces a local strain rate of about $10^{-3}s^{-1}$) shows transgranular fracture typical of ductile failure. Indeed, the fracture surface is characterized by the presence of large cavities (of about 10 μm) initiated at inclusions. The specimens loaded at a lower displacement rate (CAE10-2, figure 1.14(b) loaded at 0.08 mm/min which induces a local strain rate of about $10^{-4}s^{-1}$) show both intergranular and transgranular fracture. Indeed, in addition to the large cavities, the fracture surface is characterized by macro faults which size(about 20 μm) is consistent with the average grain size. There might be possible relation between the strain rate and the failure mechanisms, as discussed in the PhD thesis of Max [95] where it is observed a change between intergranular and transgranular fracture as function of temperature and strain rate. This observation seems consistent with the fracture surfaces of axisymmetric specimens CAE4-1 and CSMOOTH-2 (see figure 1.15) and the fracture surfaces of the flat specimens PAE1-1 and PAE2-1 (see figure 1.16). The local strain rate of these latter 4 specimens was of the order of $10^{-4}s^{-1}$. However, the relation between strain rate, stress triaxiality and fracture mechanism was not further investigated in the present work.

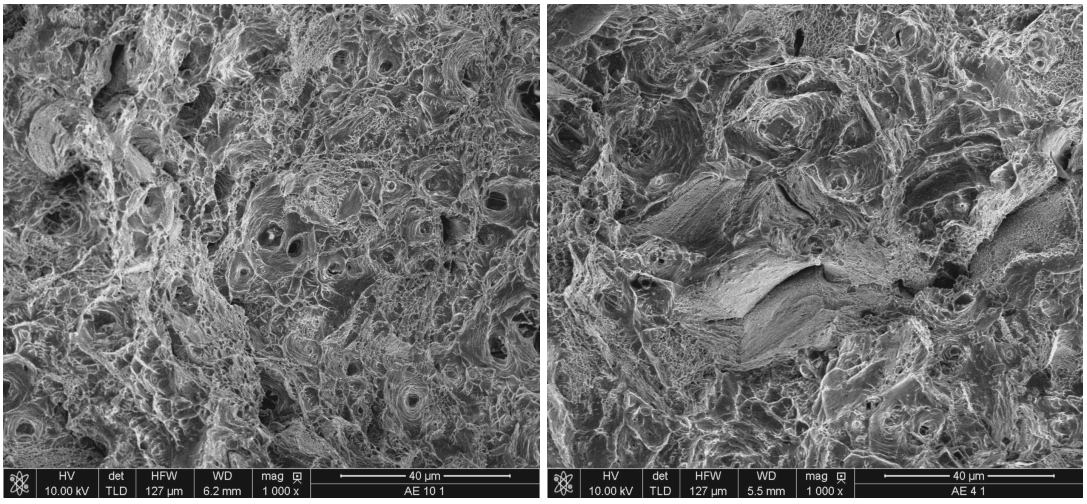

(a) CAE10 - 1 (0.8 mm/min) (b) CAE10 - 2 (0.08 mm/min)

Figure 1.14: Fracture surfaces observations of the notched specimen CAE10. The different loading rates generate different fracture surfaces. The specimen loaded at a higher rate (left) shows transgranular fracture, while the specimen loaded at a lower rate (right) shows, in addition, intergranular fracture. Images were taken near the centre of the fracture surface.

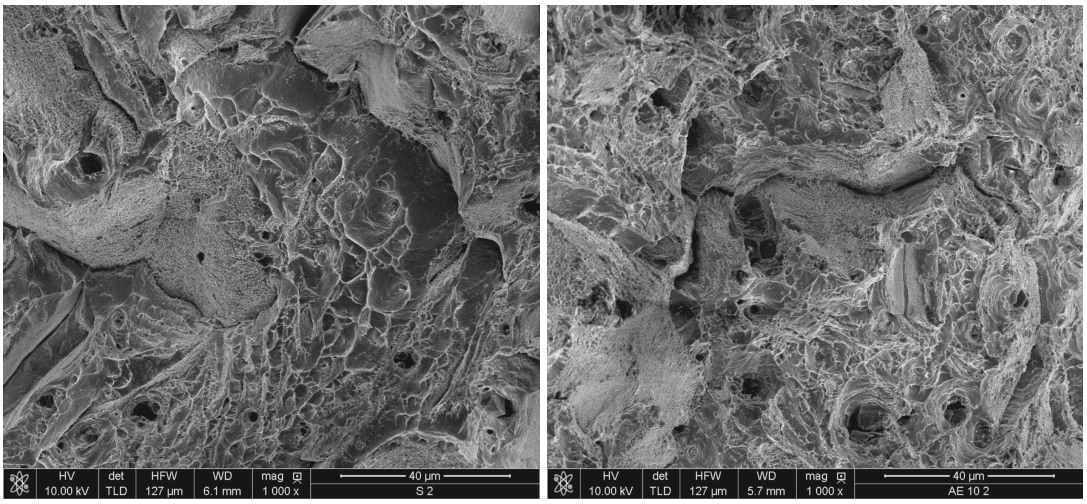

(a) CSMOOTH - 2 (b) CAE4 - 1

Figure 1.15: Fracture surfaces observations of the notched specimens CAE4-1 and CSMOOTH-2. The fracture surfaces are characterized both by intergranular fracture and transgranular fracture. Images were taken near the centre of the fracture surface.

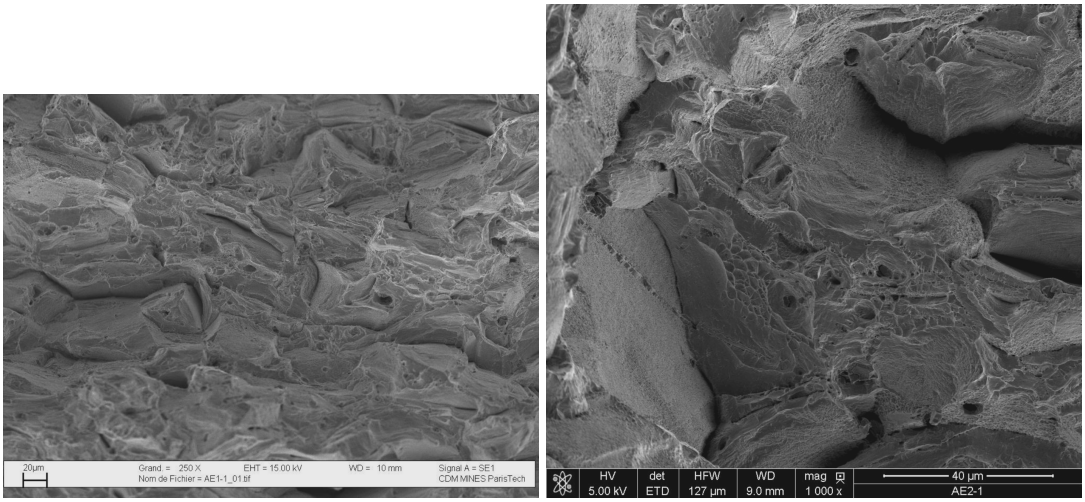

(a) PAE1 - 1 (b) PAE2 - 1

Figure 1.16: Fracture surfaces observations of the notched specimens PAE1-1 and PAE2-1. The fracture surfaces are characterized prevalently by intergranular fracture. Images were taken near the centre of the fracture surface.

Measurement of the initial void volume fraction The analysis of the polished cross section[4] of the raw material allows to calculate the initial void volume fraction of the material. Furthermore, the same analysis performed on the cross sections of the broken specimens allows to trace the evolution of void volume fraction versus strain. From this latter, it is possible to extrapolate the value of void volume fraction at arbitrary values of strain. Three tests have been considered to perform this analysis (CAE10-3, PAE2-2, PSMOOTH-1).

The void volume fraction is quantified in terms of percentage of surface by an image thresholding operation. To distinguish voids from inclusions (all types confounded) the SEM was set to generate images where matrix, voids and inclusions correspond to three distinct gray levels as in figure 1.17. A regular grid of images(200 μm wide, 10% overlap) has been created for each

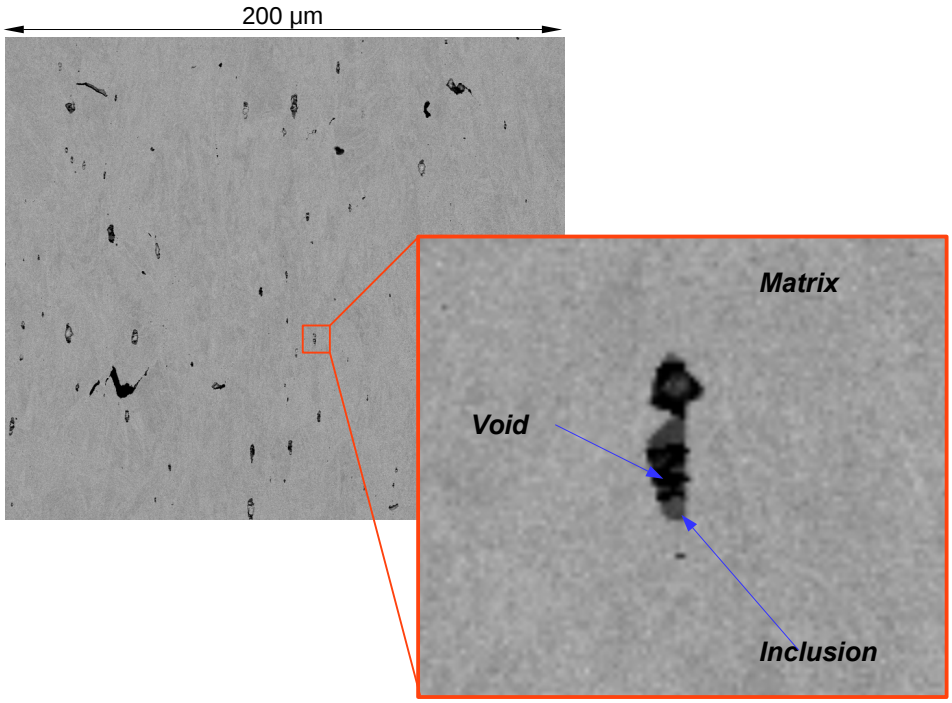

Figure 1.17: Example of polished cross section (CAE10-3). Matrix, voids and inclusions correspond to three distinct gray levels. Although the void volume fraction might seem high, the majority of the dark spot are inclusions. The image has also been chosen as illustration to be particularly rich in dark spots, compared to the remaining images.

cross section, as in figure 1.18. Once the void volume fraction value f, and the inclusion ratio value r, were computed for each subset, the following relation has been used to fit the evolution of porosity versus the distance from fracture, denoted x (which is related to the strain level):

$$f = ae^{-bx} + f_0 \tag{1.7}$$

[4]The cross section is realized by performing a cut along the loading direction (*i.e.* perpendicular to the fracture surface

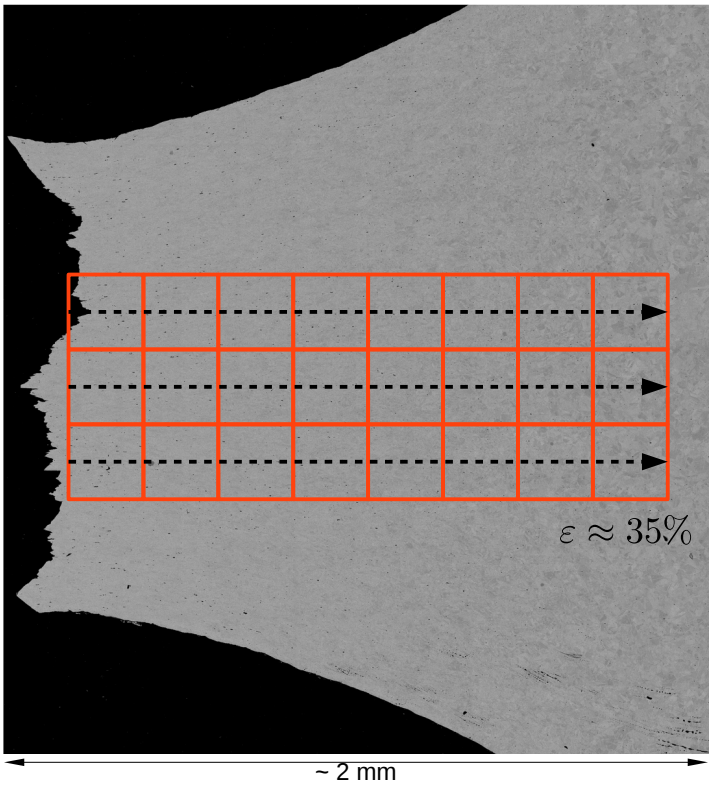

Figure 1.18: Schema of regular grid on cross section (CAE10-3).

where x is the distance from the fracture surface. Coefficients a and b are two adjustable coefficients used to perform an exponential fit. Finally, coefficient f_0 quantifies the void volume fraction at the opposite of the fracture surface. The choice of the constant parameter f_0 allows to use equation 1.7 to fit constant profiles of void volume fraction (*e.g.* for the raw material). Therefore, parameter f_0 will be used to evaluate the void growth versus strain. Figure 1.19 shows the profiles of porosity and inclusions (which have been fit considering a constant value), while table 1.5 reports the coefficient f_0 for the considered specimens and the relative strain level measured by DIC. Let us note that void growth is relatively low, since at a relative high strain level (35% for a deformation at break of 50%) void volume fraction is barely 5 times higher than the initial value, which is considerably low as well ($1 \cdot 10^{-4}$). This observation is consistent with the observation at macroscopic scale of table 1.4: void volume fraction is not high enough to induce an observable loss of stiffness of the material. Finally, let us note that the inclusion level is approximatively constant for the considered specimens.

Specimen	p_0	$\varepsilon\%$
Raw Material	$1 \cdot 10^{-4}$	0
PAE2-2	$1.8 \cdot 10^{-4}$	10
PSMOOTH-1	$3.7 \cdot 10^{-4}$	27
CAE10-3	$5.6 \cdot 10^{-4}$	35

Table 1.5: void volume fraction for different specimens and the relative (approximative) strain level. The void volume fraction at relatively high strain level is moderate.

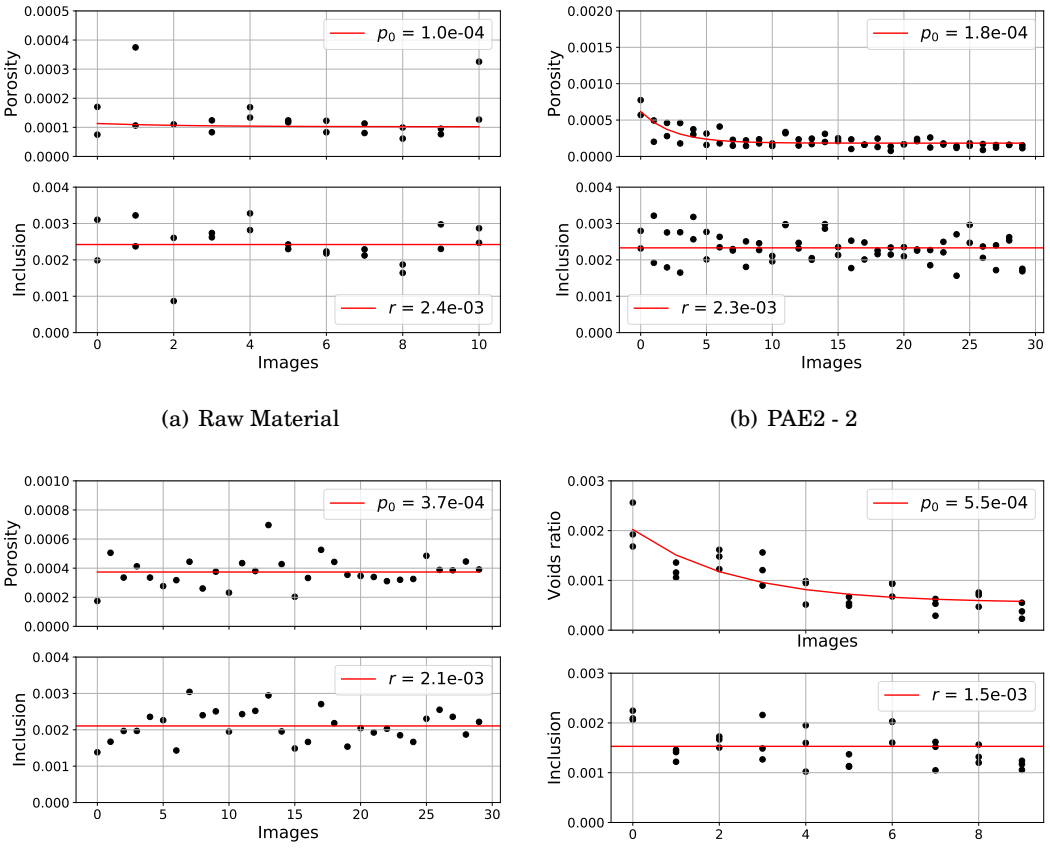

(a) Raw Material

(b) PAE2 - 2

(c) PSMOOTH 1

(d) CAE10 - 3

Figure 1.19: Porosity and inclusions profiles along the loading direction.

Résumé

Ce premier chapitre présente l'approche expérimentale. Y sont décrits le choix des géométries, ainsi que la méthode de mesure par corrélation d'images et les premières observations sur les essais. Bien que la stratégie d'identification proposée dans cette thèse soit conçue pour tous les matériaux ductiles soumis à de grandes déformations, un seul matériau est utilisé pour mener l'étude. Il s'agit de l'alliage Inconel625, utilisé dans l'aéronautique.
La rupture ductile est fortement influencée par le niveau de triaxialité des contraintes. Afin de varier l'état de contraintes, les essais sont réalisés sur des éprouvettes entaillées avec différents rayons d'entaille. Outre les géométries axisymétriques habituellement utilisées pour l'étude de la rupture ductile, des géométries planes sont également prises en compte afin de tirer profit de la richesse des informations de la corrélation d'images. En effet, grâce à la faible épaisseur des éprouvettes planes, le niveau de triaxialité est quasi-constant dans l'épaisseur et l'amorçage de la fissure est visible en surface.
La corrélation d'images est faite grâce à un algorithme de corrélation local développé à l'ONERA. Les résultats fournis sont denses et non filtrés (lissage, etc.).
L'alliage étudié montre une rupture à un niveau important de déformation (≈ 50 % à l'ambiante) et une forte dispersion de la réponse macroscopique. Cette dispersion affecte davantage le domaine plastique pour les éprouvettes axisymétriques et l'instant d'amorçage de la fissure pour les éprouvettes planes. Dans tous les cas, la rupture suit rapidement l'amorçage et s'accompagne peu de striction.
Les observations au microscope à balayage (MEB) des sections polies permettent de calculer une valeur pour le taux de porosité initial, et montrent aussi que ce taux reste faible jusqu'à des niveaux de déformations proches de la rupture. Cette observation est confirmée par une diminution négligeable du module de Young.

CHAPTER 2

NUMERICAL MODELLING OF DUCTILE FAILURE WITHIN THE FINITE STRAIN FRAMEWORK

This chapter describes the considered numerical modelling for ductile failure within the finite strain framework. On the one hand, it is necessary to dispose of a numerical model as complete and representative of the reality as possible. On the other hand, it is necessary to dispose of a model as simple as possible, in order to consider a relatively low number of parameters. In fact, the difficulties of parameter identification increase together with the number of parameters, since it becomes not trivial to assess whether the parameters are independent between each other. The choice of the numerical model starts from the analysis of the mechanical tests (see chapter 1). The considered material, Inconel 625, shows a prominent strain hardening followed by a softening response attributed to damage evolution, exceeding a strain level of about 50% at break. Section 2.1 describes the material's model up to softening, which involves elastic and plastic deformations. Section 2.2 is dedicated to the modelling of the damage process using the GTN model. Finally, section 2.3 describes the finite element approach, which considers a large strain formulation and a non-local regularization proposed in a previous PhD thesis carried out at EdF R&D [136, 137].

2.1 Elasto-Visco-Plastic behaviour

From the experimental stress-strain curve of figure 1.9, issued from the test on a smooth cylindrical specimen, it is clear that the considered material presents a non-linear behaviour. It might be subdivided into three parts, each one associated to a different mathematical (thus numerical) description. First of all, a linear segment, which is ruled by the elasticity theory. Secondly, a non linear ascending segment, which is ruled by the plasticity theory. Finally, a non linear descending segment, which is, here, triggered by geometrical instabilities (necking) and ruled by damage development. Moreover, due to the metallic nature of the material, some viscous effects are considered into the numerical model, although the tests carried out do not allow the identification of the viscous parameters. Finally, let us underline that what is presented below is restricted to isotropic behaviours. Indeed, this property of the considered material, that has been

confirmed by the observation of the fracture surfaces (see figure 1.13), leads to several modelling simplifications.

2.1.1 Elastic deformation

Elastic deformation is reversible and so, non-dissipative. Once the load is removed, the structure retrieves its original shape. Metallic materials have, in general, an elastic behaviour, according to which the elastic deformation $\underset{\sim}{\varepsilon}_{el}$ is proportional (linear) to the stress $\underset{\sim}{\sigma}$. The mathematical relation which describes a linear elastic behaviour is given by Hooke's law [128], and derives from the existence of an elastic energy density Φ_{el}:

$$\underset{\sim}{\sigma} = \frac{\partial \Phi_{el}}{\partial \underset{\sim}{\varepsilon}_{el}} \tag{2.1}$$

Hooke's law reads:

$$\underset{\sim}{\varepsilon}_{el} = \underset{\approx}{\mathbb{A}} : \underset{\sim}{\sigma} \tag{2.2}$$

where $\underset{\approx}{\mathbb{A}}$ is referred to as the compliance tensor. It is strictly positive and its inverse is referred to as the stiffness tensor. These tensors contains 21 independent elastic coefficients, which reduce to 2 for an isotropic behaviour. Hence, the stress-strain relation is, in this case, a function of the Young's modulus E and the Poisson's ratio ν:

$$\underset{\sim}{\varepsilon}_{el} = \frac{1+\nu}{E}\underset{\sim}{\sigma} - \frac{\nu}{E}\mathrm{Tr}(\underset{\sim}{\sigma})\,\underset{\sim}{I} \tag{2.3}$$

The elastic parameters, Young's modulus and Poisson's ratio, are not considered into the FEMU process: elastic modulus is measured following a classic procedure as described in chapter 1, while Poisson's ratio is a value taken from the literature [1]. In fact, since the objective of the current work is the identification of damage parameters, the data sampling of the mechanical tests was not suited for the identification of the elastic coefficients[1].

Moreover, let us recall that the scope of this study is not to provide an alternative identification tool for parameters that can actually be identified elsewhere with higher precision. The goal is to propose tools to identify those parameters for which there is not a commonly agreed procedure.

2.1.2 Plastic deformation

At crystalline level, the plastic deformation is related to the energy required to move the dislocations within the lattice. There is not a unique theory to approach plasticity, since the mechanisms that rule such phenomena are complex [89]. The main difficulties come from the irreversibility of the plastic deformation and the non-holonomic character of the deformation[2]. However, in continuum mechanics, in general, an empirical relation between stress and strain is considered to describe the plastic behaviour at the scale of the Representative Elementary Volume (REV). To do so, two main theories have been proposed so far.

[1]The images recording was performed at a constant frequency, which value was adapted to record a reasonable number of images (< 1000) for the complete test. Therefore, no more than 10 points within the elastic range, which does not assure an efficient identification of the elastic parameters

[2]Non-holomic character: the plastic deformation does not depends only on the applied load but also on the history of load.

One theory is the so called *deformation theory*, which attempts to model plasticity by means of a continuous relation between stress and strain $\underset{\sim}{\sigma} = f(\underset{\sim}{\varepsilon})$, as is done for the elastic deformation. However, such an approach does not allow to take into account the irreversibility of plastic deformation.

A second theory is the *incremental theory of plasticity*, also referred to as *flow theory*, which is based on a mathematical relation between the increment of load and the consequent increment of the solution in terms of stress, strain and displacement $(\delta\underset{\sim}{\sigma}, \delta\underset{\sim}{\varepsilon}, \delta\underset{\sim}{u})$. The increment of deformation is then considered as the composition of an elastic contribution and a plastic contribution $\delta\varepsilon = \delta\underset{\sim}{\varepsilon}_{el} + \delta\underset{\sim}{\varepsilon}_{pl}$. According to this theory, if the material is not undergoing plastic deformation, its behaviour is purely elastic. Furthermore, the elastic component of deformation is always recoverable and it is the unique component of deformation that is related to the increment of stress. This approach is quite efficient since it allows to take into account both irreversibility and the non-holonomic character of plastic deformation.

Yield criterion The transition from elastic behaviour to plastic behaviour is called *yield*. A so called *yield criterion* is used to establish whether a material is yielding. Such a criterion is usually formulated in terms of equivalent tensile stress, σ_{eq}, which is a scalar value that can be calculated from the stress stress tensor, either in terms of its invariants (I_1, I_2, I_3) or in terms of the principal stresses $(\sigma_1, \sigma_2, \sigma_3)$. The yielding begins when the equivalent stress σ_{eq} reaches a critical value known as *yield stress*, that is the uniaxial elastic limit of the material. In this way, the yielding of materials under complex loadings can be estimated from the results of uniaxial tensile tests.

The yield criteria for ductile metals are generally independent of the first stress invariant (the hydrostatic pressure) because of the incompressibility of the plastic flow [10]. The two most widespread criteria for ductile isotropic metals are the von Mises criterion [99], and the Tresca criterion. According to the von Mises criterion, the material yields when the distortion strain energy density reaches a threshold value, while according to Tresca the material yields when the maximum shear stress reaches a threshold value. The respective expressions of the equivalent tensile stress read:

$$\sigma_{eq} = \frac{1}{2}\left[(\sigma_1 - \sigma_2)^2 + (\sigma_2 - \sigma_3)^2 + (\sigma_3 - \sigma_1)^2\right]^{\frac{1}{2}} \tag{2.4}$$

for the von Mises criterion and:

$$\sigma_{eq} = \frac{1}{2}\max(|\sigma_1 - \sigma_2|, |\sigma_2 - \sigma_3|, |\sigma_3 - \sigma_1|) \tag{2.5}$$

for the Tresca criterion.

Let us note that a generic yield criterion defines a surface in the space of stresses that is referred to as the *yield surface* (see figure 2.1).

Experimental data for isotropic metals tend to lie in between the Tresca surface and the von Mises surface [64]. Therefore, several alternative criteria have been proposed in the literature [10] so far, most of them including the contribution of the third invariant of the stress tensor and a variable number of additional parameters. In the present work we consider the Hosford yield criterion [64], which is based on a unique additional parameter $n \in [1, +\infty[\in \mathbb{R}^2$, here referred to as the Hosford exponent. The equivalent stress for this criterion reads:

$$\sigma_{eq} = \left[\frac{(\sigma_1 - \sigma_2)^n + (\sigma_2 - \sigma_3)^n + (\sigma_1 - \sigma_3)^n}{2}\right]^{\frac{1}{n}} \tag{2.6}$$

When varying the Hosford exponent from one to infinity, the Hosford surface expands starting from the Tresca surface for $n = 1$, through the von Mises surface for $n = 2$, to reach the maximum expansion for $n = 2.767$ [64]. After that value, the Hosford surface shrinks, crossing again the von Mises surface ($n = 4$) to reach the Tresca surface ($n = +\infty$). The Hosford criterion was chosen since it allows to reproduce any experimental surface that lies in between the Tresca surface and the von Mises surface, as shown in figure 2.1.

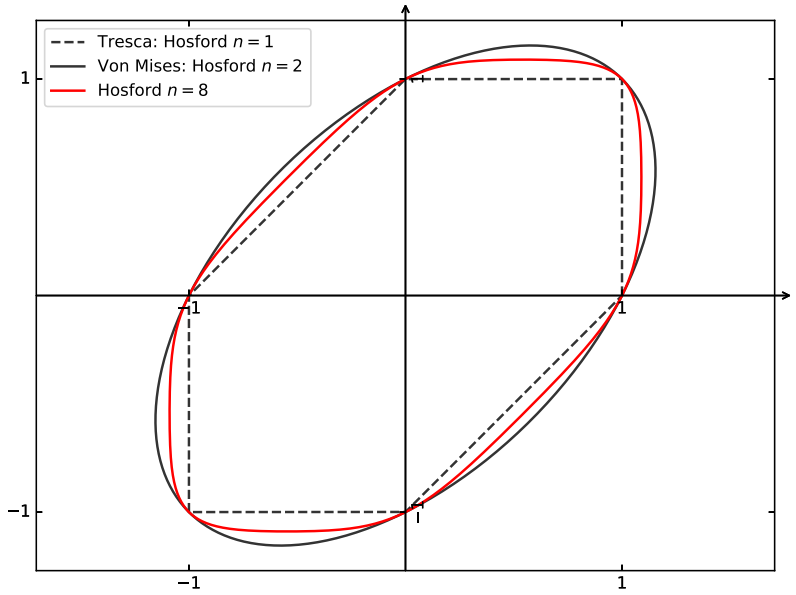

Figure 2.1: Projection on the $\sigma_3 = 0$ plane of three Hosford yield surfaces with different exponents. The Hosford yield surface can reduce both to the Tresca surface and the Von Mises surface.

Hardening In the general case, the yield surface changes with plastic deformation. The description of the variation is referred to as *hardening rule*, which is a function of the so called hardening parameters. Two common hardening rules are kinematic hardening and isotropic hardening. Kinematic hardening is when the yield surface remains the shame shape and size but translates in the stress space (Bauschinger effect). Isotropic hardening is when the yield surface remains the same shape but expands with increasing stress.

The identification of the kinematic hardening parameters requires tensile tests involving cyclic loadings, while the identification of the isotropic hardening requires only monotonous loadings. Therefore, the tensile tests carried out in the present study only allow the characterization of isotropic hardening. This is the unique hardening rule considered in the following. From here, the material can either exhibits:

- perfect plastic behaviour: further deformation of the material occurs at constant stress. The yield surface does not expand nor shrink;

- hardening behaviour : further deformation of the material induces an increase of the yield stress. The yield surface expands;

- softening behaviour (negative hardening): further deformation of the material induces a reduction of the yield stress. The yield surface shrinks.

From figure 1.9, it is clear that the considered Inconel 625 has an hardening behaviour, since the flow stress arises with the deformation. The hardening law considered in this study is taken from reference [126], which is in turn inspired from the exponential law proposed by Voce [132]. Such an hardening law describes hardening as a function of the cumulated plastic strain p, an internal state variable that depends on the loading history of the material:

$$R(p) = R_0 + Q_1 \cdot (1 - e^{-b_1 p}) + Q_2 \cdot (1 - e^{-b_2 p}) \tag{2.7}$$

where $R0$ is the initial yield stress and Q_1,b_1,Q_2,b_2 are the hardening parameters. The choice of this hardening law is motivated by the large deformations of the Inconel 625. Indeed, the two non-linear terms allow to fit for example an early stage and a late stage of work hardening. Both the yield stress and the hardening parameters will be identified using FEMU.

Flow rule To complete the analysis of the plastic deformation it is necessary to introduce the so called *flow rule*, which states a relation between the plastic deformation $\underset{\sim}{\varepsilon}_{pl}$ and the cumulated plastic strain p.

Most of the metallic materials satisfy the Drucker's first stability criterion [38] (also called the Hill's stability criterion since it was originally proposed by Hill [63]), and they are referred to as the *standard materials*. According to this criterion, the plastic work of the material can only increase:

$$\mathrm{d}\underset{\sim}{\sigma} : \mathrm{d}\underset{\sim}{\varepsilon}_{pl} \geq 0 \tag{2.8}$$

Several important consequences follows from this criterion and characterize the standard materials:

- the internal free energy density, denoted here $\Phi(\underset{\sim}{\varepsilon}_{el}, \underline{a})$, is a convex function of the elastic deformation and the internal variables

- the internal energy density can be split into an elastic component and a plastic component: $\Phi(\underset{\sim}{\varepsilon}_{el}, \underline{a}) = \Phi_{el}(\underset{\sim}{\varepsilon}_{el}) + \Phi_{pl}(\underline{a})$

- the yield surface, denoted here $\Psi(\underset{\sim}{\sigma}, p)$, is convex

- the plastic flow is normal to the yield surface.

Consequently, the flow rule can be written as:

$$\dot{\underset{\sim}{\varepsilon}}_{pl} = \dot{p} \frac{\partial \Psi}{\partial \sigma} \tag{2.9}$$

where $\dot{p}$ is referred to as plastic multiplier and it is non null solely if plastic deformation occurs.

2.1.3 Viscous deformation

Although the characterization of viscous effects would have required tests at higher loading rates (compared to the the tests described in chapter 1), viscous effects are generally taken into account into the numerical modelling of a metallic material. Moreover, from a numerical point of view, viscous effects foster convergence during damage evolution and crack propagation. Therefore, a simple Norton flow rule is considered. It reads:

$$\dot{p} = \dot{p}_0 \left(\frac{\Psi}{\sigma_0} \right)^m \tag{2.10}$$

where σ_0 and m are scalar parameters. Nevertheless, since those parameters cannot be identified in the present study, their values were arbitrarily fixed to minimize their influence on the material's response. A simple criterion was used to set $\sigma_0 = 10$ MPa and $m = 5$: these values induce, for the considered loading rates, a stress variation (compared to the rate-independent behaviour) considerably lower than the uncertainty of the load cell of the testing machine.

2.2 Damage behaviour

In this section, the numerical tools used for the simulation of the failure process are described after a brief introduction of the possible approaches to fracture.

2.2.1 Global and local approaches to fracture

Two main approaches have been developed so far to simulate fracture [14]. The first approach is referred to as *global* while the second approach is referred to as *local*. The global approach to fracture is essentially based on the Linear and Non-Linear Fracture Mechanics. The assumption is that fracture resistance can be assessed in terms of a single macroscopic parameter, as the J-integral [65, 112] or the crack tip opening displacement. The global approach to fracture is simple and widely used. The main limitations of this approach arise when the process zone, *i.e.* where fracture occurs, has a dimension which is not negligible compared to the size of the structure.

The local approach to fracture is based on local criteria. It is based on a more physical representation of the material degradation. The local approaches can, in turn, be divided into *phenomenological models* and *micro-mechanical models*.

According to phenomenological models, the material degradation is considered from a macroscopic point of view. To do so, solely the effects of damage are considered at the scale of the Representative Elementary Volume. The physics of the phenomenon at the microscale is not taken into account. Within this category, it is worth mentioning:

- the approach of Kachanov and Rabotnov [66, 111], where damage is quantified as the reduction of the load carrying effective area;
- the approach of Lemaitre and Chaboche [81], where damage is quantified as the variation of the elastic modulus;
- the approach chosen by Engelen et al. [40], where damage is quantified by means of a scalar variable solely driven by the cumulated plastic strain.

According to micro-mechanical models, the material degradation is considered from a microscopic point of view. The evolution of damage (nucleation, growth and coalescence of micro-voids) is directly modelled. It is the case of the Gurson's model [57] and the Rousselier's model [117], to mention two of the most known models. Even though a pure micro-mechanical description could be more accurate, the complex phenomena involved in ductile failure would lead to an extremely complex micro-mechanical representation. Thus, some phenomenological approximations are in general accepted and introduced within micro-mechanical models. As an example, the GTN [130, 131] (Gurson Tvergaard Needleman) model, which is used in the present study, consists in a modified version of the micro-mechanical model of Gurson, where void nucleation and void coalescence is modelled considering a phenomenological description.

Additional details about the continuum approaches to damage can be found into the book of Murakami [102] and into the review of Besson [14].

2.2.2 Damage evolution by void growth

To start, let us recall that the ductile failure of metals is a damage process that involves growth, nucleation and coalescence of micro voids that are responsible for the loss of bearing capacity of the structure. In what follows, damage is modelled using a scalar variable f representing the void volume fraction. On the one hand, the choice of a scalar variable limits the description of damage to an uniform distribution of spherical voids. On the other hand it leads to a simple but efficient description of the phenomenon.

One of the first works on void growth is attributed to Rice and Tracey [114]. They studied the growth of a sperichal cavity within a infinite perfectly plastic medium. The authors highlighted the relation between the stress triaxiality level[3] and the growth of the cavities. This is the main result of their work, since the Rice and Tracey model cannot be applied to a general porous material because of the hypothesis of infinite medium.

Later, Gurson [57] defined a damaging yield criterion and an expression for the evolution of the void volume fraction. It is a complete model to study the evolution of spherical voids within a perfectly plastic medium. According to the Gurson approach, void growth reduces the bearing capacity of the material and modifies the yield surface, shrinking it. Let us note that such a softening behaviour violates the conditions of standard material according to Drucker. From a numerical point of view, it leads to the localization problem, which will be discussed in section 2.3.1.

The yield surface of the Gurson model reads:

$$\Psi(\sigma, R, f) = \left(\frac{\sigma_{eq}}{R}\right)^2 + 2f\cosh\left(\frac{3\sigma_h}{2R}\right) - 1 - f^2 \leq 0 \tag{2.11}$$

which reduces to a Von Mises surface when no damage occurs ($f = 0$). The expression of the void growth ratio arises from the incompressibility of the plastic flow (elastic deformation is neglected):

$$\dot{f} = \dot{f}_g = (1-f)Tr(\dot{\varepsilon}_{pl}) \tag{2.12}$$

Nevertheless, the Gurson's analysis does not take into account nucleation and void coalescence. Tveergaard and Needleman [131] improved the model including the missing phenomena of ductile failure, creating the so called GTN model.

[3] The stress triaxiality is defined as $T = \frac{\sigma_h}{\sigma_{eq}}$ where σ_{eq} the equivalent stress and $\sigma_h = \frac{\sigma_1+\sigma_2+\sigma_3}{3}$ is the hydrostatic pressure

Coalescence Coalescence is introduced by means of two parameters q_1 and q_2 and critical level of void volume fraction f_c at which coalescence begins. Hence, the GTN yield surface becomes:

$$\Psi(\sigma,R,f) = \left(\frac{\sigma_{eq}}{R}\right)^2 + 2q_1 f^* \cosh\left(\frac{3q_2\sigma_h}{2R}\right) - 1 - (q_1 f^*)^2 \leq 0 \tag{2.13}$$

where f^* is an effective void volume fraction, defined as:

$$f^* = \begin{cases} f & \text{if } f \leq f_c \\ f_c + \delta(f - f_c) & \text{otherwise} \end{cases} \tag{2.14}$$

The scalar coefficient δ represents the acceleration of the void growth due to coalescence. According to the GTN model, failure happens when the effective void volume fraction f reaches a maximum value f_r. Rupture occurs when $f^* = \frac{1}{q_1}$:

$$f_r = \left(\frac{1}{q_1} - f_c\right)\frac{1}{\delta} + f_c \tag{2.15}$$

Nucleation Void nucleation is modelled as a phenomenological contribution $\dot{f_n}$ to the void growth rate $\dot{f}$. It is expressed as a function of the cumulated plastic strain:

$$\dot{f} = \dot{f_g} + \dot{f_n} = (1-f)Tr(\underline{\dot{\varepsilon}}_{pl}) + A_n(p)\dot{p} \tag{2.16}$$

where $A_n(p) > 0$ is the phenomenological description of the nucleation. A common expression for $A_n(p)$ is given by Tvergaard and Needleman [131]:

$$A_n(p) = \frac{f_N}{s_N\sqrt{2\pi}} \exp\left[-\frac{1}{2}\left(\frac{p - p_N}{s_N}\right)^2\right] \tag{2.17}$$

where f_N is the inclusion ratio, which is considered since new voids nucleate at inclusions. Value p_N is the effective plastic strain at which the nucleation ratio is maximum, and s_N is the standard deviation of the deformation due to nucleation. A simpler description of nucleation could be a linear evolution of nucleation triggered at a certain critical value p_s of cumulated plastic strain:

$$A_n(p) = k\mathcal{H}(p - p_s) \tag{2.18}$$

where k is a constant value and $\mathcal{H}$ is the heaviside function. This latter nucleation law is considered in the present work, since as observed in section 1.4, the considered Inconel 625 shows a strong (supposedly linear) nucleation of new voids occurring at a high plastic strain levels.

Finally, let us note that although the GTN model provides a rich description of damage, it has some limitations. In fact, the GTN model does not predict correctly failure under pure shear loading since pure shear is associated to a null stress triaxiality level. Furthermore,the GTN model does not predict correctly failure when voids are not spherical [50].

2.3 Finite Element approach

The high deformation values reached during the mechanical tests (see chapter 1) requires a finite element approach specific for large deformations. Moreover, the chosen material behaviour leads to well known numerical problems such as volumetric locking and strain localization, which require advanced techniques to be solved.

2.3.0.1 Elastic-Plastic constitutive laws within the finite strain framework

The incremental theory of plasticity is still a valid approach within the finite strain framework. However, there is a large debate about the correct decomposition of deformation into an elastic component and a plastic component. In the following, the most considered types of decomposition are presented.

Additive decomposition The first approaches that have been proposed were direct extensions of the additive decomposition equations defined within the small strain framework $\dot{\underset{\sim}{\varepsilon}} = \dot{\underset{\sim}{\varepsilon}}_{el} + \dot{\underset{\sim}{\varepsilon}}_{pl}$, but using the strain rate tensor $\underset{\sim}{D}$. Let us note that since the material derivative of the strain tensor is non-objective, the relation must be written in terms of objective derivatives[4].

$$\underset{\sim}{D} = \underset{\sim}{D}_{el} + \underset{\sim}{D}_{pl} \tag{2.19}$$

Nevertheless, despite their wide use [15] such approaches are not considered here since they show undesirable side-effects as a certain energy dissipation within the elastic range (which is non-physical) and shear oscillations (*i.e.* distortion of the solution) [36, 120].

Starting from Lee [80], several authors considered a multiplicative decomposition of the deformation gradient into an elastic and plastic contribution:

$$\underset{\sim}{F} = \underset{\sim}{F}_{el} \cdot \underset{\sim}{F}_{pl} \tag{2.20}$$

Such a decomposition implies the introduction of an in-between configuration obtained by a conceptual de-stressing (to a null stress) of the currently deformed material configuration. However, such an intermediate state is fictitious and non unique. This is the main drawback of this approach. The considered deformation tensors are:

$$\underset{\sim}{G}_{pl} = (\underset{\sim}{F}_{pl}^T \underset{\sim}{F}_{pl})^{-1} \quad , \quad \underset{\sim}{B}_{el} = \underset{\sim}{F}\underset{\sim}{G}_{pl}\underset{\sim}{F}^T \tag{2.21}$$

where $\underset{\sim}{G}_{pl}$ is a Lagrangian tensor and $\underset{\sim}{B}_{el}$ an Eulerian tensor. A tensor is said to be Lagrangian when it maps the deformation on the reference configuration. On the opposite, a tensor is said to be Eulerian when it maps the deformation on the deformed configuration [74]. The internal energy decomposition reads:

$$\Phi = \Phi_{el}(\underset{\sim}{B}_{el}) + \Phi_{pl}(p) \tag{2.22}$$

where p is the cumulated plastic strain, the unique internal variable considered. It follows the constitutive law:

$$\underset{\sim}{\tau} = 2\frac{\partial \Phi_{el}}{\partial \underset{\sim}{B}_{el}} \cdot \underset{\sim}{B}_{el} \quad , \quad A = -\frac{\partial \Phi_{pl}}{\partial p} \tag{2.23}$$

where τ is the Kirchhoff stress tensor and A the thermodynamic force associated to p. The plastic flow is characterized by the following set of equations:

$$\dot{\underset{\sim}{G}}_{pl} = -2\lambda \underset{\sim}{F}^{-1} \frac{\partial \Psi}{\partial \underset{\sim}{\tau}} \underset{\sim}{B}_{el} (\underset{\sim}{F}^T)^{-1} \qquad \dot{p} = \lambda \frac{\partial \Psi}{\partial A} \qquad \lambda \Psi = 0 \qquad \Psi \leq 0 \qquad \lambda \geq 0 \tag{2.24}$$

[4] According to the principle of material objectivity, a kinematic tensor is said to be objective if it is independent from the frame of reference used to describe the phenomenon [69]. As an example, the Cauchy-Green deformation tensor $\underset{\sim}{C} = \underset{\sim}{F}^T \underset{\sim}{F}$ is an objective tensor. Instead, the material derivative of a deformation tensor is not objective. In this case, it is possible to formulate the problem in terms of objective derivatives. The most commonly used objective derivatives are the Truesdell rate, the Green-Nagdhi rate and the Jaumann rate.

where Ψ is the yield potential function and λ the plastic multiplier.

More recently, Papadopoulos et al. [106] first, and Miehe et al. [98] later, considered an additive decomposition of the deformation gradient within the logarithmic strains space:

$$\underset{\sim}{E} = \underset{\sim}{E}_{el} + \underset{\sim}{E}_{pl} \tag{2.25}$$

where

$$\underset{\sim}{E} = \frac{1}{2}\log(\underset{\sim}{F}^T \cdot \underset{\sim}{F}) \tag{2.26}$$

Let us introduce the stress tensor $\underset{\sim}{T}$, symmetric, defined by duality with respect to the logarithmic strain rate. Then, the stress power $\mathscr{P}$ reads:

$$\mathscr{P} = \int_{\Omega_0} \underset{\sim}{T} : \dot{\underset{\sim}{E}} \, \mathrm{d}\Omega_0 \tag{2.27}$$

Tensor $\underset{\sim}{T}$ is a measure of stress within the logarithmic space of strain. It does not have a physical meaning, but classical stress description as the Kirchoff stress tensor or the Cauchy stress tensor can be recovered from $\underset{\sim}{T}$ as described in reference [98]. According to the flow theory, the internal energy density reads:

$$\Phi = \Phi_{el}(\underset{\sim}{E}_{el}) + \Phi_{pl}(p) \tag{2.28}$$

It follows the constitutive law:

$$\underset{\sim}{T} = \partial\Phi_{el} \quad , \quad A = \frac{\partial\Phi_{pl}}{\partial p} \tag{2.29}$$

where the stress-strain relation is hyperelastic. The condition of material objectivity is respected [136, 137]. Furthermore, the plastic flow is characterized as follow:

$$\dot{\underset{\sim}{E}}_{pl} = \lambda\frac{\partial\Psi}{\partial\underset{\sim}{T}} \qquad \dot{p} = -\lambda\frac{\partial\Psi}{\partial A} \qquad \lambda\Psi = 0 \qquad \Psi \leq 0 \qquad \lambda \geq 0 \tag{2.30}$$

Shuthov [120] compared the approaches mentioned above based on a weak-invariance indicator: the most rigorous approach appears to be the multiplicative decomposition, since the additive decomposition within the logarithmic strain approach is accurate solely if the elastic deformation is negligible compared to plastic deformation, which is the case of this study. Indeed, according to the experimental tests illustrated in chapter 1, the elastic deformation can be considered as negligible compared with the plastic deformation.

Furthermore, the similarity of the additive decomposition within the logarithmic strain space with the small strain formulation makes its implementation relatively easier compared to the multiplicative approach. This is why this latter approach was retained in this study. The implementation of the selected approach is entirely inherited from the previous PhD thesis of Zhang [136, 137], which proposes a robust and complete framework for the simulation of ductile failure within the large strain framework (the details about the reformulation of the GTN model within the logarithmic strain space can be found within the the original work).

2.3.1 The strain localization problem

Phenomenon The softening behaviour of a structure is triggered by instabilities which nature might be either geometrical (necking) or material (local inhomogeneities) [113]. During the softening phase, the deformation is concentrated within a thin zone, referred to as localization band, while the rest of the structure undergoes elastic unload. It is within the localization band that the damage process take place up to fracture.

Problem description The simulation of a softening behaviour using a standard (local) finite element approach leads to a non physical solution. In fact, the results are pathologically dependent on the mesh size and orientation: damage localizes within the smallest band that can be represented by the mesh, which might be a unique layer of elements or a unique layer of Gauss points (see figure 2.2). Absurdly, for an infinitely small size of the mesh, the localization zone would tend to a zero width band, and so to a null dissipated energy, which is a completely non-physical solution.

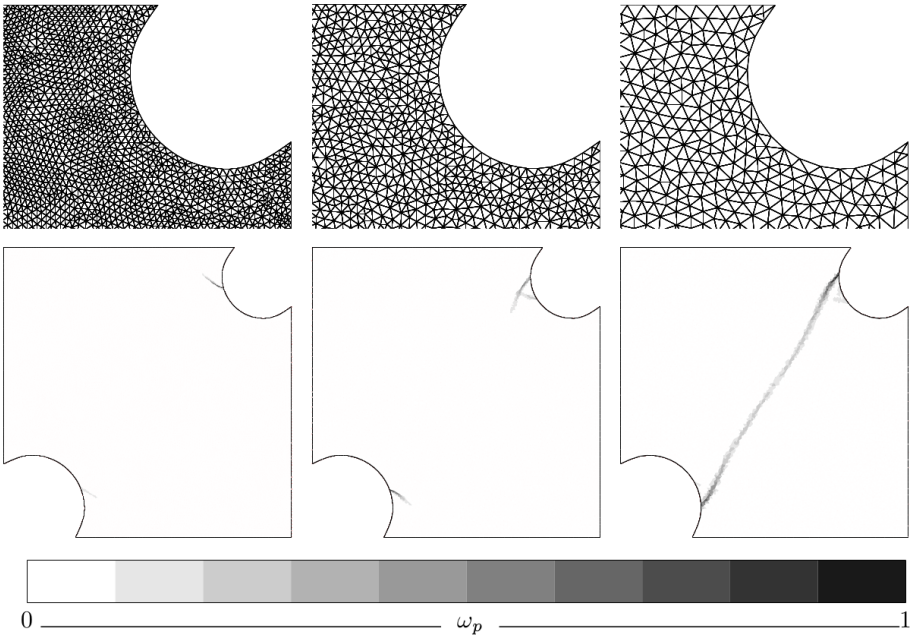

Figure 2.2: Numerical localization problem shown on a damage field. The mesh size and orientation determine the profile of damage. Credit [44]

Problem explanation From a mathematical point of view, the localization can be explained as a loss of ellipticity[5] of the constitutive equations which leads to the loss of uniqueness of the solution. The solution bifurcates [12]. From a modelling point of view, the pathological localization is due to the lack of information about the material scale. In fact, the continuum mechanics is

[5]The ellipticity condition reads:

$$\det(\underline{n} \cdot \frac{\partial \underline{\underline{\sigma}}}{\partial \underline{\underline{\varepsilon}}} \cdot \underline{n}) > 0 \qquad \forall \underline{n} \in \mathbb{R}^3 \qquad ||\underline{n}|| = 1 \tag{2.31}$$

based on the hypothesis of material's homogeneity within the Representative Elementary Volume (REV). Such an hypothesis is no longer verified when localization occurs, since the material cannot be considered as homogeneous within the REV any more.

Solution The solution to the localization problem consists in enriching the description of the continuous medium by introducing the missing additional information about the material scale, which is directly related to the effective (physical) size of the localization band. Such mechanical models are referred to as non-local models.

Regularization by enriched energy density

This approach consists in adding a phenomenological term to the free energy density of the system, which acts as regularization operator. The fundamentals of this approach were investigated by Aero et al. [3]. A developed mathematical framework for this kind of approach is described in the work of Lorentz [85]. Several publications prove the good mathematical and numerical properties [87, 88] of this approach: the constitutive relations result from a variational approach within the standard materials framework, which is valid as long as the regularization is done on an internal variable. The equations of this approach are written on the reference configuration, hence using Lagrangian quantities. Considering then the cumulated plastic strain as the variable to be regularized, the free energy density reads:

$$\Phi_{nl}(E, E^p, p, \nabla p) = \Phi_{el}(\underset{\sim}{E} - \underset{\sim}{E}_{pl}) + \Phi_{pl}(p) + \frac{c}{2}\nabla p \cdot \nabla p \tag{2.32}$$

where parameter c, which has the dimension of a force, is the regularization parameter. The regularization prescribes a constraint on the gradient of the cumulated plastic strain. The regularized hardening variable cannot undergo uncontrolled localisation since it would result in an infinite free energy. Thus, the larger the parameter c, the smoother the spatial distribution of the hardening variable.

Regularization via a spatial non-local operator

The principle of this family of approaches is to directly introduce a characteristic length (the internal length) into the model [11, 107, 116]. From a simplified point of view, the characteristic length expresses zone of mutual interaction between material points. The model is based on the definition of a spatial operator (tensor or scalar) which connects a mechanical variable to its non-local counterpart:

$$v_{nl} = \mathscr{B}(v) \tag{2.33}$$

The choice of the operator $\mathscr{B}$ determines the approach and consequently its non-local properties. However, the weakness of these approaches is the non coercive property of the regularization operator, which might not ensure the uniqueness of the solution, as proven by Lorentz et al. [86]. In the following, the convolution operator and the gradient operators are introduced.

Convolution operator: the interaction of the material points is defined by a convolution operation between a weight function w and the local variable v:

$$v_{nl} = \frac{\int_\Omega w(||x-y||\, v(y) \mathrm{d}\Omega}{\int_\Omega w(||x-y||\, \mathrm{d}\Omega} \tag{2.34}$$

where w is an odd function which maximum is in $x = y : w(0) = 1$, Ω is the interaction zone and $||x - y||$ the distance between two points. This approach has been introduced by Kroner [72] for a non-local elasticity frame. It has also been used to model brittle failure and ductile failure as well. Despite the large use of this approach, it carry some algorithmic issues that are incompatible with an efficient computation. In fact, to compute v_{nl}, it is necessary to share information between integration points. The integration of the material law is no longer independent for each integration point. Moreover, the tangent matrix is in general non-symmetric. Finally, there are additional issues related to the computation of the integral on the edges of the domain and on the non-convex portions of the domain (*e.g.* cracks).

However, the regularisation operator that will be introduced in the next paragraph does not suffer from this problems and can lead to an equivalent result in certain cases.

Gradient operators: the interaction between points is considered via the superior order derivatives of the deformations fields and the internal variables. A distinction can be made on the definition of the non-local variable, which might be explicit:

$$v_{nl} = v + c\nabla^2 v \tag{2.35}$$

or implicit:

$$v_{nl} - c\nabla^2 v_{nl} = v \tag{2.36}$$

with c the characteristic length.

The introduction of such an additional equation to the problem requires an additional boundary condition:

$$\nabla v_{nl} \cdot \underline{n} = 0 \qquad \text{on} \qquad \partial\Omega \tag{2.37}$$

Both gradient operators can be derived from the convolution operator. Compared to the explicit gradient approaches, implicit gradient approaches have several advantages [40]. Indeed, they impose additional boundary conditions only on the domain's edge and not on the elastic-plastic boundaries as for explicit gradient approaches. Furthermore, implicit gradient has a local mathematical formulation which leads to an efficient numerical implementation since no information needs to be exchanged between integration points.

Regularization via a micromorphic potential

The approaches belonging to this family aim at enriching the kinematic description at macro scale using additional degrees of freedom issued from the kinematic description at micro scale. The pioneer work is attributed to the Cosserat brothers [32], that associated a micro-rotation tensor to each material point. A more recent, and generic, framework has been proposed by Forest [47]. Once the micromorphic variable is chosen, the formulation of the Helmholtz free energy is enriched by a micromorphic potential which connects the microscale variable with is macroscopic counterpart. This operation introduces the effects of the neighbour points generating a non-local regularization.

Thick Level Set regularization

Thick level set is a numerical model for damage, introduced by Möes [101], based on the definition of a damage front (the level set) which separates the undamaged zone from the damaged zone.

Damage is modelled as a function of the orthogonal distance from the damage front. Furthermore, damage is supposed to be confined within a zone of finite dimension l_c in the wake of the front, which is referred to as the Thick Level Set (TLS). The non-local properties of the TLS method are given by a constraint imposed on the gradient of the damage function.

In this work the regularization by enriched energy density is considered. It is the regularization considered in the work of Zhang [136, 137], where the positive results obtained for the simulation of ductile failure within the finite strain framework are encouraging.

2.3.2 The volumetric locking problem

2.3.2.1 Description of the problem

The Volumetric locking is a numerical problem that affects the simulations of quasi-incompressible behaviours when the finite element approach is solely formulated in terms of displacement. It arises in the present study because of the incompressibility of the plastic flow. The volumetric locking problem induces spurious oscillations of the solution fields, as visible in figure 2.3(a). The displacement solution is underestimated and, on the contrary, the stiffness is overestimated. In fact, the problem derives from the inability of the standard finite element to find a displacement solution coherent with the a quasi-null volume variation. The mathematical theory of this problem have been investigated by Babuska [9] and Brezzi [22].

2.3.2.2 Solutions to the problem

A simple solution to prevent volumetric locking is obtained by reducing the number of integration points. An alternative solution, referred to as selective integration, aims at reducing the number of integration point only for the hydrostatic part of deformation, which is responsible of the volumetric locking. The deviatioric part is fully integrated. These techniques restores the singularity of the stiffness matrix, avoiding locking. Nevertheless, the reduced integration might lead to zero energy parasite modes which requires an additional stabilization of the finite element. Furthermore, such techniques are applicable only to quadrangular element. For this reason, they are not considered in this study, since the long term objective is to use automatic remeshing, which requires triangular elements. The last solution to mention is represented by the so called mixed formulations. Introduced by Washizu [133], this solution aims at enriching the finite element formulation by introducing additional fields (dilatation and pressure) as unknowns of the problem. This latter solution is part of the numerical approach provided by Zhang [136, 137], adopted in this study, which consider a mixed non-local method to regularize both the volumetric locking problem and the strain localization problem (see figure 2.3(b)).

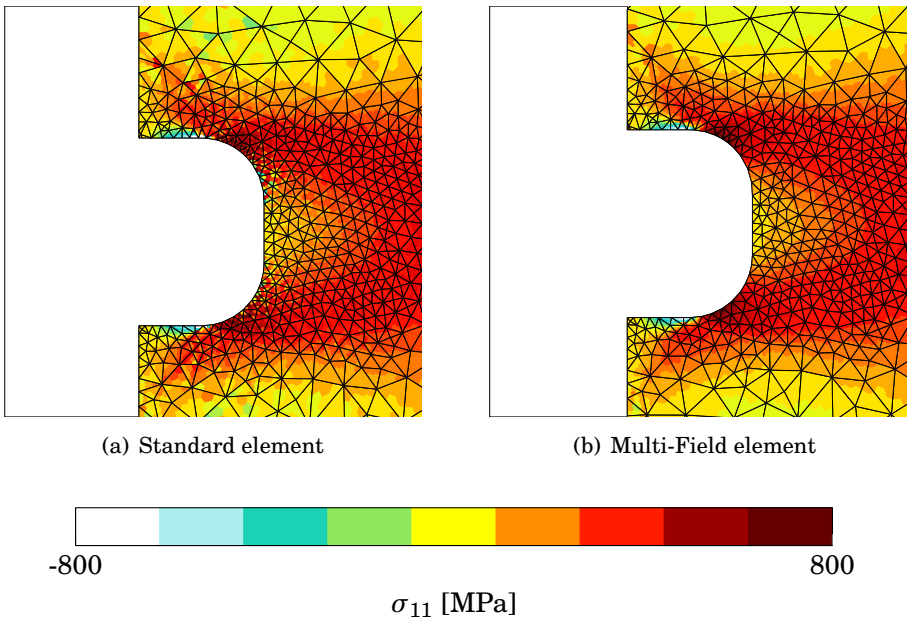

(a) Standard element (b) Multi-Field element

(c)

Figure 2.3: Aspect of σ_{11} field using a standard element affected by the volumetric locking problem (left) and using the mixed element considered in this work (right).

Résumé

Ce deuxième chapitre porte sur le modèle matériau et sur l'approche éléments finis utilisés afin de reproduire le comportement observé expérimentalement.
Le seuil de plasticité est défini par le critère de Hosford. Ce critère permet notamment, grâce à un seul paramètre supplémentaire, de reproduire des comportements matériaux dont les surfaces de charge sont situées entre celles des critères de Tresca et de Von Mises. Le fort écrouissage est modélisé par une loi exponentielle de type Voce, où deux termes non-linéaires permettent de décrire l'écrouissage à des faibles et hauts niveaux de déformation respectivement. L'endommagement est modélisé par un modèle de type GTN, où la germination, la croissance et la coalescence de vides sont prises en compte. Les caractères tardifs et rapides de la rupture de l'Inconel625 ont été modélisés par une forte germination de nouvelles cavités commençant à un niveau de plasticité cumulée relativement important.
Les grandes déformations associées aux matériaux ductiles nécessitent des approches éléments finis spécifiques, capables d'en décrire la cinématique. Dans cette thèse le choix porte sur l'approche additive logarithmique proposée par Miehe et al. Néanmoins, la simulation d'un matériau ductile adoucissant en présence de forts écoulements plastiques pose des problèmes de localisation et de verrouillage. Le premier problème peut être résolu au travers d'approches non-locales bien connues, tandis que le deuxième problème peut être traité par une formulation mixte, où les déplacements nodaux ne sont pas les seules inconnues du problème d'équilibre.
Le choix de la formulation éléments finis c'est donc porté sur la formulation proposée dans la thèse de Zhang, où l'approche en grandes déformations de Miehe et al. est régularisée sur le gradient de la plasticité afin d'éviter le problème de localisation. De plus, pression et dilatation sont considérées comme inconnues afin d'éviter le problème de verrouillage.

CHAPTER 3

PRESCRIPTION OF MEASURED BOUNDARY CONDITIONS

This chapter deals with the prescription of measured displacements issued from DIC measurements as boundary conditions for the finite element simulation. To do so, the DIC fields are mapped onto the finite element mesh as described in appendix B. Applying measured boundary conditions is important for parameter identification since it assures a consistent comparison between the considered test and its simulation. In fact, measured boundary conditions allow to take into account a possible rigid body motion caused by a slipping of the specimen within the machine clamps. Furthermore, measured boundary conditions allow to completely exclude the testing machine from the finite element model[1]. Nevertheless, the measured values of the displacement fields are altered by the uncertainty of the measurement system, which is here referred to as measurement noise. The results of the FOLKI-D (DIC) algorithm, where no post-filtering operations are performed, evidence this problem. The first part of this chapter analyses the negative impact of the measurement noise onto the solution of the mechanical problem. The second and last part of this chapter illustrates and compares two possible approaches to limit the detrimental effect of noised boundary conditions.

3.1 Introduction

Digital Image Correlation (DIC) is a powerful tool to measure surface full field displacements on both laboratory size samples and real life structures [51]. The richness of information provided by this technique allows not only to analyse local phenomena [61], but also prescribe the measured displacements as Dirichlet boundary conditions (assuming constant displacements in depth[2]), as in [110] and [43]. Alternatively, the boundary conditions can be considered as unknowns of the inverse problem and determined by the resolution of the Cauchy's problem as in [29] and [5].

Nevertheless, prescribing noised measured boundary conditions (the measurement values are altered by the measurement uncertainty) may produce undesirable and unpredictable effects. Regardless of its amplitude, noise may alter significantly the solution. This contribution analyses

[1] Because of its own stiffness, the testing machine could not be excluded *a priori* from the finite element model without generating a relatively important approximation if nominal displacements were to be prescribed.

[2] This latter hypothesis is acceptable in most of the cases when thin specimens are considered, see [134]

the impact of noised boundary conditions in the case of mechanical problems. Their impact is exposed in section 3.2 on both an analytical and a finite element problem. The proposed filtering solutions are evaluated in section 3.3. To do so, a reference unnoised solution is generated using finite element simulation. The corresponding boundary conditions are perturbed with a random Gaussian noise to generate noised solutions which are then compared to the reference based on the definition of an alteration coefficient. Finally, in section 3.4, the proposed methodology is discussed and applied to an actual case study using a complex specimen geometry.

3.2 Impact of noise on the solution of the equilibrium problem

Noised boundary conditions produce an alteration on the solution. This section exposes the problem on different cases.

3.2.1 Analytical test case: elasticity problem under antiplane shear condition

This part focuses on an antiplane shear problem (the Poisson's problem) for which an analytical solution exists.

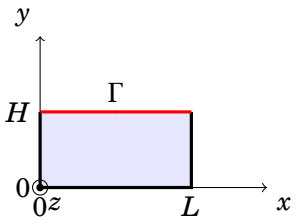

Figure 3.1: Cross section of the Poisson problem bar.

Let us consider a bar with rectangular cross section $L \times H$ as in figure 3.1, where Γ designates the top edge (red boundary). An antiplane strain state can be achieved by considering an out-of-plane displacement field:

$$u_x = 0, \quad u_y = 0, \quad u_z = u_z(x,y) = u(x,y) \tag{3.1}$$

As boundary conditions, the following nonzero displacement is prescribed on Γ (red boundary), while a null displacement is prescribed on the remaining portion of the boundary (black boundary).

$$u_{|\Gamma} = \sum_{n=0}^{N} u_n = \sum_{n=0}^{N} u_n^0 \sin\left(\frac{\pi n}{L} x\right) \tag{3.2}$$

According to the small strain theory, the relations between strain and displacement read:

$$\varepsilon_{xz} = \frac{1}{2}\frac{\partial u}{\partial x} \qquad \varepsilon_{yz} = \frac{1}{2}\frac{\partial u}{\partial y} \tag{3.3}$$

Considering an elastic behaviour, the nonzero stress components σ_{xz} and σ_{yz} can be directly expressed as functions of the corresponding strain components as:

$$\sigma_{xz} = 2\mu\varepsilon_{xz} \qquad \sigma_{yz} = 2\mu\varepsilon_{yz} \tag{3.4}$$

where μ is the shear Lamé constant. Considering null bulk forces the equilibrium equation reads:

$$\Delta u_n(x,y) = 0 \tag{3.5}$$

which is the homogeneous Poisson's equation. It can be solved by separation of variables to obtain the expression of displacement at equilibrium. The solution is written as:

$$u(x,y) = \sum_{n=0}^{N} u_n(x,y) \quad \text{with} \quad u_n(x,y) = u_n^0 \frac{\sinh(\frac{\pi n}{L} y)}{\sinh(\frac{\pi n}{L} H)} \sin\left(\frac{\pi n}{L} x\right) \tag{3.6}$$

The partial derivatives are:

$$\frac{\partial u_n}{\partial x}(x,y) = u_n^0 \frac{\pi n}{L} \frac{\sinh(\frac{\pi n}{L} y)}{\sinh(\frac{\pi n}{L} H)} \cos\left(\frac{\pi n}{L} x\right) \tag{3.7}$$

$$\frac{\partial u_n}{\partial y}(x,y) = u_n^0 \frac{\pi n}{L} \frac{\cosh(\frac{\pi n}{L} y)}{\sinh(\frac{\pi n}{L} H)} \sin\left(\frac{\pi n}{L} x\right) \tag{3.8}$$

Equations 3.7 and 3.8 allow to evaluate the impact of noise on stress and strain. Let us consider noise as a term of the same form as the prescribed boundary condition with high spatial frequency p (with $p \gg N$) and relatively small amplitude u_b. Since the frequency is in the numerator of the derived field expressions, the considered noise will affect significantly the solution even for small values of amplitude. Figure 3.2 shows the difference between the noised solution and the reference (*i.e.* without noise), both evaluated on the top edge Γ for a particular set of (u_n^0, n) values. As expected, the impact of noise is higher for the derived fields.

Furthermore, all the solution fields depend on hyperbolic functions of y. This implies that the impact of noise is maximum on the edge where boundary conditions are prescribed and that it vanishes as y decreases from H to 0, as illustrated in figure 3.3. These observations are consistent with the literature [62], where it is shown that errors tend to concentrate in the vicinity of boundary where measured boundary conditions are applied.

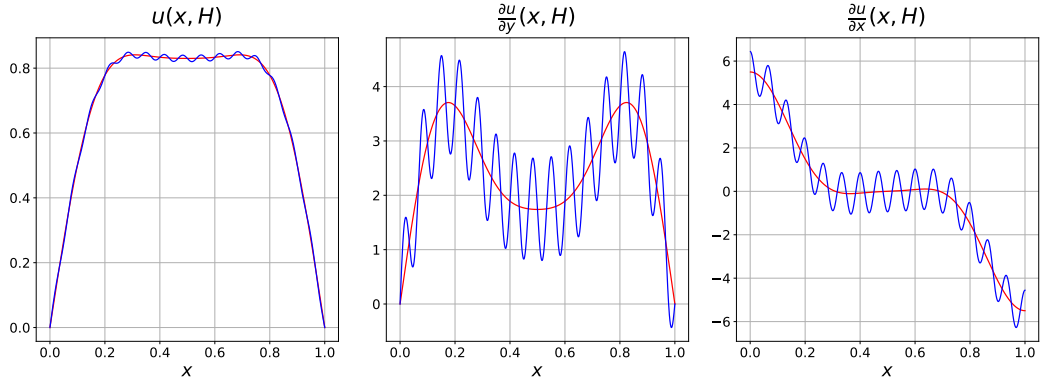

Figure 3.2: Comparison between the noised solution (blue) and the reference (red) for different fields on the top edge Γ ($y = H$). Noise impact is higher for the derived fields. Data: $N = 5$, $u_1^0 = 1$, $u_3^0 = 0.2$, $u_5^0 = 0.03$, $u_0^0 = u_2^0 = u_4^0 = 0$, $p = 30$, $u_b = 0.01$, $H = 1$, $L = 1$.

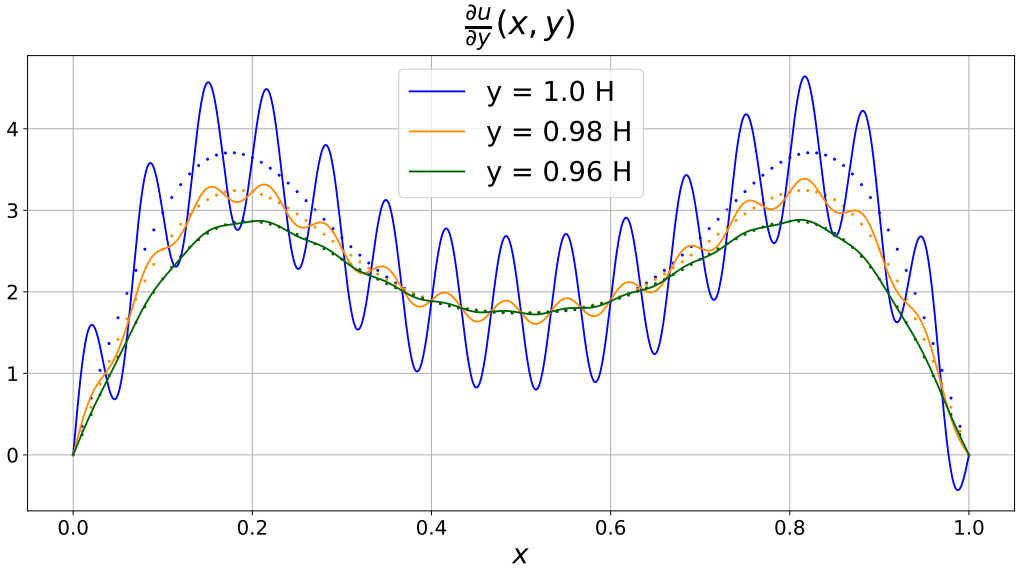

Figure 3.3: Noised solution at different distances (solid lines) from the top edge Γ ($y = H$) where boundary conditions are prescribed compared with their respective reference solution (dotted lines). Noise impact vanishes as y decreases from H to 0.

3.2.2 Numerical test case including plasticity

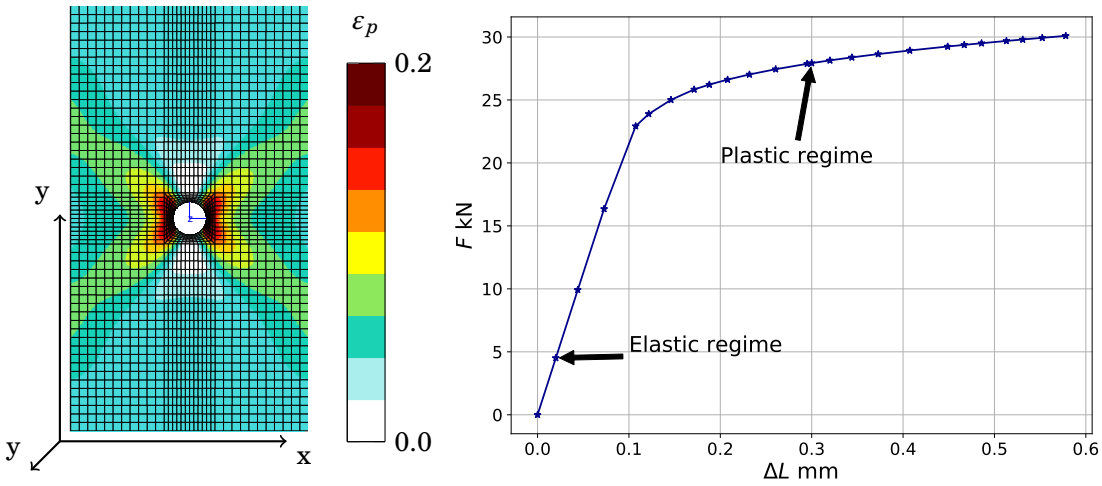

Figure 3.4: On the left, the considered mesh and cumulated plasticity field for a reference load. The whole geometry undergoes plastic deformation. On the right, the macroscopic response, where the two investigated loading steps are indicated. Specimen is 28mm wide, 50 mm high and 2 mm thick. The hole diameter is $\phi = 4$ mm.

The objective of this section is to illustrate the negative impact of noise within a context closer to an actual mechanical test. A tensile test on a perforated flat specimen is investigated (see figure 3.4). The bottom edge of the specimen is clamped so that $u_{x,y=0} = u_{y,y=0} = 0$, while a vertical uniform displacement ($u_{y,y=H}$) is applied on the top edge for the reference case (with $u_{x,y=H} = 0$). Rigid body motion along the third direction (z) is prevented. The considered constitutive model is detailed in chapter 2. The solution of the problem submitted to reference boundary conditions (without noise) is compared to the solution of the problem with noised boundary conditions. Such boundary conditions are generated adding, for each time step, a Gaussian noise to the reference boundary conditions. Noise has a null mean value and a standard deviation of $\varsigma = 10^{-3}$ mm. This magnitude is chosen to be representative of an experimental uncertainty for DIC measurements. A relative and an absolute alteration coefficients ($\delta_{r,\mathbb{C}}$, $\delta_{a,\mathbb{C}}$) are then defined to quantify noise impact:

$$\delta_{r,\mathbb{C}} = \left| \frac{\mathbb{C}_{\text{noise}} - \mathbb{C}_{\text{ref}}}{\mathbb{C}_{\text{ref}}} \right| \qquad \text{and} \qquad \delta_{a,\mathbb{C}} = |\mathbb{C}_{\text{noise}} - \mathbb{C}_{\text{ref}}| \tag{3.9}$$

where $\mathbb{C}$ is the finite element result of interest (force, displacement, deformation, ...). Subscripts indicate whether the prescribed boundary condition is polluted by noise or not. The absolute alteration coefficient $\delta_{a,\mathbb{C}}$ allows to evaluate the magnitude of the alteration provoked by noise. Such an absolute value may be constant for all the loading steps. Instead, the relative alteration coefficient $\delta_{r,\mathbb{C}}$ allows to evaluate the magnitude of the alteration with respect to a reference value. In fact, the problems issued from the measurement noise are more significant in correspondence of the low values of the considered quantity. Moreover, let us note that a reference solution cannot be defined when experimental boundary conditions are prescribed.

Considering the macroscopic response of the reference simulation (see figure 3.4) two loading steps are considered: the first one is within the elastic regime while the second one is within the plastic regime. Displacement for the loading step within the plastic regime is 15 times the displacement of the loading step within the elastic regime. Figure 3.5 shows the relative alteration coefficient evaluated at the top edge where boundary conditions are prescribed. As expected impact is lower on displacement than on stress (of about 2 orders of magnitude). Relative alteration on stress can exceed 500% within the elastic regime (low displacement value), and 180% within the plastic one (high displacement value).

As observed before, noise impact decreases with the distance from the edge where the boundary condition is applied. Figure 3.6 shows the alteration coefficient at a distance of 5 mm from the edge. Noise impact is less than 14% within the elastic regime and less than 1% within the plastic one.

Since the behaviour is, in this case, supposed not purely elastic, the noised boundary conditions may cause the formation of spurious plastic areas at the domain's edge as illustrated in figure 3.7. In cases where plasticity is coupled with damage, failure prediction may be compromised.

3.3 Noise filtering

Alteration caused by noised boundary condition can be reduced by low-pass filtering. Two approaches can be then distinguished. The first one aims at reconstructing the data while the second one is based on the mechanical filtering of the problem.

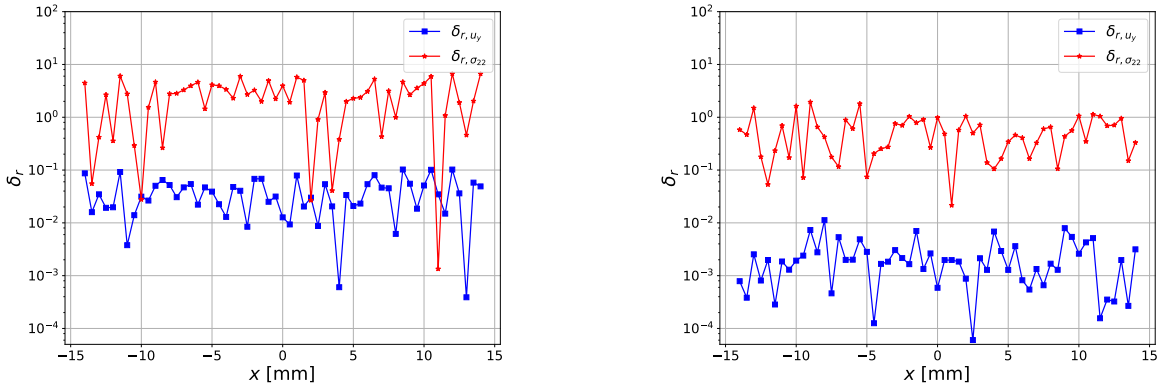

(a) Elastic regime

(b) Plastic regime

Figure 3.5: Relative alteration coefficient δ_r for vertical displacement u_y (blue) and stress component σ_{22} (red) evaluated at the top edge, where boundary conditions are prescribed. Noise alters significantly the finite element solution. At high displacement values (plastic regime) the perturbation due to noise is less severe.

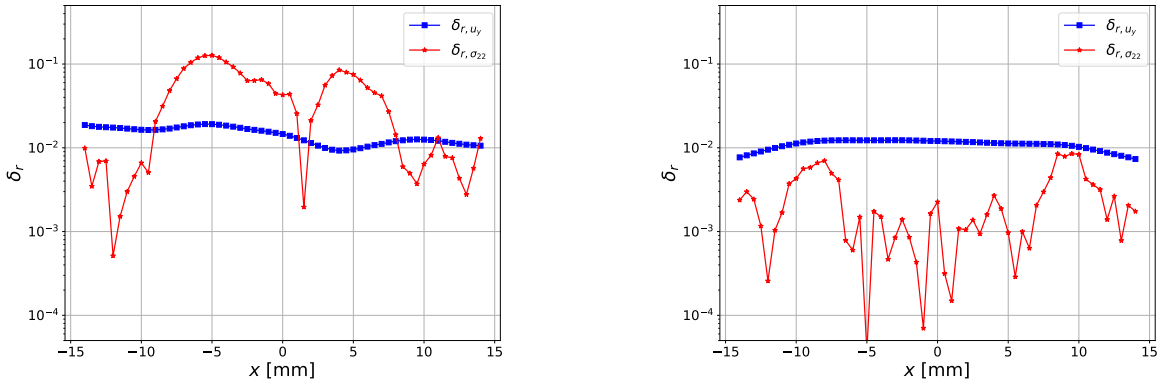

(a) Elastic regime

(b) Plastic regime

Figure 3.6: Relative alteration coefficient δ_r for vertical displacement u_y (blue) and stress component σ_{22} (red) evaluated at 5 mm from the edge. Noise impact vanishes with distance.

3.3.1 Data reconstruction

The most commonly used technique of data reconstruction consists in approximating the boundary condition by a polynomial function of relatively low order m (usually with $m < 5$). Let us note that a robust approach for polynomial reconstruction is to define the function with respect to the curvilinear coordinates system associated to the boundary to deal with complex boundary geometries. The extrapolation by polynomial functions of constant order has been applied by [62] to boundary conditions issued from global volumetric image correlation. Restricting the choice to low order functions allows preventing approximation errors. As observed by Runge [118] when using polynomial interpolation with polynomials of high degree on a set of equispaced points the

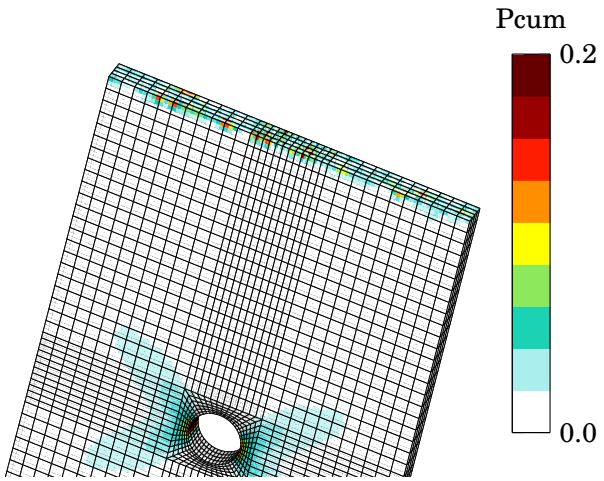

Figure 3.7: Spurious cumulated plasticity at the edge where noised boundary conditions are prescribed. Values on the edge are of the same magnitude than values around the hole.

error of approximation increases with the order of the polynomial, with a concentration at the edge of the domain. Figure 3.8 shows the alteration coefficient on the stress component σ_{22} for function orders $m = 0$, 1 et 2 on the perforated specimen. This specimen has a straight boundary which is loaded with a uniform displacement for the reference case (figure 3.4). Therefore, the zero order polynomial function gives the best filtered result. Comparing the alteration coefficient for the unfiltered solution (figure 3.5) with the filtered one (figure 3.8) shows that alteration is reduced by 2 orders of magnitude.

However, let us note that the domain of application of the polynomial reconstruction might be limited because of the low order constraint. In fact, the geometrical singularities such as notches or holes could alter significantly the regularity of the boundary condition and impede such an approximation.

A second technique for the data reconstruction approach is the reconstruction by the Moving Least Square algorithm [83]. The extrapolation is carried out piece-wise by defining a window which dimension is lower than the data set size. On the one hand, moving least squares offers more flexibility to fit complex functions, but on the other hand, it requires a prior analysis of the boundary condition to determine the optimal parameters (window size and polynomial order). When the window is undersized for the chosen function order, the moving least square will reproduce noise instead of smoothing it. On the opposite, when the window is oversized, the boundary conditions could be distorted (*e.g.* if the whole data set is used, the result is the same than the polynomial reconstruction). Figure 3.9 shows the alteration coefficient for different window sizes for the moving least squares algorithm. In the present study, the window size is expressed in terms of the number of points used for the local reconstruction. As expected, an undersized window ($w = 3$) leads to a reduced and unsatisfactory noise reduction (see figure 3.9). A larger window sizes allow a proper smoothing of the noise impact. Since the present loading is a constant displacement applied on a straight boundary, the best result is given by a low polynomial order combined with a large window size.

Let us compare in figure 3.10 the best filtering result of moving least squares with the best result obtained using a single polynomial over the whole data set. The higher noise impact

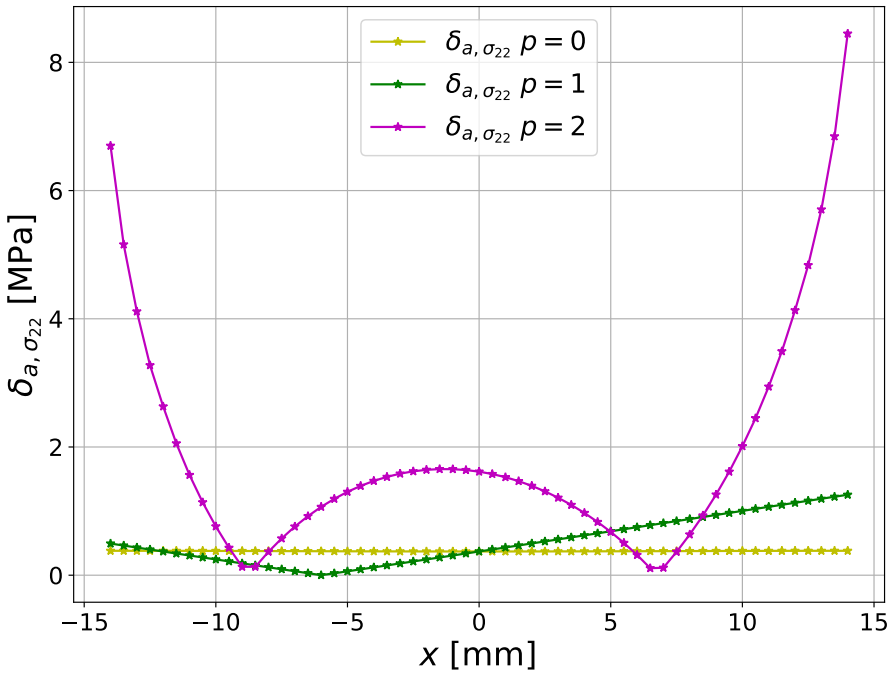

Figure 3.8: Absolute alteration coefficient on a stress component $\delta_{a,\sigma_{22}}$ for different orders of the smoothing polynomial function. For the considered case the function order 0 represents at best the reference data and so it provides the best filtering result.

reduction is given by the polynomial reconstruction, since it reproduce at best the reference displacement. This example points out the fact that data reconstruction approaches cannot be automated since the choice of the parameters largely depends on the measured data.

Finally, let us note that the data reconstruction techniques could allow the extrapolation of the boundary condition where data is missing (*e.g.* where Digital Images Correlation could not provide a result, like on the edges of the specimen).

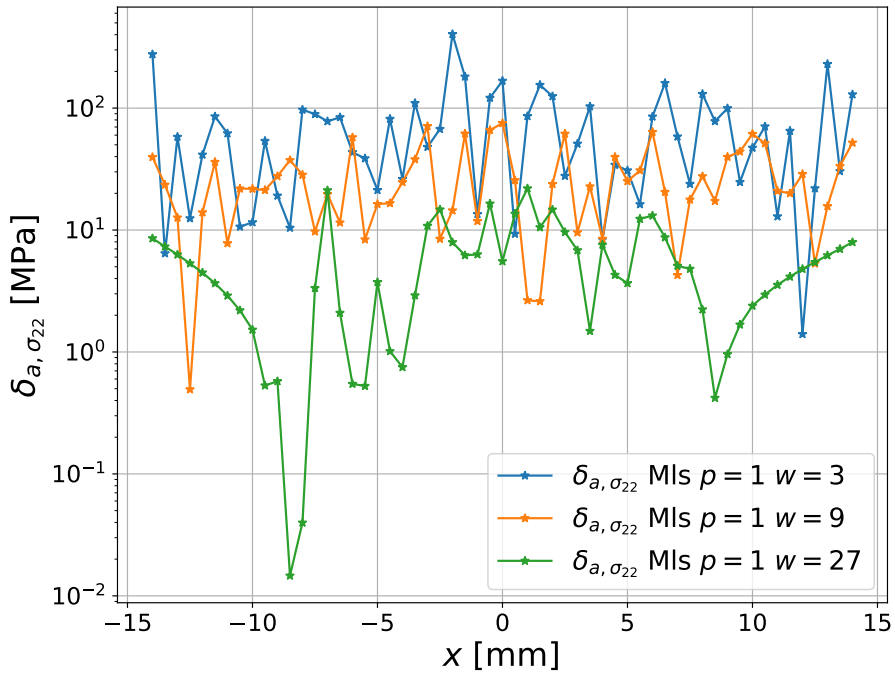

Figure 3.9: Absolute alteration coefficient $\delta_{a,\sigma_{22}}$ for different parameters for the moving least squares algorithm. An undersized window leads to an unsatisfactory reduction of noise impact.

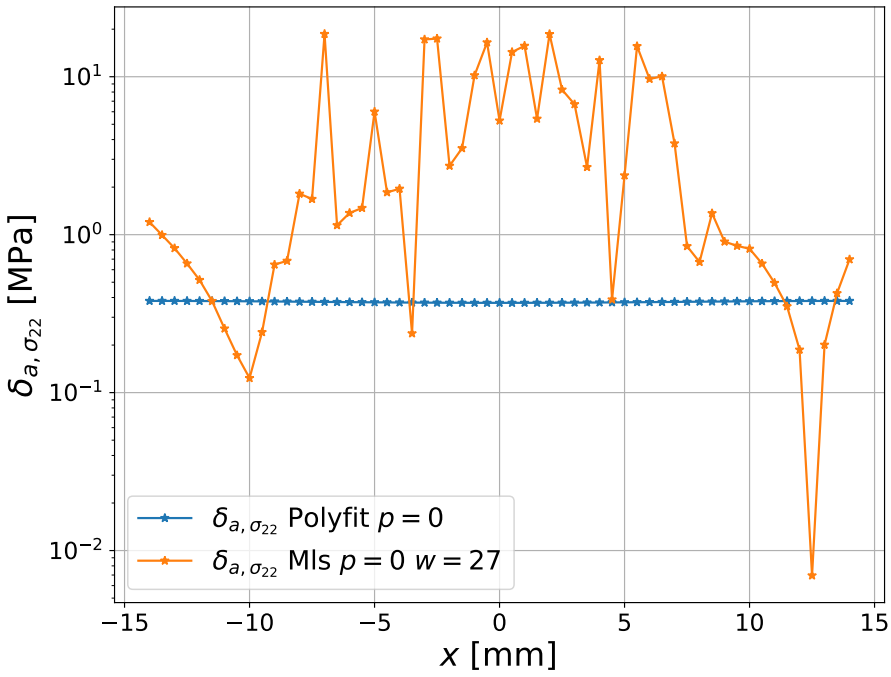

Figure 3.10: Comparison of absolute alteration coefficient $\delta_{a,\sigma_{22}}$ between moving least square and polynomial approximation. Since for the present case the reference solution is a constant displacement the reconstruction by a single polynomial is more appropriate than moving least square.

3.3.2 Mechanical filtering

The most straightforward approach involving mechanical filtering could be the prescription of a sheer elastic behaviour on a finite portion of the specimen's geometry around the boundary of the domain. The idea is to numerically prevent the development of artificial cumulated plasticity by forcing an elastic behaviour. However, such a solution is not applicable when expected cumulated plasticity can develop within that zone: for example in figure 3.4, the whole perforated specimen is undergoing plastic deformation. Moreover, this solution tends to lock the out-of-plane displacement at the boundary between the elastic and plastic layer. As a consequence, the elastic layer solution is excluded from this study.

To overcome this problem, a different approach could be the prescription of the measured boundary conditions via an elastic attachment. It can be seen as if displacement is applied to the structure via an elastic spring placed upon the boundary. The described loading can be represented by a Robin boundary condition, also known as mixed boundary condition or Fourier boundary condition [58]. It is commonly used for thermodynamic problems[3]. For a mechanical problem, the Robin boundary condition reads[4]:

$$l_R \underset{\sim}{\sigma} \cdot \underset{\sim}{n} = \frac{1}{S_\Gamma}(\underset{\sim}{u}_m - \underset{\sim}{u}) \tag{3.10}$$

where l_R is referred to as the Robin coefficient and S_Γ is the characteristic dimension of the boundary where displacement is prescribed. Quantities S_Γ and l_R are respectively homogeneous to $[mm^2]$ and $[mm/N]$ for 3D problems, while they are homogeneous to $[mm]$ and $[mm^2/N]$ for 2D problems.

Let us recall the anti-plane shear problem in section 3.2, but replacing the Dirichlet boundary condition on the top edge with the Robin boundary condition of equation 3.10. The solution at equilibrium now depends on the Robin coefficient l_R and reads:

$$u_n(x,y,l_R) = u_n^0 \frac{1}{1+\frac{\mu\pi n l_R}{\tanh(\frac{\pi n}{L}H)}} \frac{\sinh(\frac{\pi n}{L}y)}{\sinh(\frac{\pi n}{L}H)} \sin\left(\frac{\pi n}{L}x\right) \tag{3.11}$$

while the partial derivatives:

$$\frac{\partial u_n}{\partial x}(x,y,l_R) = u_n^0 \frac{\pi n}{L} \frac{1}{1+\frac{\mu\pi n l_R}{\tanh(\frac{\pi n}{L}H)}} \frac{\sinh(\frac{\pi n}{L}y)}{\sinh(\frac{\pi n}{L}H)} \cos\left(\frac{\pi n}{L}x\right) \tag{3.12}$$

$$\frac{\partial u_n}{\partial y}(x,y,l_R) = u_n^0 \frac{\pi n}{L} \frac{1}{1+\frac{\mu\pi n l_R}{\tanh(\frac{\pi n}{L}H)}} \frac{\cosh(\frac{\pi n}{L}y)}{\sinh(\frac{\pi n}{L}H)} \sin\left(\frac{\pi n}{L}x\right) \tag{3.13}$$

The low pass filtering property of the Robin boundary condition can be evaluated by means of the Dirichlet-to-Neumann operator, which is defined as the operator that associates the prescribed displacement on the top edge $u_{|\Gamma}$ (equation 3.2) to the derived solution (stress σ_{yz} for instance) evaluated on Γ (*e.g.* equation 3.13):

$$\lambda_{RN,yz,n} = \frac{\sigma_{yz,n}}{u_{|\Gamma,n}} = \mu \frac{1}{u_{|\Gamma,n}} \frac{\partial u_n}{\partial y} = \mu \frac{\pi n}{L} \frac{1}{1+\frac{\mu\pi n l_R}{\tanh(\frac{\pi n}{L}H)}} \frac{1}{\tanh(\frac{\pi n}{L}H)} \tag{3.14}$$

[3]The heat exchanged across a wall is proportional to the temperature gap.

[4]The present numerical implementation applies the Robin boundary condition direction-wise.

The value of such operator for the filtered problem ($l_R \neq 0$), calculated at high frequencies ($n \to \infty$), is bounded to a constant value:

$$\lim_{n\to\infty} \lambda_{RN} = \frac{1}{l_R L} \qquad \text{and} \qquad \lim_{l_R \to 0^+} \frac{1}{l_R L} = +\infty \tag{3.15}$$

It is clear from equation 3.15 that the Robin boundary condition reduces the impact of noise setting a limit to its detrimental contribution.

Nevertheless, let us underline that the Robin boundary condition is not a Dirichlet condition. Hence, the original problem itself is modified using a Robin boundary condition, regardless of the noise. To prove it, let us evaluate the difference in terms of amplitude r_u between the solution with Robin boundary condition ($l_R \neq 0$) and the solution with Dirichlet boundary condition ($l_R = 0$):

$$r_u(l_R, n) = \frac{u_n(x, y, l_R \neq 0)}{u_n(x, y, l_R = 0)} = \frac{1}{1 + \frac{\mu \pi n l_R}{\tanh(\frac{\pi n}{L} H)}} \tag{3.16}$$

to observe that the value decreases from 1 to 0 as l_R increases from 0 to ∞. Therefore, the considered Robin boundary conditions degenerates into a Dirichlet condition for $l_R = 0$, while it degenerates to an homogeneous Neumann condition for $l_R \to \infty$ (*i.e.* the prescribed displacement is completely adsorbed by the Robin spring).

However, the Robin boundary condition might be an acceptable approximation of a Dirichlet condition for relatively small values of the Robin coefficient l_R. Yet, the smaller l_R is, the less noise impact is reduced: a compromise has to be reached. The present work proposes to guide the compromise by the Discrepancy Criterion of Morozov [100]. The idea beyond such a criterion is to not require the solution to be more accurate than the measured boundary condition itself, which originates from a device with a finite precision. The discrepancy criterion reads:

$$\left|\left| \underset{\sim}{u}_b - \underset{\sim}{u}_{l_R} \right|\right|_\Gamma \leq k\varsigma \tag{3.17}$$

meaning that the solution $\underset{\sim}{u}_{l_R}$ (evaluated on the boundary Γ) is acceptable if the difference with the measured (and prescribed) displacement $\underset{\sim}{u}_b$ remains within an acceptable range. To provide a physically reasonable value for this latter range, it is calculated as k times the standard deviation ς of the measured data. The norm is calculated as a *p-norm*. The order of the norm is arbitrary. Therefore, an Euclidean ($p = 2$) norm is considered in this work.

The evaluation of the optimal Robin coefficient is obtained by assuming an elastic behaviour. In this case, the variational formulation of an elastic problem with Robin boundary conditions reads:

$$a(\underset{\sim}{u}_{l_R}, \underset{\sim}{v}) + \frac{1}{l_R S_\Gamma} \int_\Gamma (\underset{\sim}{u}_{l_R} - \underset{\sim}{u}_b) \underset{\sim}{v} \, \mathrm{dS} = l(\underset{\sim}{v}) \tag{3.18}$$

where Γ is the portion of boundary where the Robin boundary condition is prescribed, $\underset{\sim}{v}$ is a test function, $l(\underset{\sim}{v})$ the work of the external forces, and $a(\underset{\sim}{u}_{l_R}, \underset{\sim}{v})$ the following bilinear form:

$$a(\underset{\sim}{u}_{l_R}, \underset{\sim}{v}) = \int_\Omega \mathbb{C} : \underset{\approx}{\varepsilon}(\underset{\sim}{u}_{l_R}) : \underset{\approx}{\varepsilon}(\underset{\sim}{v}) \, \mathrm{d}\Omega \tag{3.19}$$

The solution of the system of equations 3.18 and 3.17 is not linear with respect to variables $(\underset{\sim}{u}_{l_R}, l_R)$ because of the non-linear dependence of $\underset{\sim}{u}_{l_R}$ with respect to l_R. Nevertheless, since the

current objective is to get a relatively small value of l_R, it is possible to substitute $\underset{\sim}{u}_{l_R}$ by an asymptotic development around $l_R = 0$. The following ansatz is proposed:

$$\underset{\sim}{u}_{l_R} = \underset{\sim}{u}_0 + l_R \underset{\sim}{u}_1 + l_R^2 \underset{\sim}{u}_2 + \cdots + l_R^n \underset{\sim}{u}_n \tag{3.20}$$

Appendix D shows that the ansatz is valid since it is possible to determine all the coefficients $\underset{\sim}{u}_n$. The asymptotic development is here truncated at the first two terms of the series, $\underset{\sim}{u}_0$ and $\underset{\sim}{u}_1$.

$$\underset{\sim}{u}_0|_\Gamma = \underset{\sim}{u}_b \qquad \text{and} \qquad \underset{\sim}{u}_1|_\Gamma = -S_\Gamma \underset{\approx}{\sigma}(\underset{\sim}{u}_0)|_\Gamma \cdot n \tag{3.21}$$

They are obtained from the solution of the problem where the noised displacements are applied on Γ as a Dirichlet boundary condition. Therefore, the Morozov condition is approximated as:

$$\left|\left|\underset{\sim}{u}_b - \underset{\sim}{u}_0 + l_R \underset{\sim}{u}_1\right|\right|_\Gamma = \left|\left|l_R \underset{\sim}{u}_1\right|\right|_\Gamma \leq k\varsigma \tag{3.22}$$

leading to the expression of the optimal Robin coefficient value:

$$l_R = \frac{k\varsigma}{S_\Gamma \left|\left|\underset{\approx}{\sigma}(\underset{\sim}{u}_0) \cdot \underset{\sim}{n}\right|\right|_\Gamma} \tag{3.23}$$

However, the hypothesis of purely elastic behaviour is not met in the cases studied in the present work, because of the elasto-visco-plastic behaviour of the structure and the early development of spurious plasticity due to noise within the elastic regime. Therefore, $\underset{\approx}{\sigma}(\underset{\sim}{u}_0)|_\Gamma$ is here considered as the solution of the possibly non-linear problem where the noised boundary conditions have been applied as a Dirichlet condition for the smallest displacement level that can be prescribed. For instance, it is the first time step given by the images' sampling.

To summarize, the mechanical filtering via the Robin boundary condition requires three steps. The first step consists in a partial resolution (first loading step only) of the problem with noised displacements prescribed as Dirichlet boundary conditions. The second step consists in the calculation of the optimal coefficient. The third step consists in full resolution of the problem with noised displacements prescribed as Robin boundary conditions. The Robin coefficient l_R is kept constant with respect to time.

The norm $\left|\left|\underset{\approx}{\sigma} \cdot \underset{\sim}{n}\right|\right|_\Gamma$ in equation 3.23 is calculated as:

$$\left|\left|\underset{\approx}{\sigma} \cdot \underset{\sim}{n}\right|\right|_\Gamma = \sqrt{\frac{1}{S_\Gamma} \int_\Gamma \left(\underset{\approx}{\sigma} \cdot \underset{\sim}{n}\right)^2 \mathrm{d}S} \tag{3.24}$$

where the normalization by S_Γ yields a norm that does not change the measurement unit. For a discretized surface, where potentially each element e has a different size, the norm can also be computed as:

$$\left|\left|\underset{\approx}{\sigma} \cdot \underset{\sim}{n}\right|\right|_\Gamma = \sqrt{\frac{1}{S_\Gamma} \sum_{\Gamma_e} \sum_{i=1}^{n_{gp}} \left(J_i \omega_i \underset{\approx}{\sigma}_i \underset{\sim}{n}_i\right)_e} \tag{3.25}$$

where i is an index over the Gauss points n_{gp} of the element e. Notation J indicates a Jacobian term mapping the deformed configuration into the reference configuration, while notation w indicates the weight associated to the Gauss points. Furthermore, let us note that the finite element calculation of such a quantity requires a first extrapolation of the stress values from the

Gauss points of the element to the nodes of the element common with the surface Γ, and a second interpolation of the stress values from the nodes of the surface to the Gauss points of the surface.

The optimal Robin coefficient for the tensile test on the perforated flat specimen values $l_R = 2.78 \times 10^{-7}$ mm/N, considering $k = 2$ and $\varsigma = 10^{-3}$ mm. Such coefficient produces a reduction of the noise impact, as can be seen in figure 3.11. The discrepancy condition is indeed verified since $||\underset{\sim}{u}_b - \underset{\sim}{u}_{l_R}||_\Gamma \approx 1.5 \times 10^{-3}$ mm which respects the initial condition ($k\varsigma = 2 \times 10^{-3}$ mm). Furthermore, it might be interesting to evaluate if locally the solution on the boundary is close to the measured (so prescribed) displacement. To do, the solution on the boundary is compared with the scattering band of the measure on the same boundary, as visible in figure 3.12. Since 85% of the solution values are within the scattering band the solution with Robin boundary conditions is considered as satisfactory.

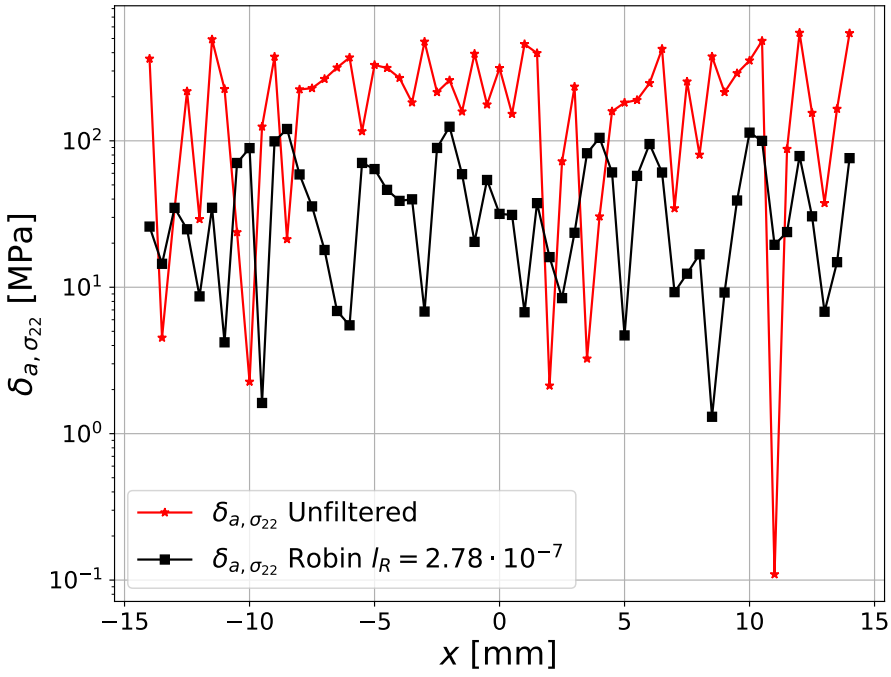

Figure 3.11: Absolute alteration coefficient $\delta_{a,\sigma_{22}}$ for a Robin boundary condition with $l_R = 2.78 \times 10^{-7}$ mm/N.

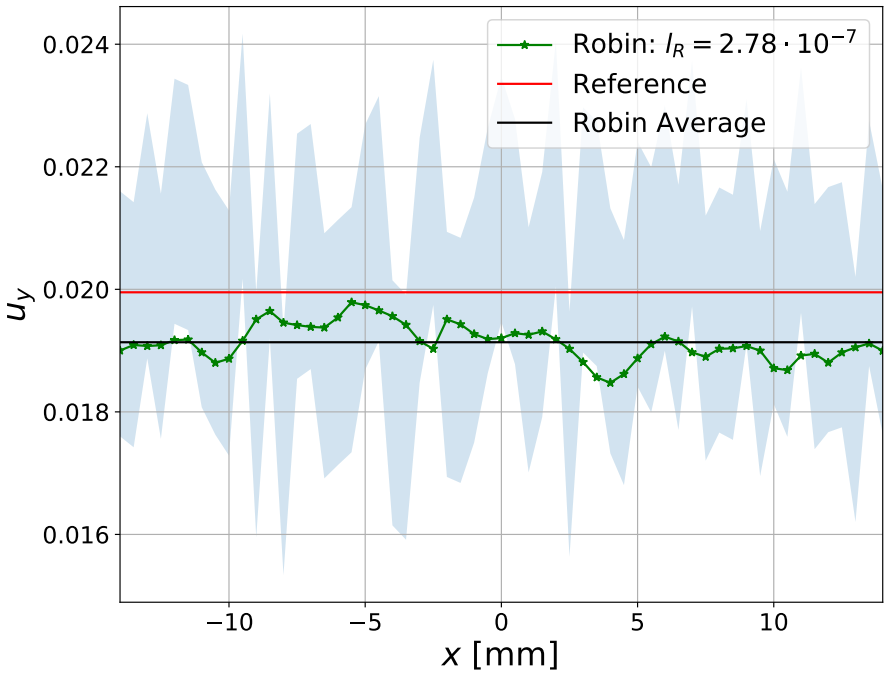

Figure 3.12: Solution on the boundary where displacement boundary conditions are prescribed. Robin solution (green) scattering band used to verify the discrepancy criterion. The scattering band corresponds to the prescribed noised displacement (u_b) $\pm k\varsigma$, with $k = 2$ and $\varsigma = 10^{-3}$. In this case 85% of the computed values are within the acceptable range. The amplitude is significantly reduced, but the average solution is altered with respect to the solution of the reference problem.

3.4 Discussion

Regarding the perforated flat specimen, the data reconstruction approaches provided a higher noise impact reduction compared to the mechanical filtering of the problem, or about 3 orders of magnitude within the elastic regime. Yet, in order to further evaluate the different filtering techniques, let us focus on a more complex example: a tensile test on a flat specimen inspired from the first Sandia Challenge [19], see figure 3.13. The difficulty with this case is that a portion of the specimen is hidden by the machine clamps during the test. This portion must thus be omitted from the finite element model of the specimen in order to be able to prescribe measured displacements as boundary conditions. The part of the geometry taken into account for this example is visible in figure 3.13. The choice of the geometry's cut is in general arbitrary. The present choice of the cut is made in order to be able to compute a value of the force reaction to be compared to the measured force.

3.4.1 Artificial boundary conditions

At first, artificial boundary conditions are used in order to define a reference simulation for the evaluation of the noise impact. A numerical simulation is carried out on the entire finite element model prescribing a constant displacement on the pins (4 mm/min). Afterwards, displacements

are extracted at the boundary coordinates of the finite element portion (the "submesh") to be used as reference boundary conditions. Then, noised boundary conditions are generated by adding a Gaussian noise to the reference boundary conditions. Such noise component has null mean value and standard deviation $\varsigma = 10^{-3}$ mm. Let us note that, in order to represent at best a DIC measurement, only surface displacements are extracted from the full simulation. An hypothesis of constance in depth is then made. In order to choose the parameters for the data reconstruction

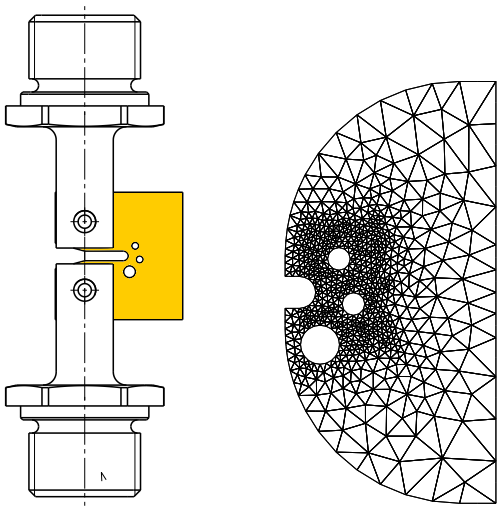

(a) (b)

Figure 3.13: Tensile test on a complex geometry specimen. Tensile test schema on the left and specimen mesh used for computation on the right.

techniques (polynomial order, window size) it is necessary to perform a prior analysis of the boundary conditions. In spite of the proximity of the edges with the geometrical singularities, the reference boundary conditions traced on the curvilinear axis (see figure 3.14) appears smooth enough to be reconstructed either by a single polynomial function or by a moving least squares technique. The choice of the polynomial order is here restricted to values larger than 2 since. It is clear from the curves in figure 3.14 that neither a 0 order polynomial nor a 1 order polynomial can reproduce the reference boundary conditions, since the real displacement profile barely corresponds to a low order polynomial. To prove it, the application of a low order polynomial (< 2) in the present case causes a distortion of the original problem, which may be still assessed in terms of alteration coefficient as visible in figure 3.15: there is a ratio of around 10 on the absolute alteration coefficient between orders 1 and 3. However, for an order 3 polynomial, high impact values can be observed at the extremes of the interval. It may signify that the boundary condition is not smooth enough to be captured by a low order polynomial function.

Consequently, the moving least square method may represent the better choice among the data reconstruction approaches. The considerations on this technique made for the perforated flat specimen are still valid: if window size is undersized, noise is reproduced and no filtering occurs. As visible in figure 3.16, the choice of a small window sizes ($w = 3$) produces negligible noise impact reductions regardless of the polynomial order, while a window size of $w = 27$ points produces a significant noise impact reduction.

In this case, the optimal Robin coefficient given by equation 3.23 is $l_R = 2.84 \times 10^{-7}$ mm/N for the top edge and $l_R = 2.48 \times 10^{-7}$ mm/N for the bottom one. These values lead to a satisfactory

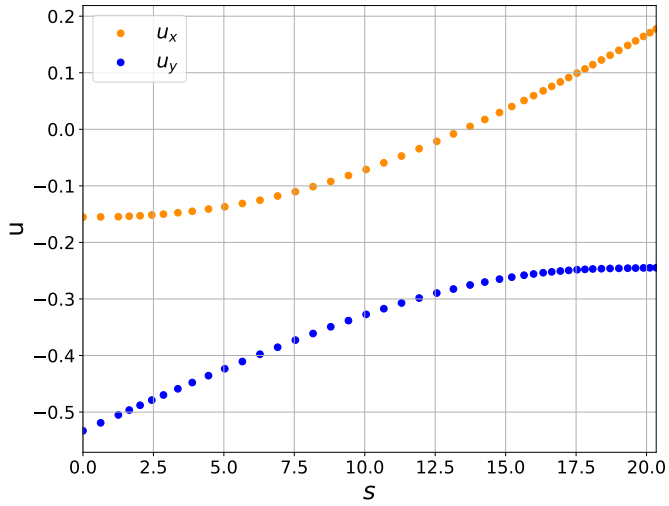

Figure 3.14: Displacement on the top boundary of the Sandia Challenge specimen. Notation s designates the curvilinear axis.

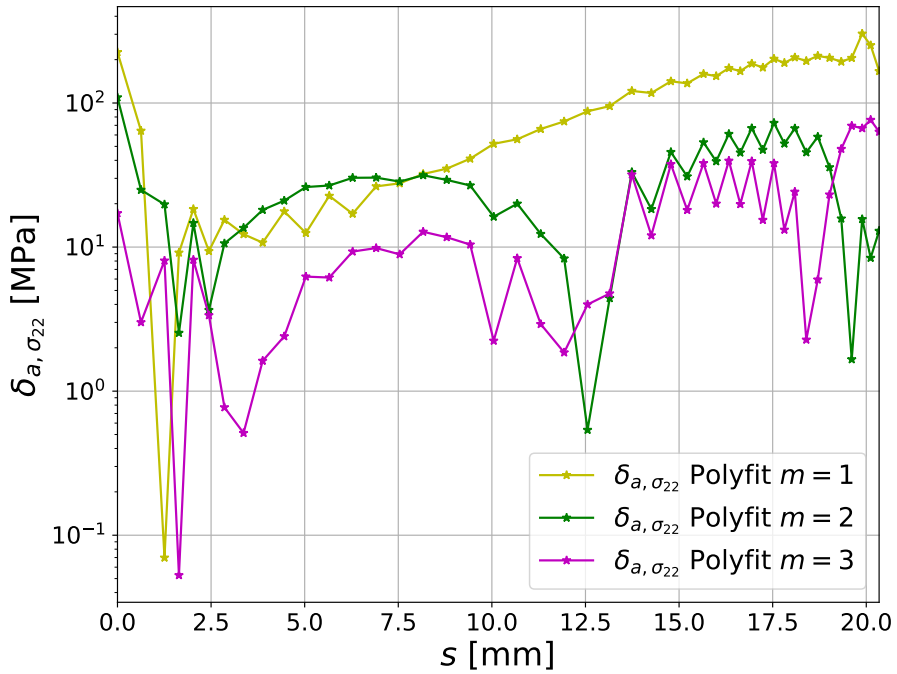

Figure 3.15: Absolute alteration coefficient $\delta_{a,\sigma_{22}}$ for different orders of the smoothing polynomial function. An inappropriate value of the polynomial order (2,3) produces a distortion of the original problem .

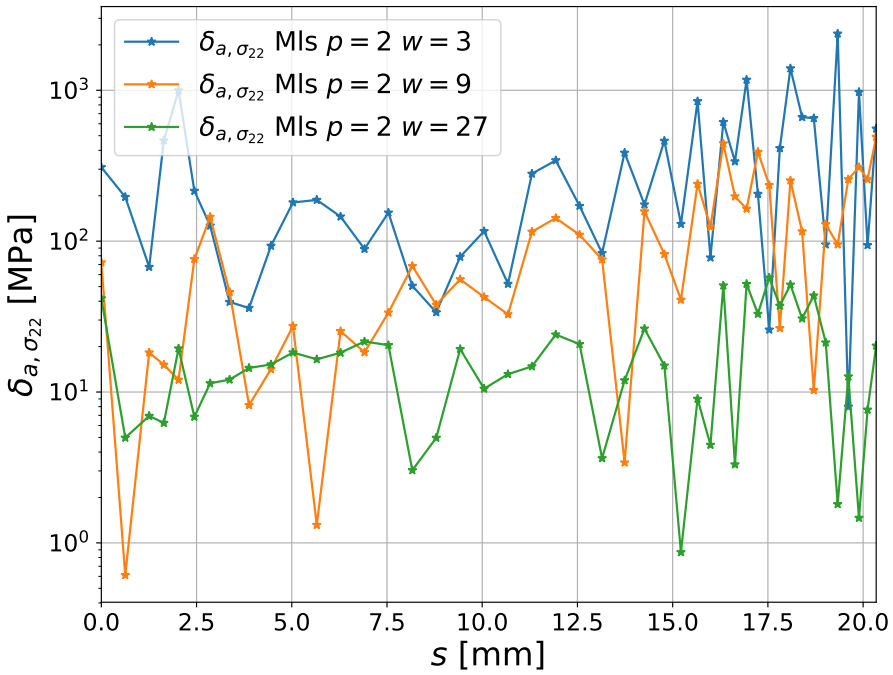

Figure 3.16: Alteration coefficient $\delta_{a,\sigma_{22}}$ for different parameters of the moving least squares algorithm.

reduction of the noise impact, as visible in figure 3.17 for the top edge. The discrepancy condition is indeed verified since $\left|\left|\underset{\sim}{u}_b - \underset{\sim}{u}_{l_R}\right|\right|_\Gamma \approx 1.1 \times 10^{-3}$ mm which respects the initial condition ($k\varsigma = 2 \times 10^{-3}$ mm). Furthermore, the solution is also locally acceptable since it is relatively close to the prescribed values, as visible in figure 3.18.

All the proposed filtering techniques provides a satisfactory reduction of noise impact. On the one hand, data reconstruction showed better scores than the mechanical filtering, but on the other hand, it requires a prior analysis of the boundary conditions to determine the optimal parameters, which may be non trivial. Instead, the mechanical filtering is an automated approach since it works regardless of the boundary condition profile.

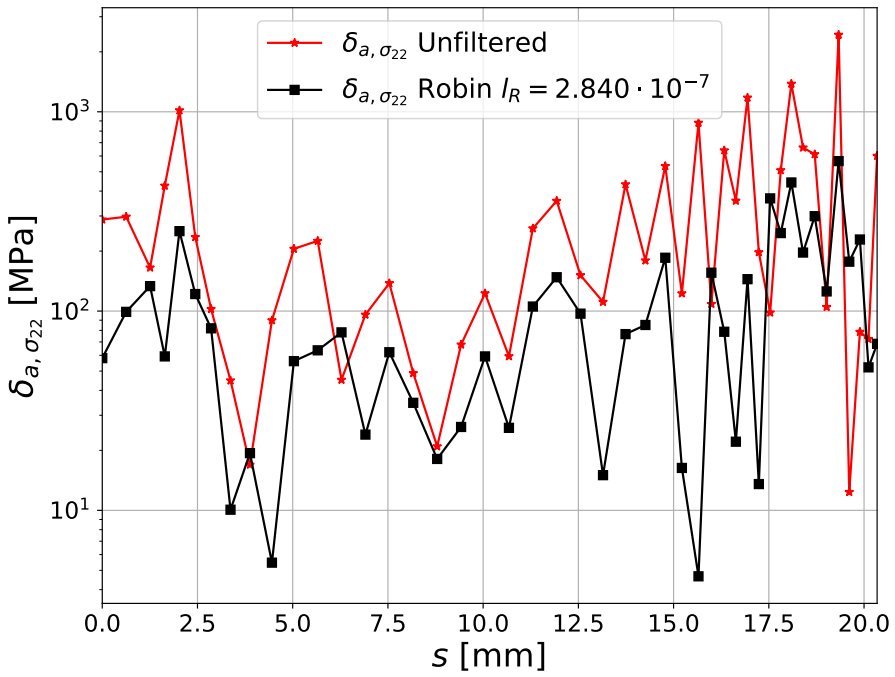

Figure 3.17: Alteration coefficient $\delta_{a,\sigma_{22}}$ for a Robin boundary condition with $l_R = 2.84 \times 10^{-7}$ mm/N.

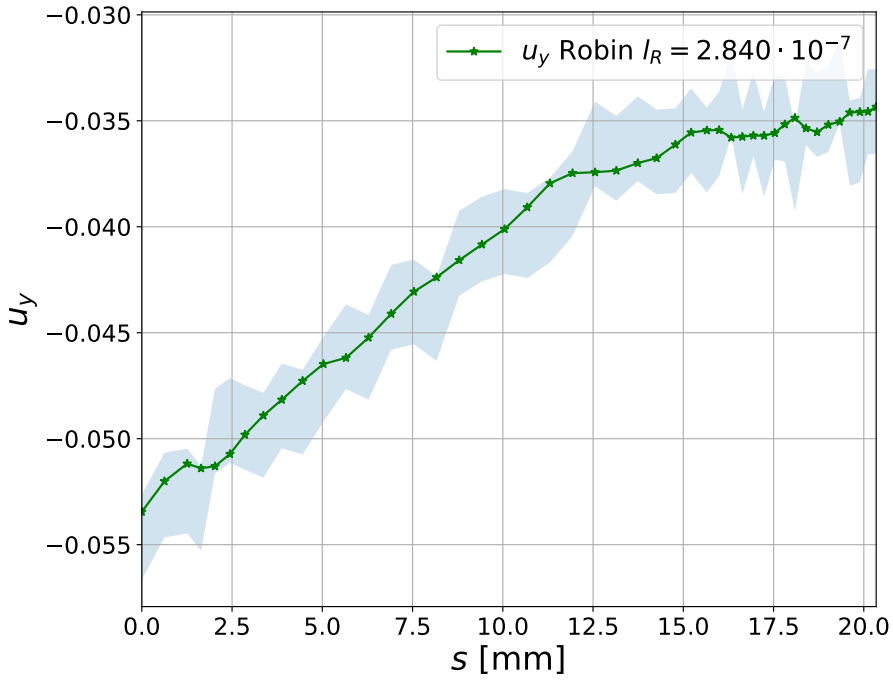

Figure 3.18: Displacement solution on the top edge. Robin boundary condition (blue line) and scattering band (blue) used to verify the discrepancy criterion. The scattering band corresponds to the prescribed noised displacement (u_b) $\pm k\varsigma$, with $k = 2$ and $\varsigma = 10^{-3}$. In this case 85% of the computed values are within the acceptable range.

3.4.2 Experimental boundary conditions

In order test the presented filtering techniques on experimental full-field measurements, a mechanical test has been carried out on the specimen inspired from the first Sandia Challenge. A constant uniform displacement (4 mm/min) is prescribed by the tensile test machine. A local DIC software developed at ONERA [28, 75] provides the full field surface measurement from which the boundary conditions for the "submesh" are extracted. The estimated DIC uncertainty for the considered specimen is $\varsigma = \pm 5 \times 10^{-4}$ mm. The polynomial reconstruction is carried out using a polynomial order $p = 3$, while the moving least squares technique using a polynomial order $p = 1$ with a window size $w = 27$. The optimal Robin coefficients are estimated at the first loading step using $k = 2$, which gives 3.298×10^{-7} mm/N and 4.756×10^{-7} mm/N for the top and bottom edges respectively. Let us note that using experimental boundary conditions a reference cannot be defined, so noise filtering may be evaluated this time based on the artificial cumulated plasticity that develops on the boundary of the mesh (which does not correspond to a free boundary in real life). As visible in figure 3.19, unfiltered boundary conditions leads to develop artificial cumulated plasticity on the boundary. Moreover, its value is similar to the value calculated around the specimen's holes. All the proposed filtering techniques allow to limit the development of cumulated plasticity on the boundary. The cumulated plasticity maxima are no longer located on the edges.

Furthermore, all the presented filtering techniques allow to perform numerical computation which is consistent with the experimental observations. Figure 3.20 shows that all the computed forces are consistent with the experimental one. Let us note that the rapid rise of the computed load is obtained close to the experimental failure initiation point. This is due to the fact that the plasticity model is unable to reproduce damage, which was excluded in this case from the computation, so that the computed displacement fields cannot reproduce the experimental ones (large mode I opening).

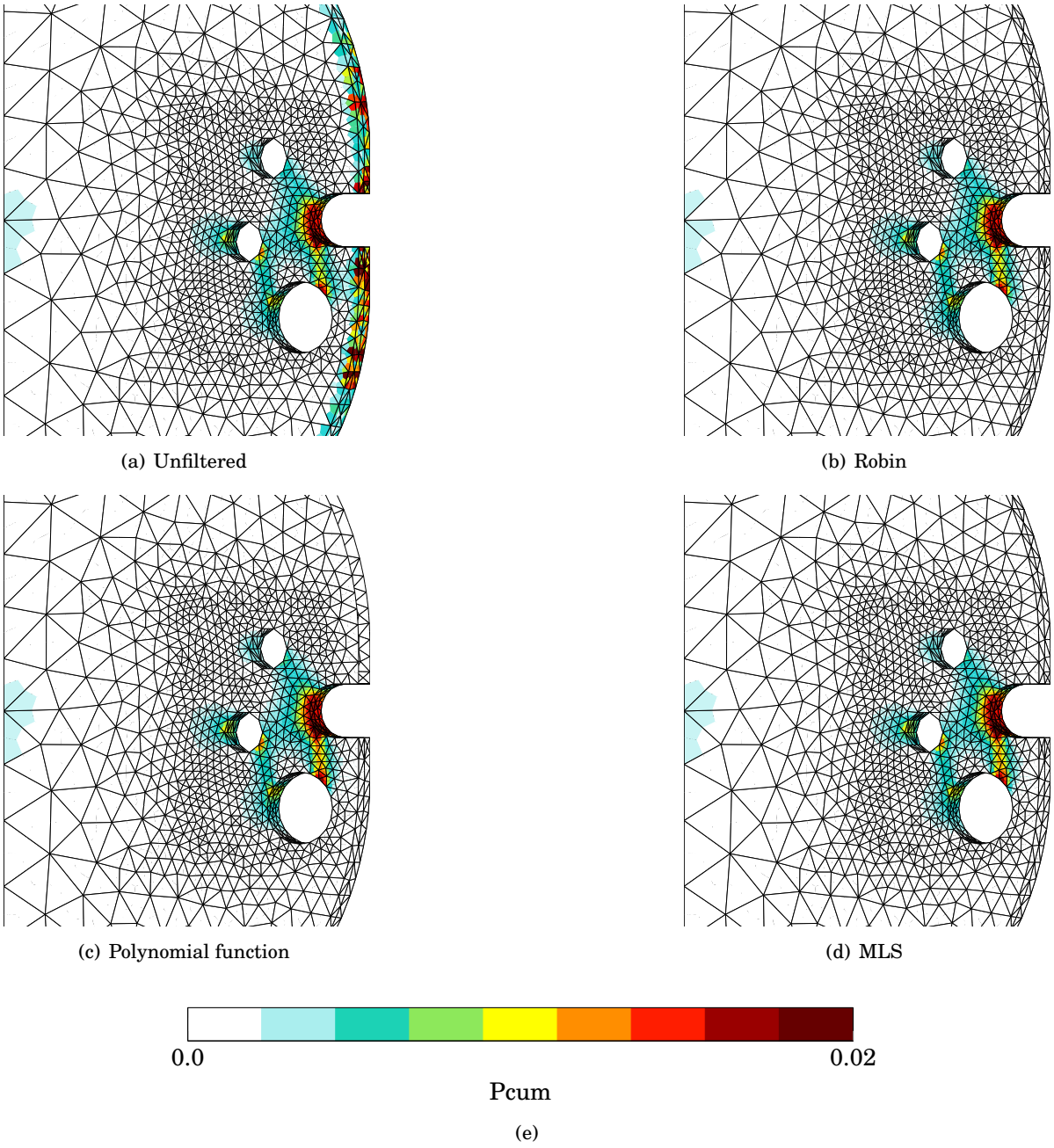

(a) Unfiltered

(b) Robin

(c) Polynomial function

(d) MLS

(e)

Figure 3.19: Cumulated plasticity on a portion of complex geometry for the three considered filtering techniques and the unfiltered simulation.

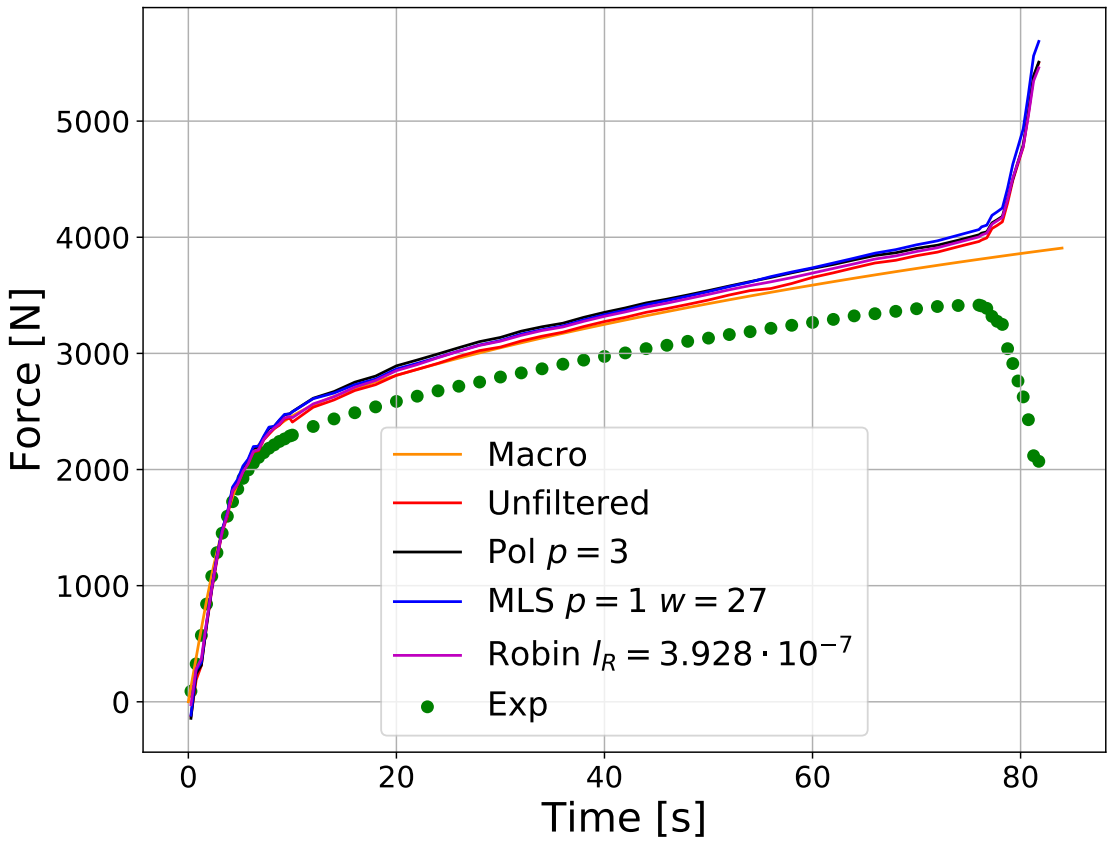

Figure 3.20: Measured force compared to the computed reaction. Notation *Macro* indicates the curve computed on the full geometry prescribing the same macroscopic displacement rate used for the experimental tests. Notation *Unfiltered* indicates the simulation where the measured boundary conditions have been directly prescribed as a Dirichlet boundary condition. Notations *MLS*, *Pol*, *Robin* indicate the filtering technique associated to the prescribed boundary conditions. For instance, moving least squares, polynomial function and Robin boundary condition.

3.5 Conclusion

The negative effects produced by noised boundary conditions prescribed to a mechanical problem have been studied. It has been shown that impact of noise is maximum around the edges where boundary conditions are prescribed and that impact is higher on the derived fields (*e.g.* strain) compared to the zero order fields (*e.g.* displacement). Three filtering solutions have been proposed and discussed based on an alteration coefficient defined on the difference with a reference (numerical) solution. The first two techniques aim at the reconstruction of the noised boundary condition (polynomial extrapolation and moving least squares reconstruction), while the latter one aims at the mechanical filtering of the problem thanks to a Robin boundary condition. All the different filtering techniques reduced the impact of noise. The data reconstruction techniques gave better results compared to the mechanical filtering. However, they require a prior analysis

of the data in order to set the function parameters (order of the polynomial, window size). Instead, the mechanical filtering by the Robin boundary condition turned out to be a robust technique based only on a filtering coefficient (here called the Robin coefficient l_R) which computation can be automated. However, the filtering capacity of this latter technique is constrained by the compromise made on l_R. In fact, a Robin boundary condition can be an approximation of a Dirichlet condition only for small values of l_R. The proposed filtering techniques have been applied to a problem where boundary conditions were issued of a Digital Image Correlation measurement on a tensile test: all of them were able to limit the development of artificial cumulated plasticity on the boundary, which may be responsible of wrong failure prediction otherwise.

Résumé

Ce troisième chapitre est un préambule à la méthode FEMU, et traite la prescription des déplacements mesurés comme condition au bord pour le calcul éléments finis. Cette opération assure la cohérence de la comparaison entre essai et calcul, qui est à la base de l'identification par recalage de modèles éléments finis. Parce que les valeurs mesurées sont polluées par l'incertitude de mesure (bruit), cette opération conduit à des altérations importantes de la solution mécanique.
Au travers d'un cas analytique il est prouvé que les effets négatifs du bruit de mesure sont plus importants pour les champs dérivés (par exemple les contraintes) et que cette altération est concentrée près des bords où les déplacements sont imposés. Dans le cas d'un calcul élasto-plastique, ce problème n'est pas négligeable car il conduit à générer de la plasticité artificielle qui pourrait induire une simulation incorrecte de la rupture. Le filtrage du bruit est donc fondamental. Différentes solutions de type filtre passe-bas sont possibles, comme par exemple des techniques de reconstruction (lissage) ou des techniques de régularisation mécanique. Ces différentes solutions ont été comparées. Les techniques s'appuyant sur le lissage montrent des atténuations importantes de l'impact du bruit, mais nécessitent une analyse préalable de la donnée afin de déterminer les paramètres de lissage. Ce type de solution est donc peu automatisable contrairement aux techniques basées sur la régularisation mécanique. Dans ce contexte, un filtrage mécanique innovant basé sur la condition au bord de Robin est proposé. Un seul coefficient est nécessaire pour ce type de filtrage et il s'obtient en suivant un protocole bien défini.

CHAPTER 4

FINITE ELEMENT MODEL UPDATING

This chapter describes the Finite Element Model Updating strategy considered to perform parameter identification from both the measured force and full-field measurements. It provides a description of the technique and a practical guidance for the identification of parameters. Section 4.1 introduces parameter identification as an inverse problem. Afterwards, section 4.2 focuses on parameters identification from full field measurements and motivates the choice of FEMU in the present study. Subsequently, section 4.3 describes the implemented FEMU technique, detailing the cost function used. Finally, section 4.4 presents and discusses the application of FEMU to the considered material for the identification of the plasticity parameters.

4.1 Parameter identification

Performing parameter identification basically means solving a so called inverse problem, in opposition with the classical forward problem of solid mechanics. A brief description of forward and inverse problems is provided in the following.

Forward problem A *forward problem* is a problem for which the input data and the model (also referred to as the system) together with its parameters are known. Both the material parameters and the geometry are considered as model parameters. The unknown of the forward problem is the response of the system. As an example, for a mechanical problem, given a solicitation, a mechanical model and a set of variables, the response of the forward problem consists in the deformed geometry and in the mechanical fields (stress, strain, displacement, etc.). In most of cases, a forward problem is *well-posed* according to Hadamard [59], *i.e.*:

- the solution exists (existence)
- the solution is unique (uniqueness)
- the solution is continuous with respect to the parameters of the system (stability)

The latter conditions ensures a low dependency of the solution on small errors on the input data or on the geometrical discretization.

Inverse problem An *inverse problem* is a problem for which the input data is known but the model is totally (or partially) unknown. To solve the inverse problem, it is necessary to know (totally or partially) the response of the system. In most cases, for a mechanical problem, the system is only partially unknown: the geometry and the material model are known, but the model parameters are not. The inverse problem can then be solved by knowing the response (force, displacement, strain, etc.) of the system. When only the parameters of the model are unknown, the inverse problem is referred to as an identification problem [51].

However, contrary to the forward problem, the inverse problem is in general ill-posed according to Hadamard. Because of the lack of completeness of the model (in general the model does not represent the whole set of complex phenomena that occurs during deformation) it is not possible to determine the exact solution of the inverse problem (inverting the forward problem). Therefore, the inverse problem is reformulated as an optimization (or minimization) problem[1], which stability is not ensured because of the uncertainties which affect the input data. However, the stability can be improved by considering superabundant data, as full-field measurements.

4.2 Parameter identification from full field measurements

There exists several techniques to perform parameter identification from full field measurements [51, 54]. In the following, four of the most commonly used methods are presented. One of them, FEMU, is retained.

4.2.1 Constitutive Equation Gap method (CEG)

This method aims at minimizing the discrepancy between an admissible stress field $\underset{\sim}{\tau}$ and a stress field $\underset{\sim}{\sigma}(\underline{u}_{exp})$ computed from the experimental displacement $\underline{u}_{exp}$ via the constitutive relation, $\sigma = \underset{\sim}{C}(\theta) : \underset{\sim}{\varepsilon}(\underline{u}_{exp})$, with $\underset{\sim}{C}(\underline{\theta})$ the elastic tensor dependent on the set of unknown parameters $\underline{\theta}$. The discrepancy is quantified thanks to an energy norm representing the constitutive equation gap:

$$\mathscr{E}(\underline{u}_{exp}, \underset{\sim}{\tau}, \underline{\theta}) = \frac{1}{2} \int_{\Omega} \left(\underset{\sim}{\tau} - \underset{\sim}{C}(\underline{\theta}) : \underset{\sim}{\varepsilon}(\underline{u}_{exp}) \right) : \underset{\sim}{C}(\underline{\theta})^{-1} : \left(\underset{\sim}{\tau} - \underset{\sim}{C}(\underline{\theta}) : \underset{\sim}{\varepsilon}(\underline{u}_{exp}) \right) \mathrm{d}\Omega \tag{4.1}$$

The constitutive equation gap of equation 4.1 has been first proposed as an error indicator for finite element simulations [73], and was considered only later as an identification tool. Is has been used to identify the parameters of elastic behaviours [17, 46] and an elasto-plastic behaviours [51] (considering a secant tensor). However, the majority of the applications concern elastic problems. Furthermore, let us note that, since DIC measurements are only available on the surface, the applications of the CEG method usually concerns problems for which the assumption of plane stress is valid.

4.2.2 The Virtual Fields Method (VFM)

This method, proposed by Grediac [53], is based on the principle of virtual work, which reads:

$$\int_{\Omega} \underset{\sim}{\sigma}(\theta, \underset{\sim}{\varepsilon}) : \underset{\sim}{\varepsilon}(\underline{u}^*) \mathrm{d}\Omega - \int_{\partial\Omega} \underline{T} \cdot \underline{u}^* \mathrm{d}S = 0 \tag{4.2}$$

[1] Such an approximative solution is also formalized as a quasi-solution in the sense of Tikhonov [127].

with $\underline{u}^*$ a kinematically admissible displacement field. The principle of virtual fields method is simple. It aims at verifying the equilibrium equation in a weak sense for a prescribed strain field. To do so, the stress tensor on the left term is evaluated from the constitutive law (explicitly for a linear elastic problem, implicitly for an incremental plastic problem) as function of the material parameters and of the experimental strain: $\underset{\sim}{\sigma} = f(\theta, \underset{\sim}{\varepsilon}_{exp})$. Hence, it is possible to build a system of equations where the unknowns are the n parameters to be identified. In order to be solved, the system must contain at least n linearly independent equations, which are obtained by carefully choosing the virtual displacement fields. This latter requirement represents the main difficulty with this method. Several works within the literature concern the choice (possibly automatic) of the virtual fields [52, 55, 129]. This Virtual Fields Method is a promising approach, since it allows the identification of dynamic properties by adding an acceleration term to the principle of virtual work. Furthermore, since there is no need to build an underling Finite Element model, the VFM does not require to know the exact boundary conditions. However, a particular attention to the experimental uncertainty is necessary, since the required quantities (strain and acceleration) are derivatives of the measured displacement: the derivation operation might amplify the uncertainty. Furthermore, as for the CEG methods, the majority of the applications within the literature concern situations for which the plane stress hypothesis is valid.

This method has been applied to identify, elastic [27] parameters, viscoelastic parameters [56], plastic parameters [8, 27], but also damage parameters [104] for ductile behaviour. Let us note that this latter reference considers a local Lemaitre damage model, where the damage law is based on 3 parameters.

4.2.3 The Equilibrium Gap Method (EGM)

This method aims at verifying the equilibrium relation in a local sense. Hence, it consists in minimizing the force residuals associated to a local mismatch of mechanical properties. The measured displacements $\underline{u}_{exp}$ are prescribed on each node of the mesh and the parameters $\underline{\theta}$ are updated until the force residual vector is null. It can be written in a weak form to be solved based on a finite element discretization [110]. As an example, for an elastic problem, whit $\underset{\sim}{K}$ the stiffness tensor, the cost function reads:

$$\underline{f}_{res} = \underset{\sim}{K}(\theta) \cdot \underline{u}_{exp} - \underline{f} \tag{4.3}$$

where vector $\underline{f}$ contains the applied nodal forces. This latter vector is null when only the interior nodes are considered. Like the virtual fields method, it requires the full-field displacement to be available over the entire surface of a 2D specimen.

This approach has been used to identify elastic properties [4], damage fields [30] and damage laws [34, 110] for composite materials. These latter applications concern local phenomenological descriptions of damage. An interesting comparison between FEMU, described here after, and the Virtual Fields Method can be found in [6].

4.2.4 The Finite Element Model Updating method (FEMU)

This method aims at minimizing the discrepancy between a measured quantity and its simulated counterpart by means of an optimization algorithm. The set of parameters which minimizes the discrepancy is the targeted set of material parameters. The discrepancy is quantified via a cost function considering either a single data type (displacement, force, temperature, ...) or several ones.

The principle of FEMU is intuitive. The corresponding flowchart is presented in figure 4.1. Each iteration includes the computation of a finite element solution and the evaluation of the cost function. Based on this latter evaluation the considered parameters are either kept and the identification stops, or updated to provide the input for the subsequent iteration. The presence of

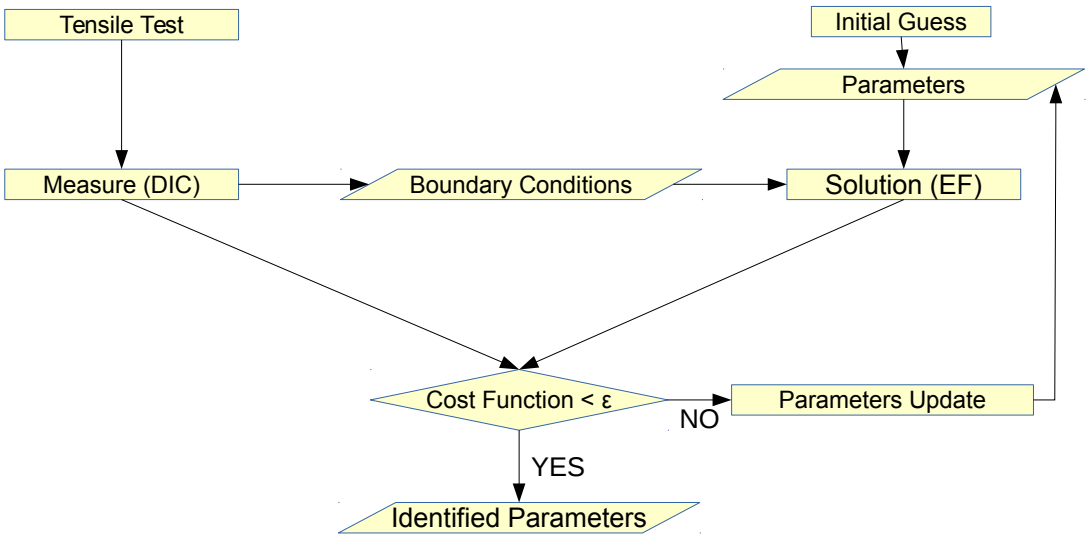

Figure 4.1: Flowchart for parameter identification by Finite Element Model Updating.

a finite element solution within the loop ensures that the equilibrium condition is automatically verified. Hence, for a given set of parameters, if the displacement solution exists, it is also kinematically admissible.

Historically, the first approaches of FEMU where based on a force cost function [33]. The displacement cost function arrived later [42] together with the full-field measurement techniques. Nowadays, it is quite common to use mixed cost functions. FEMU has been successfully used to identify elastic parameters [79, 121] and plastic parameters [37, 60, 93, 122]. Some works consider FEMU to perform identification of plastic parameters within the finite deformation framework [92, 109].

There exists a multitude of works within the literature, not labelled as FEMU, where the material parameters are identified by minimizing the discrepancy between the experimental response and the simulated one, as [37, 96]. Nevertheless, the boundary conditions are not always issued of a measurement system [124], and when they are the problems related to the measurement uncertainties described in chapter 3 is not taken into account. In other cases the cost function considers only macroscopic quantities (*i.e. not full-field measurements*) [123].

A FEMU technique has also been used to identify the parameters of local Gurson damage models [23, 90, 91, 123]. Despite the positive results, they are potentially dependent on the finite element mesh used for the simulations, and might not be used to simulate a specimen with different mesh size. Instead, in the present work, the FEMU approach is used to identify the parameters of a non local model, which solution is independent from the mesh size and orientation, as the identified parameters.

The motivations for the choice of the FEMU as identification approach can be summarized in the following points:

- the cost function can be formulated using observable data: force and displacement. In this way, the experimental uncertainties are not amplified by numerical derivation to obtain strain fields. Furthermore, the major advantage of using displacements rather than strains implies than any kind of strain formulation (corotational, multiplicative, logarithmic, ...) can be used in the FE calculations. A possible change of the finite element formulation is then neutral with respect to the identification procedure;
- the structure effects due to the large deformations are implicitly taken into account within the finite element solution;
- the FEMU approach does not require the measured displacement field to be available on the entire observed surface. Hence, correlation errors might be tolerated;
- it is possible to parametrize aspects of the model other than the behaviour's law parameters, as the regularization parameter of the non-local models;
- the implementation is flexible regarding the finite element (FE) solution. Indeed, since the FE model can be seen as a black box tool, the FEMU can be easily interfaced with different FE codes;
- the hypothesis of plane stress is not required.

An efficient identification procedure based on FEMU must consider consistent comparisons between experiments and simulations. To do so, measured displacements are prescribed as boundary conditions to the finite element problem. However, as illustrated in chapter 3, such an operation could lead to an erroneous solution if the measurement uncertainty is neglected. Regarding the management of the boundary conditions, the choice has been here to invest time to analyse the evolution of the boundary conditions in order to use the moving least squares reconstruction technique.

In this work, the in-plane boundary conditions are considered as constant along the thickness direction to compute 3D simulations. It can be considered an acceptable approximation as long as displacement is prescribed on boundaries relatively far from geometrical non-linearities. The out-of-plane boundary conditions are handled considering the symmetry of the specimen (only half of the specimen is modelled). Furthermore, beyond the problems related to the noised boundary conditions, the proposed FEMU implementation is sensitive to transfer of values from the DIC coordinate system to the FE coordinate system. Indeed, as discussed in appendix B, since the finite element mesh is built independently from the DIC results, it is necessary to ensure that the true coordinate systems are correctly aligned, in order not to add bias to the measured values.

Moreover, let us note that the main limitation of FEMU is related to the computational time, which might not be negligible when simulating complex behaviours as in the present case. Indeed, the computational time of one simulation determines the duration of the entire identification, which takes usually between 15 and 20 iterations to converge. The heaviest operation is here the computation of the Jacobian matrix used to update the parameters: it requires $m+1$ simulations with m the number of unknown parameters. For this reason, this operation has been parallelized, so that the computation of the Jacobian costs (in terms of time) as a single computation. Nevertheless, the duration of identification remains considerable.

4.3 Cost function

The cost function is the core of the identification algorithm. It is, in general, defined as *p-norm* of the discrepancy between the experimental and the numerical response, which is referred to as the identification residual. Hence, the cost function is a scalar function $\psi : \mathbb{R}^m \to \mathbb{R}$ where m is the number of time steps considered. Explicitly:

$$\psi = \left|\left|\underline{r}(\underline{\theta})\right|\right|_p = \left(\sum_{i=1}^{m} |r_i(\underline{\theta})|^p\right)^{\frac{1}{p}} \tag{4.4}$$

where $\underline{\theta}$ is the vector of the unknown parameters. Several authors agree with the choice of an Euclidean norm ($p = 2$) [37, 68, 70, 79, 92, 109], since it leads to a differentiable cost function, and the minimization problem is generally formulated as a least squares minimization problem. An absolute norm ($p = 1$) could be used as well [25]. The Euclidean norm is considered in the present work.

The proposed norm defines a mixed cost function, combining both the force residual and the displacement residual by means of a scalar coefficient $\alpha \in [0, 1]$:

$$\psi = \alpha\psi_d + (1 - \alpha)\psi_f \tag{4.5}$$

The residuals are chosen to be adimensional quantities because of their different nature:

$$\psi_d = \frac{f(u^{sim}(\underline{\theta}) - u^{exp})}{W_d} \qquad \psi_f = \frac{f(F^{sim}(\underline{\theta}) - F^{exp})}{W_f} \tag{4.6}$$

where notations sim and exp are used to refer to simulated and experimental quantities respectively, while W_f and W_d are the normalization coefficients for displacement and force respectively. The choice of these latter coefficients is not straightforward since they must lead to residuals of the same order of magnitude in order to manage the weight of the displacement term and the force term only through the parameter α. Several examples of normalizations might be found within the literature. Among them:

- Pottier [109] normalizes each term of both residuals (force and displacement) by the maximum value measured at the considered step;
- Manhken [92] normalizes the displacement residual by the initial residual (the discrepancy between the experimental displacement and the displacement computed using the initial guess parameters);
- Kajberg [67] normalizes both residuals by the amplitude of the considered quantity;
- Robert [115] normalizes the force residual by the maximum value at the considered step, as Pottier [109], while the displacement residual by the standard deviation of the measured displacement.

In the present work an approach similar to Robert et al. [115] is considered: both the displacement normalization coefficient and the force normalization coefficient are calculated using the standard deviation definition[2]. After implementation, this proposition seems to lead to adimensional values of the same order of magnitude both for the displacement residual and the force residual.

[2]No statistical meaning should be attributed to the force normalization factor although it is computed as a standard deviation.

The considered cost function aims at minimizing the average Euclidean distance between the calculated and measured quantities. The average value is meant both in a spatial and in a temporal sense. The displacement and force residuals read:

$$\psi_d = \frac{\sqrt{\dfrac{1}{t_e - t_s}\displaystyle\int_{t_s}^{t_e}\left[\frac{1}{\Omega}\iint_{\Omega}\sum_{i=1}^{N_{dim}}\left(u_i^{exp} - u_i^{sim}(\underline{\theta})\right)^2 \mathrm{d}\Omega\right]\mathrm{d}t}}{\sqrt{\dfrac{1}{t_e - t_s}\displaystyle\int_{t_s}^{t_e}\left[\frac{1}{\Omega}\iint_{\Omega}\sum_{i=1}^{N_{dim}}\left(u_i^{exp}\right)^2 \mathrm{d}\Omega\right]\mathrm{d}t - \left\{\dfrac{1}{t_e - t_s}\displaystyle\int_{t_s}^{t_e}\left[\frac{1}{\Omega}\iint_{\Omega}\sqrt{\sum_{i=1}^{N_{dim}}\left(u_i^{exp}\right)}\,\mathrm{d}\Omega\right]\mathrm{d}t\right\}^2}} \tag{4.7}$$

$$\psi_f = \frac{\sqrt{\dfrac{1}{t_e - t_s}\displaystyle\int_{t_s}^{t_e}\sum_{i=1}^{N_{dim}}\left(F_i^{exp} - F_i^{sim}(\underline{\theta})\right)^2 \mathrm{d}t}}{\sqrt{\dfrac{1}{t_e - t_s}\displaystyle\int_{t_s}^{t_e}\sum_{i=1}^{N_{dim}}\left(F_i^{exp}\right)^2 \mathrm{d}t - \left\{\dfrac{1}{t_e - t_s}\displaystyle\int_{t_s}^{t_e}\sqrt{\sum_{i=1}^{N_{dim}}\left(F_i^{exp}\right)}\,\mathrm{d}t\right\}^2}} \tag{4.8}$$

where it is possible to recognize the discrepancy terms at the numerators and the standard deviations at the denominators. In the expressions of the residuals:

- notation Ω indicates the area considered for the minimization of the displacement cost function. The choice of such a parameter should be done based on sensitivity analysis, as shown in appendix E, in order to exclude those zones which are insensitive from a variation of the parameters since solely the measurement uncertainty would contribute to the cost function
- notations t_s and t_e indicates respectively the initial and final time instants to consider for the identification. As for the minimization area Ω, the time interval should be chosen based on a sensitivity analysis
- notation N_{dim} indicates the displacement components to take into account within the cost function. A major guidance for the choice of this parameter is provided by the sensitivity analysis. However, the choice depends also on the measurement equipment, so that the coefficient might be different between displacement and force residual, as in the present case. Indeed, the load cell of the tensile test machine provides the force along a single direction, while the stero-DIC system provides the displacements along 3 directions.

Furthermore, let us note that the choice of an integral formulation for the spatial average was made in order to obtain a cost function value independent from the number of nodes of the finite element mesh, which might change because of a mesh adaptation operation. Similarly, the integral formulation for the temporal average is introduced to be independent from the sampling frequency of the images which might not be constant during the different stages of loading (elasticity, plasticity, ...).

Finally, in order to take into account the experimental scattering, the parameters should be identified on several tests at the same time. To do so, a unique cost function constituted by the

sum of the individual contributions is considered:

$$\psi = \sum_{n=1}^{N_{test}} \left(\alpha_n \psi_{d,n} + (1-\alpha_n)\psi_{f,n} \right) \tag{4.9}$$

4.4 Identification of parameters within the plastic regime

This section illustrates the identification of the plasticity parameters, which is carried out considering the largest number of experimental tests as possible in order to take into account the scattering of the data. The approach is focused at first on the hardening parameters, and then on the Hosford exponent. Moreover, the identification considered solely the part of the experimental response within the plastic regime, which is a condition verified up to a strain value of about 40% (*i.e.* without damage), as shown in section 1.4.

The FEMU identification is supported by the sensitivity analysis illustrated in appendix E. The identification is assumed, in this study, to be efficient solely if a perturbation of the parameters induces a variation of the response (force, displacement) which is at least comparable with the uncertainty of the measurement instrument. Indeed, since the cost function is minimized by means of a gradient method, which evaluates the minimization direction based on a Jacobian matrix computed by perturbation of the parameters, a variation of the response within the range of uncertainty of the measure might lead to local minima of the cost function.

4.4.1 Identification of the hardening parameters

This identification is carried out using both the classical approach for identification and the FEMU approach, in order to validate this latter by means of a comparison with a commonly accepted approach. To start, let us recall the hardening law from chapter 2:

$$R(p) = R_0 + Q_1(1 - e^{-b_1 p}) + Q_2(1 - e^{-b_2 p}) \tag{4.10}$$

where R_0, the yield stress, together with the hardening coefficients Q_1, b_1, Q_2 and b_2, are referred to as the hardening parameters to be identified.

Classical approach The most straightforward procedure for the identification of the hardening parameters, referred to as the classical approach, consists in fitting the experimental stress versus strain curves. Such a technique, based on punctual measurements (extensometer), relies on the hypothesis of homogeneous deformation within the gauge length, which is sufficiently satisfied considering smooth specimens. The classical approach is also based on the hypothesis of mass (volume) conservation (valid within the plastic regime only) which allows to determine the relation between the true quantities of the hardening law (σ, ε) and nominal quantities issued from the experimental tests (σ_n, ε_n), as described in chapter 1, equation 1.4. Therefore, the classical identification was carried out considering two tests on smooth specimens that were equipped with an extensometer: tests CSMOOTH-3 and CSMOOTH-4 (see table 1.2).

FEMU approach Contrary to the classical approach, the FEMU approach can be applied to any geometry. The following 10 tests have been considered to identify the hardening parameters via FEMU: CAE10-(1,2) CAE4-(1,2) CAE2-(1,2) PAE1-(1,2) and PAE2-1. The smooth specimens were excluded since the lack of remarkable features (corners or artificial markers) on their

surface does not allow a correct alignment of the coordinate systems according to the procedure described in appendix B. The first step to set up the FEMU identification is to analyse the results of the sensitivity analysis according to the criterion mentioned in the introduction of this section. It is shown that the influence of the hardening parameters on the displacement fields is located on the same area, which would imply an indetermination of the parameters if solely the displacement discrepancy were considered. Indeed, it would not be possible to distinguish the individual contribution of each parameter. Furthermore, the influence of parameters Q_1 and b_1 on displacement is negligible (compared to the measurement uncertainty) both at the early and late stages of hardening. For these reasons, the repartition coefficient α was set to $\alpha = 0$ in order to minimize the force discrepancy only. Solely the vertical component of the simulated load is considered, since it is the unique component comparable with an experimental quantity.

Let us note that there is a slight difference between the FEMU identification and the classical one: the Hosford exponent identification. Indeed, the influence of this parameter is null for smooth specimens but not for notched specimens, because of the multi-axial state of stress. For this reason, the Hosford exponent should, *a priori*, be considered within the FEMU identification at the same time than the hardening parameters. However, since the sensitivity analysis showed that the influence of such a parameter on the force discrepancy is here negligible (*i.e.* with $\alpha = 0$), it has not been considered for this first step of identification.

The FEMU algorithm has been tested considering different guess values, in order to assess the uniqueness of the solution. The results and their relative initial values are reported in table 4.1: All the techniques converge to a similar set of values. However, the values of parameters Q_1 and

Guess values				
Parameter	Classical	FEMU 1	FEMU 2	Unit
R_0	490	490	350	MPa
Q_1	80	80	50	MPa
b_1	230	230	300	
Q_2	3600	3600	2000	MPa
b_2	0.6	0.6	0.7	

Results				
Parameter	Classical	FEMU 1	FEMU 2	Unit
R_0	460	454 (−1.3%)	448 (−2.6%)	MPa
Q_1	62	71 (+14.5%)	78 (+26%)	MPa
b_1	315	408 (+29.5%)	397 (+26.%)	
Q_2	2820	2944 (+4.4%)	2905 (−3.%)	MPa
b_2	0.794	0.802 (+1%)	0.833 (+5%)	

Table 4.1: Hardening parameters: guess values and identification results. The set of parameters obtained via classical identification is similar to the set of parameters obtained using FEMU. The difference with the parameters obtained by the classical approach is expressed in percentage next to each values.

b_1 identified using FEMU have a higher difference with respect to the the values identified using the classical technique. This large difference is attributed to the relatively low influence of those parameters on the global response, which is limited at the early stages of hardening, as visible in figure 4.2.

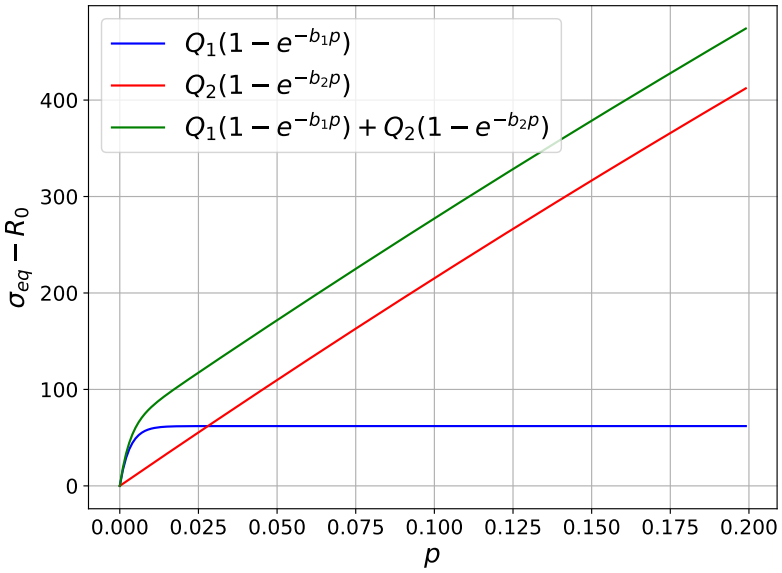

Figure 4.2: Evolution of the non-linear terms of the hardening law with respect to the cumulated plasticity p, considering the parameters identified by the classical approach. The influence of parameters Q_1 and b_1 is limited at the early stages of hardening, and produces a simple vertical shift at the late stages of hardening.

4.4.2 Verification of the hardening parameters

The identified hardening parameters were verified by means of comparisons with the experimental data, in two steps. The first comparison was made based on the experimental responses of the axisymmetric smooth specimens, which were excluded from the FEMU identification. As visible in figure 4.3, the set of parameters issued from the classical identification leads to a numerical curve which lies perfectly in between the two experimental ones. This confirms the validity of the curve fitting performed. The parameters identified via FEMU leads to slightly overestimating the response of the axisymmetric specimens. Let us recall that the FEMU identification considered 9 tests compared to the 2 tests considered for the classical identification. Further analysis of the response on the other geometries are thus necessary to conclude on this difference. In the meantime, let us note that the two curves considering the FEMU parameters are close to each other, confirming the stability of the result. The set of parameters referred to as FEMU 1 is then arbitrarily chosen as the set of identified hardening parameters.

Further verification of the hardening parameters was made by comparison between experiment and simulation for all the tests on simple notched specimens carried out in this work, as visible in figures 4.4, 4.5, 4.6 and 4.7 for axisymmetric, PAE1, PAE2 and plain strain geometries respectively. The comparison with the experimental curves is satisfactory for both sets of parameters (classical and FEMU 1 in table 4.1), confirming the validity of FEMU for the identification of the hardening parameters. However, let us note that the computational time of these two types of identification is not comparable, which motivates the choice of the classical approach if a large number of tests on smooth specimens is available.

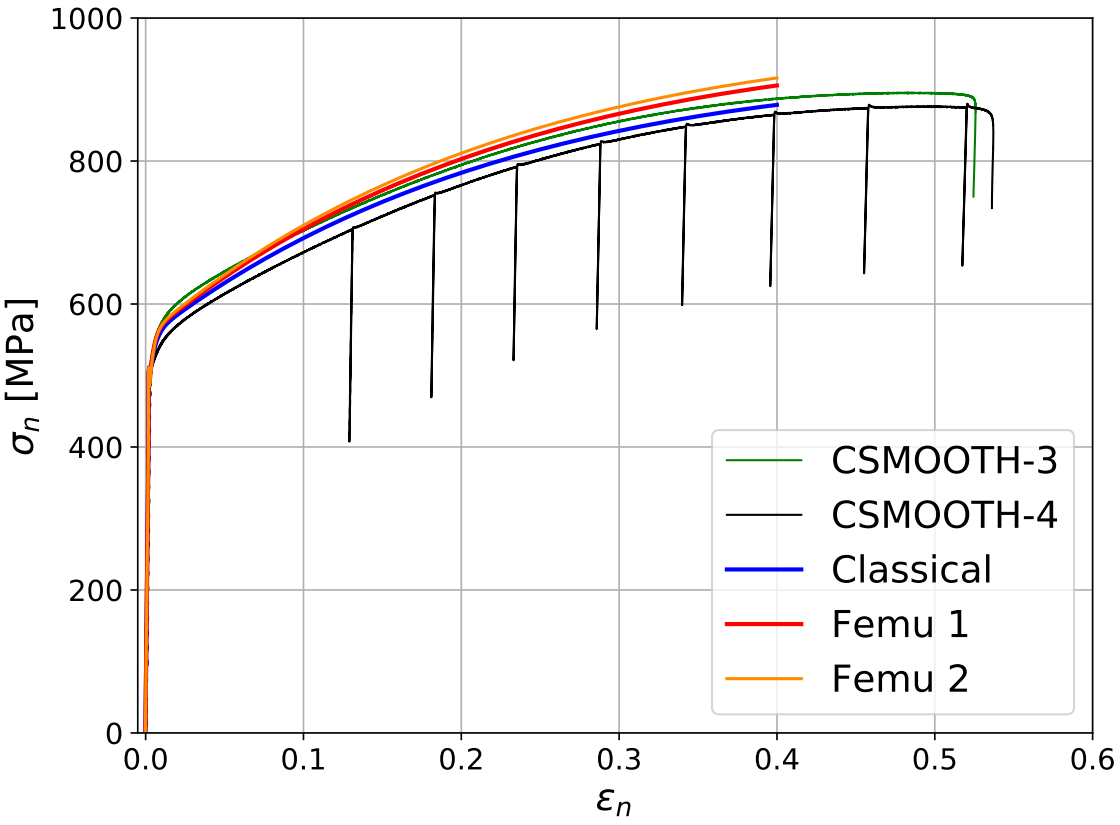

Figure 4.3: Comparison between the identified set of parameters based on the experimental response of the axisymmetric smooth specimens. The numerical curves are calculated up to a strain level of 40%, which delimits the plastic regime.

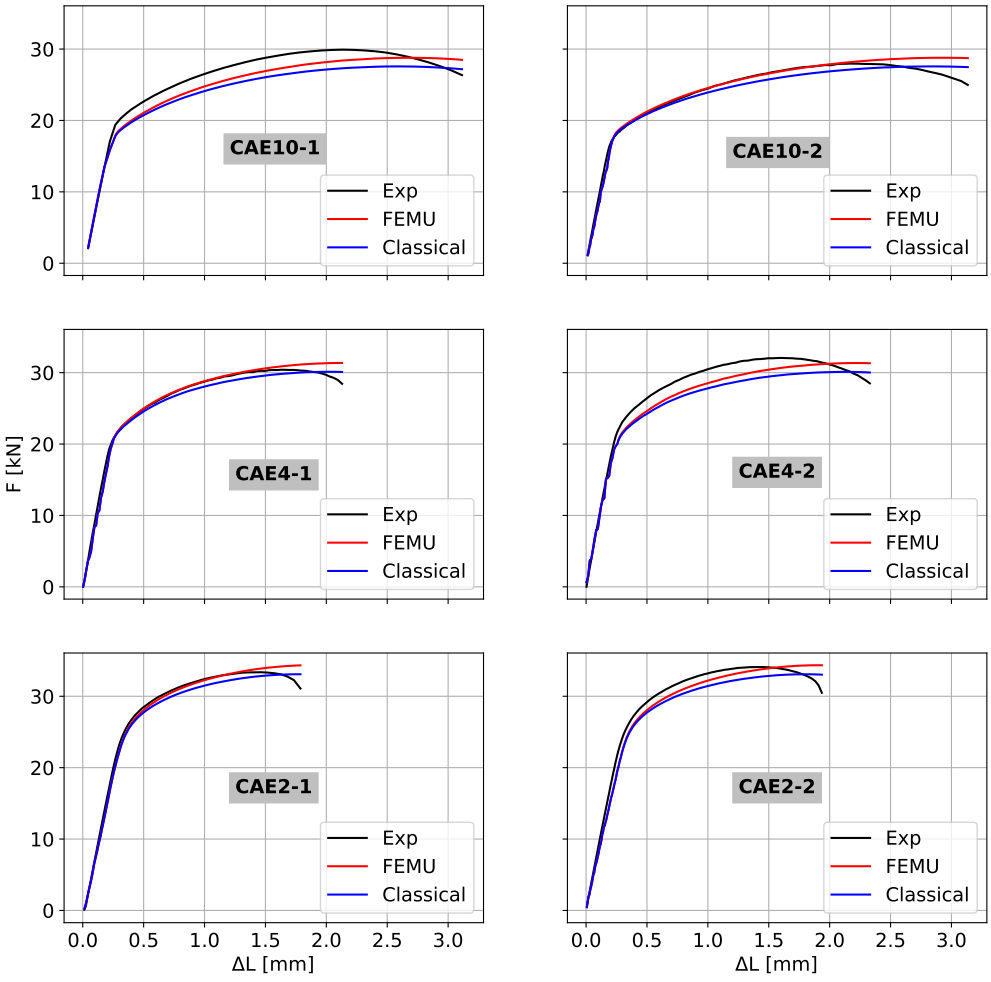

Figure 4.4: Comparison between the experimental responses and their numerical counterparts for the axisymmetric specimens. The simulations are computed using the respective measured boundary conditions and the identified set of parameters referred to as FEMU 1. The Hosford exponent was set to $n = 7.5$.

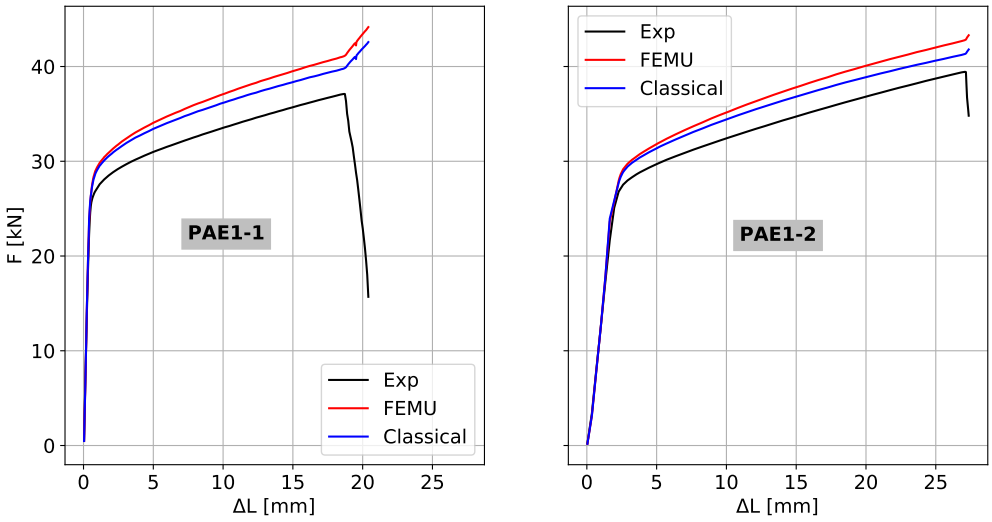

Figure 4.5: Comparison between the experimental responses and their numerical counterparts for the flat PAE1 specimens. The simulations are computed using the respective measured boundary conditions and the identified set of parameters referred to as FEMU 1. The Hosford exponent was set to $n = 7.5$.

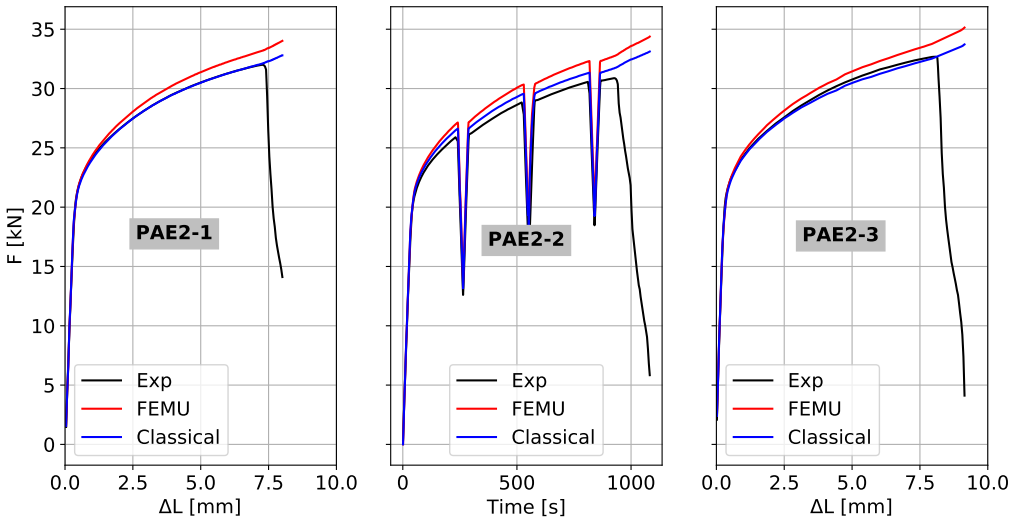

Figure 4.6: Comparison between the experimental responses and their numerical counterparts for the flat specimens. The simulations are computed using the respective measured boundary conditions and the identified set of parameters referred to as FEMU 1. The Hosford exponent was set to $n = 7.5$. The load of specimen PAE2-2 has been plotted versus time rather than elongation in order to assess the accuracy of the management of the boundary conditions: the elastic unloads (0.2 mm) are correctly reproduced. Specimens PAE2-2 and PAE2-3 were not considered for the identification.

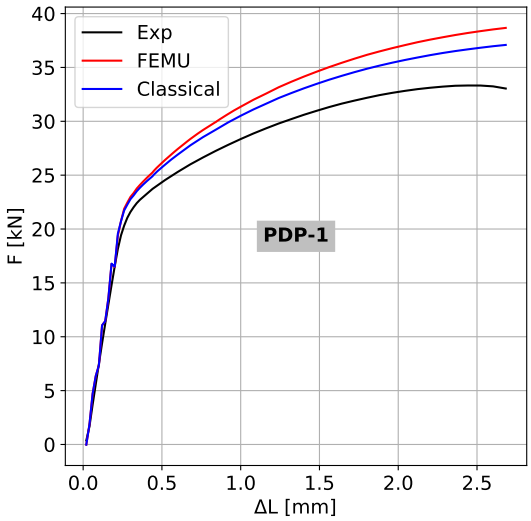

Figure 4.7: Comparison between the experimental responses and their numerical counterparts for the plane strain specimen. The simulations are computed using the respective measured boundary conditions and the identified set of parameters referred to as FEMU 1. The Hosford exponent was set to $n = 7.5$.

From the analysis of the macroscopic responses, it appears that the load of flat specimens is overestimated compared to the experiment, contrary to the axisymmetric specimens. Such a mismatch is attributed to the material scattering, due to a possible inhomogeneity of the the raw material. The stress versus strain curves of figure 4.8 illustrate the significant material scattering on smooth specimens. However, a link with the microstructure has not been investigated.

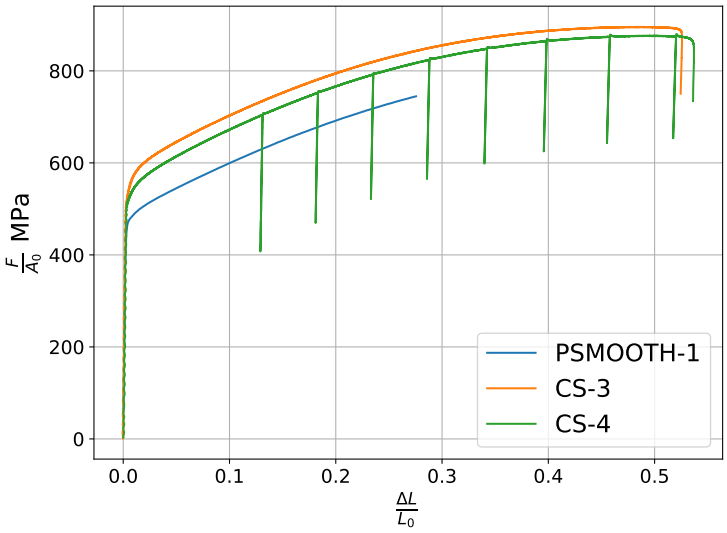

Figure 4.8: Experimental load for 3 different geometries. There is a considerable scattering due to a possible inhomogeneity of the the raw material.

4.4.3 Identification of the Hosford exponent

As mentioned, the Hosford exponent was not included within the previous FEMU identification since the repartition coefficient α was set to a null value (force gap only) and the sensitivity analysis showed a negligible influence of this parameter on the force response for the considered geometries. Therefore, the identification of this parameters was carried out in a second time.

According to the sensitivity analysis in appendix E, the Hosford exponent has a significant influence on the horizontal displacement (orthogonal to the loading direction) especially for the flat specimens PAE1 and PAE2. Therefore, the FEMU identification has been carried out by setting the repartition coefficient to unit $\alpha = 1.0$ and considering solely the horizontal direction within the minimization. To limit the computational time, solely the test PAE2-1 was considered for this step of the identification. Again, in order to verify the uniqueness of the solution, several guess values have been tested (see table 4.2). The final values are similar to each other so that an Hosford exponent $n = 7.5$ is retained as the identified value.

An additional confirmation of the validity of this result is given by the evolution of the cost function with respect to the targeted parameter n visible in figure 4.9, from which the convexity of the cost function is clear.

	Hosford exponent n		
Guess Value	4	10	6
Final Value	7.3	7.9	7.6

Table 4.2: Hosford exponent: guess values and identification results.

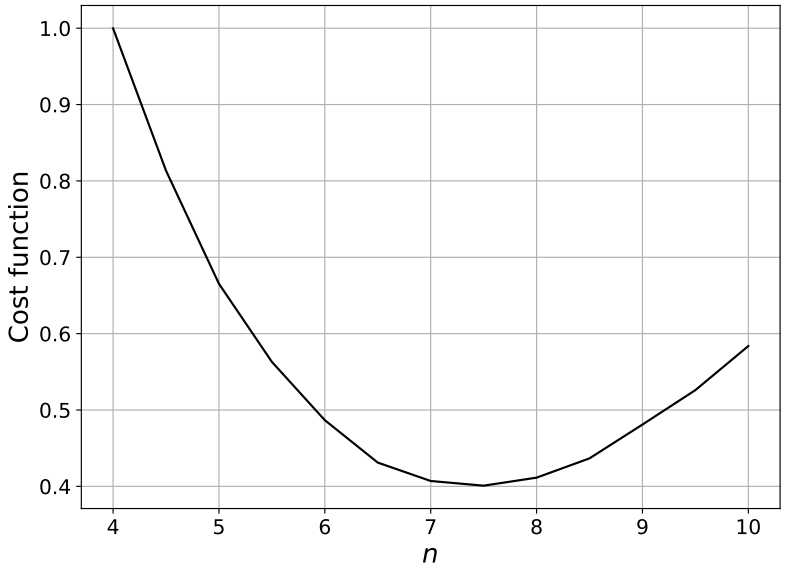

Figure 4.9: Convexity of the cost function with respect to the Hosford exponent. Let us not the high convexity of this parameter given by the considerable sensitivity of the transversal displacement field with respect to the Hosford exponent.

4.5 Conclusion

The proposed strategy for parameter identification has been successfully validated thanks to the identification of the hardening parameters. Indeed, the obtained parameters are similar to the parameters identified using a classical approach. A different behaviour was observed between flat and axisymmetric specimens, which has been attributed to an intrinsic difference of the material at the raw state. Finally, the Hosford exponent has been identified using FEMU, thanks to its considerable influence of the transversal displacement field.

Résumé

Ce quatrième chapitre introduit l'identification des paramètres à partir de mesures de champ denses. Les principales méthodes présentes dans la littérature sont décrites, dont la méthode FEMU retenue pour cette étude. La FEMU est choisie car elle s'appuie sur des quantités directement mesurables et car elle permet de traiter des problèmes nécessitant une simulation tridimensionnelle. La formulation de la FEMU proposée est basée sur une fonction coût de type intégral afin de rendre la mesure de l'écart entre simulation et expérience indépendante du maillage éléments finis. De plus, la fonction coût proposée prend en compte force et déplacement simultanément, ce qui nécessite une normalisation adéquate afin de comparer ces quantités de nature différente. La normalisation est faite en considérant les écarts types respectifs des mesures. La mise en place de l'identification demande le réglage d'un nombre de facteurs à prendre en compte tels que la zone d'intérêt ou bien les composantes de déplacement. Ce réglage est guidé par des analyses de sensibilité. Ces analyses montrent si les paramètres ont une influence suffisante pour l'identification par rapport à la précision des moyens de mesure. Elles montrent également si les paramètres sont en compétition dans la zone considérée. Le paramètres d'écrouissage de l'Inconel625 sont d'abord identifiés par une approche standard et ensuite par FEMU sur des géométries différentes. La similitude entre les résultats issus de ces deux approches, en termes de valeur et de réponse macroscopique, permet de valider l'approche FEMU. Enfin, la FEMU est utilisée pour identifier le critère de plasticité d'Hosford à partir d'un seul essai de traction sur éprouvette plane entaillée.

CHAPTER 5

IDENTIFICATION OF DAMAGE PARAMETERS VIA FEMU

This last chapter of the thesis is dedicated to the FEMU identification of the damage parameters (both the parameters of the GTN model and the regularization parameter of the non-local model being here referred to as damage parameters). Section 5.1 gives a brief literature overview of different approaches for the identification of the GTN model. Subsequently, section 5.2 discusses the influence of the regularization parameter for the considered model. Section 5.3 illustrates the application of FEMU on a flat specimen and section 5.4 discusses the obtained results by means of comparisons between experiment and simulation on several specimens.

5.1 Identification of the GTN model within the literature

There is not a unique approach to perform the identification of the GTN parameters. Various approaches have been proposed so far, most of which consider a mixed experimental-numerical technique with, possibly, SEM observations [71, 84]. The main purpose of SEM analysis is to determine the parameters which have a micro-mechanical meaning, as the initial void volume fraction or the final void volume fraction [71]. In this way, it is possible to reduce the number of parameters to be identified by means of an optimization algorithm, which are managed as phenomenological parameters. Reducing the number of parameters to be optimized is indeed as a key point of parameter identification. With the same objective, several studies aim at determining correlations between the parameters. Perrin et al [108], define parameter q_1 as function of porosity, showing that, for a null porosity, this parameter tends to $q_1 = 1.47$, accordingly to the result of Tvergaard and Needleman [131] ($q_1 = 1.5$). Gao et al. [48] link parameters q_1 and q_2 to the strain hardening, which has a decelerating effect on void growth. Zhang et al.[138] propose a relation between f_r and f_0 ($f_r = 0.15 + 2f_0$). Benseddiq et al. [13] show that the critical void volume fraction f_c decreases with increasing stress triaxiality for a nickel-chromium steel (12NC6). However, the results are based on a limited number of tests. Let us note that an exhaustive overview of various identification approaches and their respective results can be found in the latter mentioned work of Benseddiq et al.

Because of the similarity with the proposed FEMU approach, it is worth mentioning the works of Springmann and Kuna [123, 124], where it is proposed to identify the GTN model

by minimizing the distance (force and local displacement) between test and simulation by means of a gradient method. However, their approach considers a local model of damage, giving parameters potentially dependent on the considered mesh. Furthermore, the boundary conditions are apparently not issued from local measurements, since only 1/8 of the specimen geometry is modelled. Brunet et al. [24] consider a non-local model of damage and propose to identify the damage parameters with a FEMU approach based on the force gap. The differences with the present approach are that the non-local regularization is an explicit gradient formulation and that the FE solution is obtained according to an explicit integration. Most of all, the boundary conditions for the finite element problem do not appear as issued from full-field measurements. Finally, let us mention a recent work of Abbassi et al. [2], where an Artificial Neural Networks is coupled with DIC measurements to perform the identification of the GTN model parameters. According to the authors, such an approach leads to considerable computational time gain.

5.2 Influence of the regularization parameter

In this section, the influence of the non-local regularization parameter (see chapter 2, equation 2.32) is investigated both within the hardening regime and the softening regime. Indeed, although this parameter allows the correct simulation of the mechanical response during the softening phase, the regularization is made on the cumulated plasticity field, which appears prior to softening.

Hardening regime The sensitivity analysis presented in appendix E, shows that, within the plastic regime, the sensitivity of displacement and force with respect to the regularization parameter is negligible, since it cannot be captured by the current measurement systems. Hence, knowing that the uncertainties of the considered measurement systems are relatively small (± 0.001 mm and ± 200 N), the regularization parameter is to be considered as a parameter without any influence within the hardening regime. However, let us note that this conclusion is relative to the considered non-local model[1]. A rather clear illustration of this negligible influence is visible in figure 5.1, with the evolution of the cost function with respect to the regularization parameter and the Hosford exponent within the plastic regime. The convexity with respect to the regularization parameter is insignificant compared to the convexity with respect to the Hosford exponent.

Softening regime The influence of the regularization parameter becomes significant (with respect to the measurement uncertainty) within the softening phase, as visible in figure E.9. Nevertheless, the guess value of the regularization parameter remained unaltered during an identification attempt (see table 5.1). This result was attributed to the competing influence between the regularization parameter and the remaining damage parameters, as visible in figures E.9 and E.7. Let us note that the influence of the regularization parameter is one order of magnitude lower than the GTN parameters, so that a minimal variation of the GTN parameters compensates for the contribution of the regularization parameter in terms of displacements.

Nevertheless, let us note that although a value of the regularization parameter cannot be identified in this study, the considered non-local model provides solutions independent from the mesh size and orientation. Therefore, also the FEMU technique provides parameters which do

[1] From another point of view, this analysis shows that the regularization parameter of the considered non-local model does not alter the solution of the corresponding local model within the plastic regime.

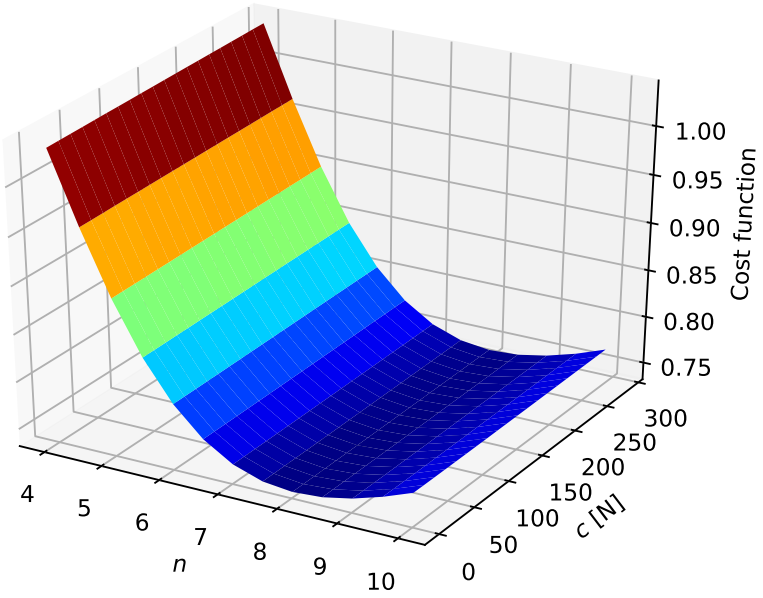

Figure 5.1: Evolution of the displacement cost function with respect to the Hosford exponent and the regularization parameter. The cost function takes an approximatively constant value along the regularization parameter axis.

not depend on the mesh characteristics and can be used to simulate specimens with different mesh sizes.

5.3 Application of FEMU

The approach retained in the present study considers all the GTN parameters as phenomenological terms, except for the initial void volume fraction ($f_0 = 1 \times 10^{-4}$) measured be means of SEM observations. Furthermore, no empirical relations between the parameters are considered.

5.3.1 Identification

The sensitivity analysis (see appendix E) showed a clear competition between the various parameters of the GTN model, leading to a potential indetermination. Therefore, the choice has been made to lock parameters q_1 and q_2 since their purpose is to control void growth, which has been shown to be a minor phenomenon compared to void coalescence for Inconel 625 (see section 1.4). Furthermore, according to the literature, their values do not vary significantly for metallic materials [13, 41, 130, 131]. The values of parameters q_1 and q_2 were then fixed at 1.5 and 1 respectively, as originally proposed by Tvergaard and Needleman [131].

The FEMU was thus used to identify the 4 remaining parameters, denoted k, p_s, f_c, f_r as in equations 2.18 and 2.15, which guess values are reported in table 5.1. The guess values are representative of the observations of chapter 1: according to the SEM analysis, void growth is negligible ($< 5 \times 10^{-4}$) up to a $\varepsilon \approx 35\%$ of deformation. For this reason, void nucleation is considered the principal mechanism leading to the critical level of void volume fraction. Thus, relatively high values for the nucleation parameters are taken as guess values. Furthermore, according to the analysis of the elastic unloads, no loss of stiffness was observed up to a deformation of 50%, meaning that there should not be a significant void volume fraction. Considering that the material generally breaks at strain levels slightly higher than 50%, the assumption is that failure occurs at a relatively low level of void volume fraction ($f_r = [0.10 - 0.25]$).

Solely the flat geometries were considered for the characterization of damage. In fact, due to their relatively small thickness (compared to the diameter of the axisymmetric specimens), the mechanical solution is characterized by a negligible gradient along the thickness direction (see, for example, the stress triaxiality evolution in figure 5.2). In this way, what is measured on the surface by DIC is considered as representative of the behaviour at core. Besides fracture initiation is not observable for axisymmetric geometries since it occurs at the center of the notched specimens.

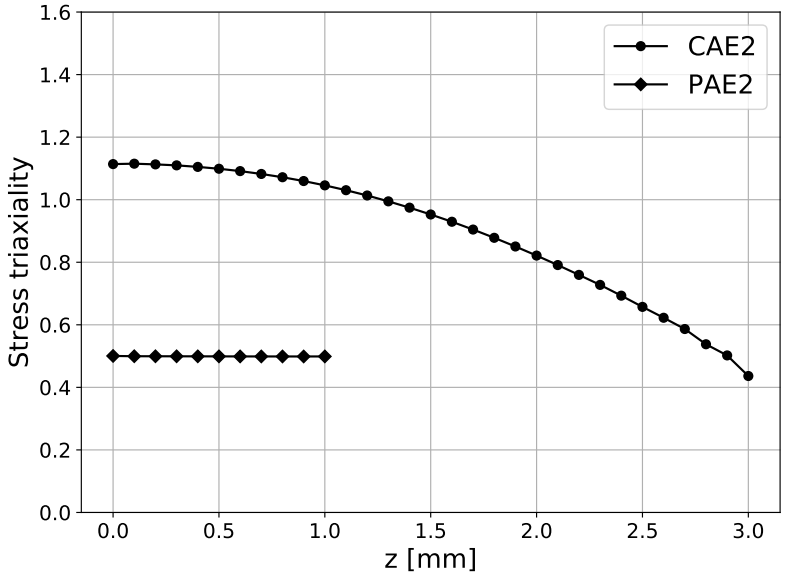

Figure 5.2: Comparison of the stress triaxiality along the thickness direction between flat and axisymmetric geometries. The values are calculated at the center of the specimen.

In order to limit the computational time of the identification, the damage parameters were identified on solely the test PAE2-1[2] (see figure 1.5(b)).

[2]Each simulation involved in the algorithm is run up to the onset of fracture. Hence, the 3D implicit simulation of geometry PAE2 required approximatively 10 hours of calculation with ~ 80000 degrees of freedom. Moreover, the computational time of one simulation affects the time of the identification, since the time of one simulation is multiplied by sum of the number of iteration of the identification process plus the number of evaluations of the Jacobian matrix.

FEMU was run considering a repartition coefficient $\alpha = 0.5$ to minimize both the force gap and the displacement gap. All the 3 displacement directions were considered within the cost function ($N_{dim} = 3$). The Region of Interest Ω is a rectangular zone corresponding approximatively to the refined region of the mesh showed in appendix E. The considered time interval corresponds approximatively to the last stage of hardening plus the entire softening phase. The identified values are reported in the table 5.1

Identification on test PAE2-1			
Parameter	Guess Value	FEMU	Unit
f_c	0.10	0.063	
f_r	0.25	0.127	
p_s	0.4	0.458	
k	0.6	0.49	
c	40	39.98	[N]

Table 5.1: Results of damage parameter identification. The non-local regularization parameter c remained unaltered.

5.3.2 Verification

The identified parameters were at first used to simulated the PAE2 geometry, which test number 1 served for the identification. Each test was simulated prescribing the measured displacements as boundary conditions. One the one hand, figure 5.3 shows that the onset of softening is correctly reproduced for test PAE2-1, as expected. On the other hand, figure 5.3 shows that the identified parameters allows also to simulate correctly the onset of softening on the same geometry with a different loading (the effective boundary conditions are not strictly the same for all tests), and different meshes (for PAE2-3). The premature failure predicted for specimen PAE2-3 is due to the higher deformation at failure showed experimentally, which cannot be modelled with the parameters identified on test PAE2-1. These observation confirms the aptitude of FEMU for the identification of the damage parameters for the initiation stage.

Let us also note that the simulated spatial distribution of void volume fraction is consistent with the physical crack observed experimentally for specimens PAE2-1 and PAE2-2, as visible in figures 5.4 and 5.5. This result is obtained thanks to the application of measured boundary conditions. The comparison for specimen PAE2-3 is not showed here, since when the simulation stopped, no crack is visible on the real specimen. Indeed, at this point, the measured boundary conditions correspond to a stable hardening phase. Consequently the simulation of void volume fraction is equally distributed on both the roots of the notch, as visible in figure 5.3.

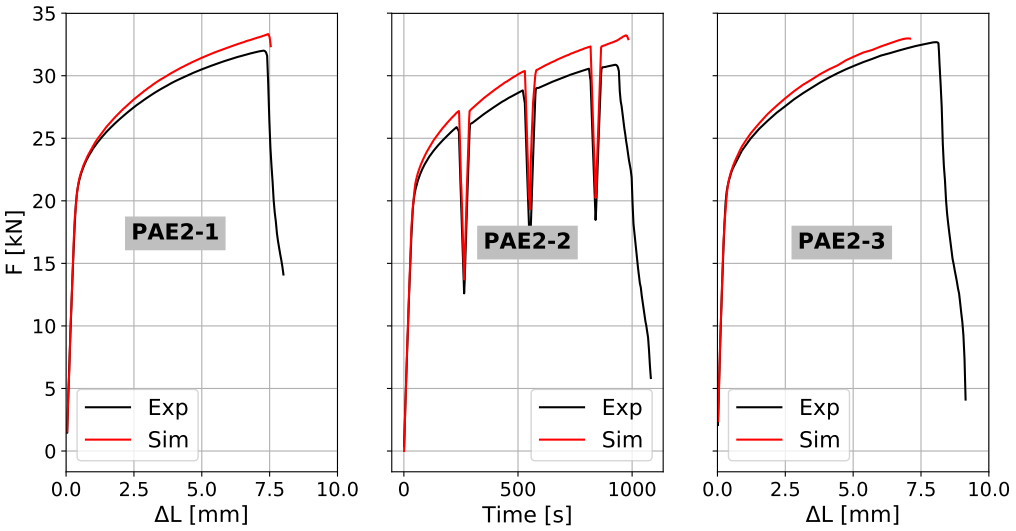

(a) Force versus time (machine displacement)

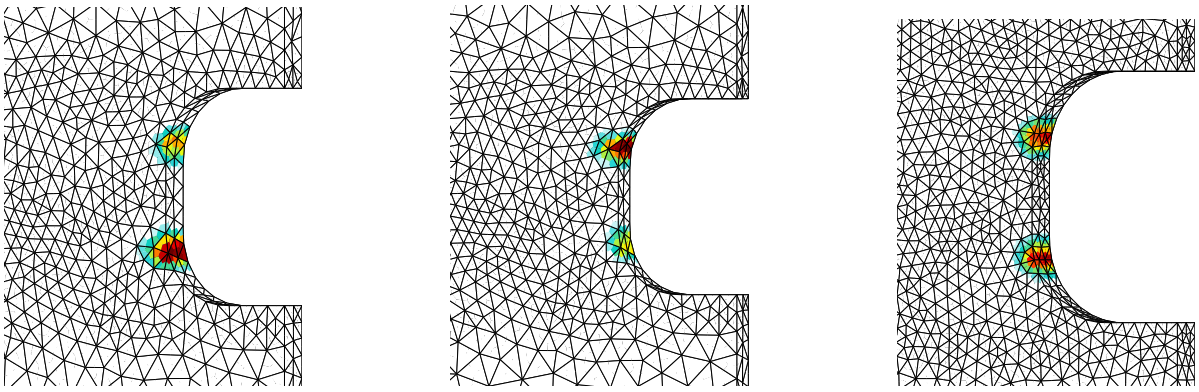

(b) PAE2-1 (c) PAE2-2 (d) PAE2-3

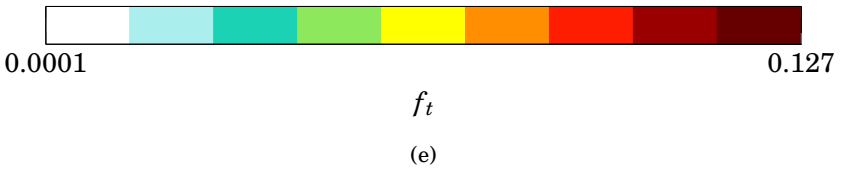

(e)

Figure 5.3: Top: comparison between experimental result and simulation for 3 PAE2 specimens tested. The simulation are made using the identified damage parameters. Bottom: spatial distribution of void volume fraction. The simulations stopped because of a convergence issue arising once the critical void volume fraction value $f_r = 0.127$ is reached.

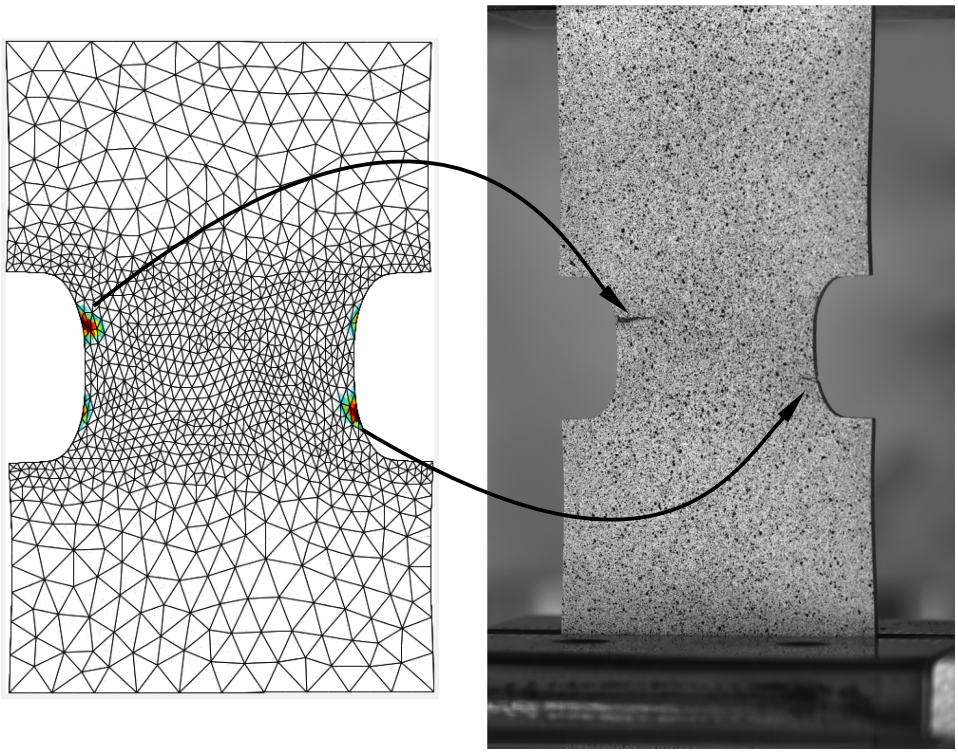

Figure 5.4: Comparison between the simulated void volume fraction (left) and the real crack (right) for test PAE2-1. The simulation's result is shown synchronized with the image.

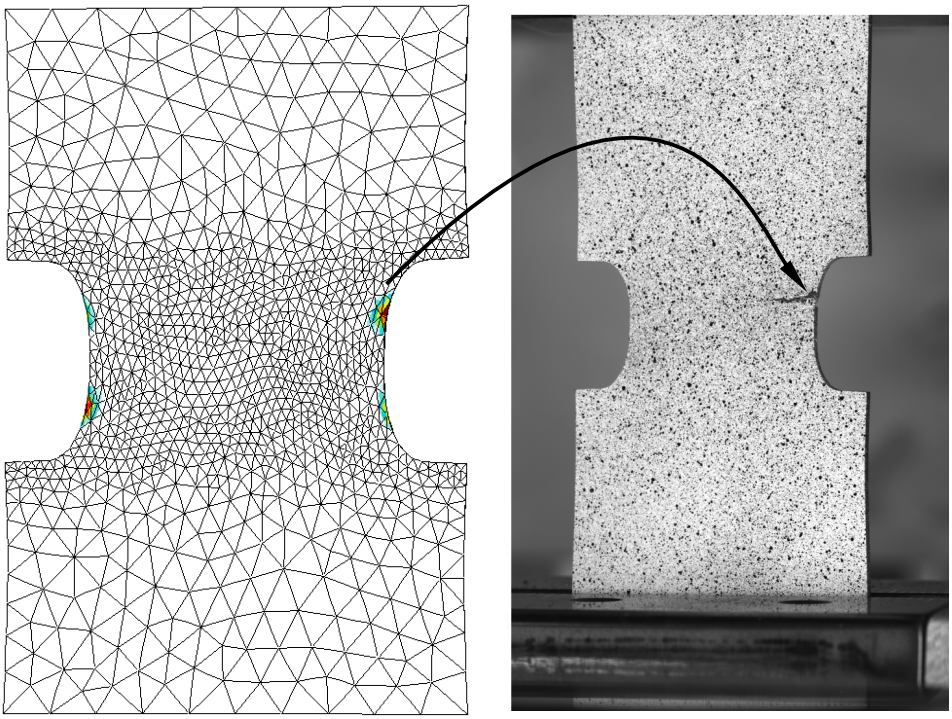

Figure 5.5: Comparison between the simulated void volume fraction (left) and the real crack (right) for test PAE2-2. The simulation's result is shown synchronized with the image.

5.4 Validation of the damage parameters

The validation of the identified parameters needs to take into account specimens different from those used for the identification. To do so, two groups of geometries have been considered. The first group is formed by the tests that were taken into account for the identification of the plasticity parameters (see section 4.4), but excluded from the identification of the damage parameters because of the computational time constraint: *i.e.* all the axisymmetric geometries, together with the PAE1 and the plane-strain geometry. The second group is formed by tests on more complex geometries, which failure is not trivial to predict.

5.4.1 Validation on the first group of specimens

Figures 5.8, 5.6 and 5.7 compare the simulated load with the experimental one. The validation is based on the capacity of the model to predict the onset of failure. Let us note that all the simulations stopped because of convergence difficulties appearing once the critical value of void volume fraction is reached.

The simulation of the onset of failure is satisfactory for all the flat specimens and the plane strain specimen, as visible in figures 5.6 and 5.7. Let us note that for specimen PAE1-2 (as for specimen PAE2-3), the simulated onset of failure is premature since the experimental response of specimen PAE1-2 showed higher deformation at failure than specimen PAE1-1 (see figure 1.11(b)). The consistent scattering at failure could be taken into account by enlarging the number of tests considered for the identification of the damage parameters. It would then be interesting to determine not only a set of parameters but also a confidence interval around a mean macroscopic response.

The simulations of the axisymmetric geometries are encouraging, as visible in figure 5.8, since the all the simulations, except for CAE2-1, predict failure after the maximum experimental load is reached. Nevertheless, the simulated failure happens too rapidly (quasi vertical load drop). Indeed, the axisymmetric geometries have a different stress triaxiality level, which is not taken into account by identifying the parameters on an unique flat geometry. A possible solution is to consider both axisymmetric and flat geometries for the identification of the damage parameters.

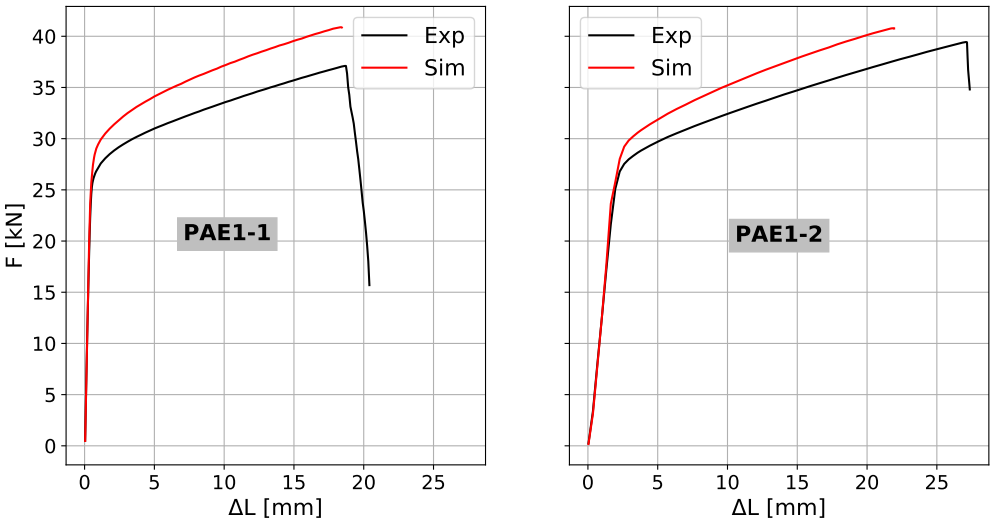

(a) Force versus time (machine displacement)

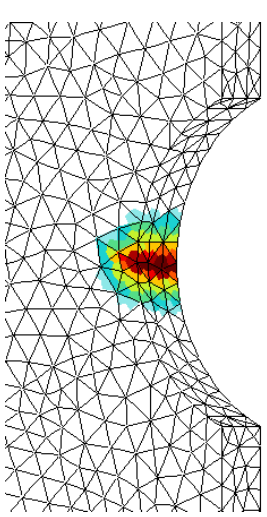

(b) PAE1-1

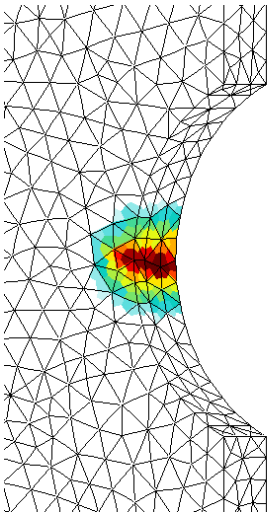

(c) PAE1-2

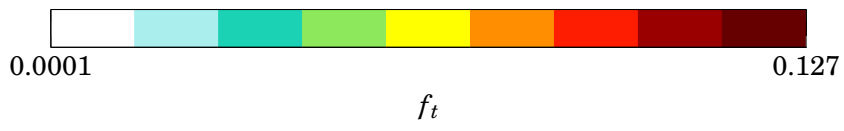

(d)

Figure 5.6: Simulation of the PAE1 specimens using the parameters identified via FEMU on test PAE2-1. The simulations stopped because of a convergence issue arising once the critical void volume fraction value $f_r = 0.127$ is reached.

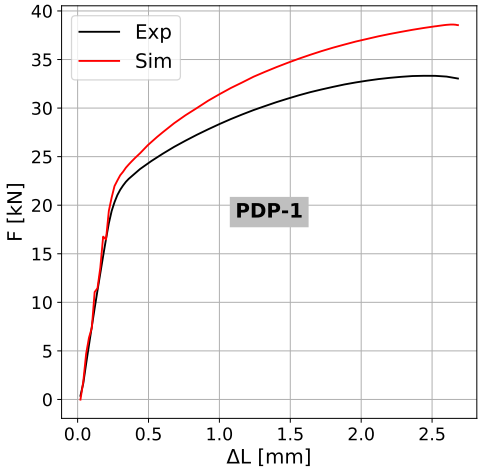

Figure 5.7: Simulation of the plane strain specimen using the parameters identified via FEMU on test PAE2-1. The simulations stopped because of a convergence issue arising once the critical void volume fraction value $f_r = 0.127$ is reached.

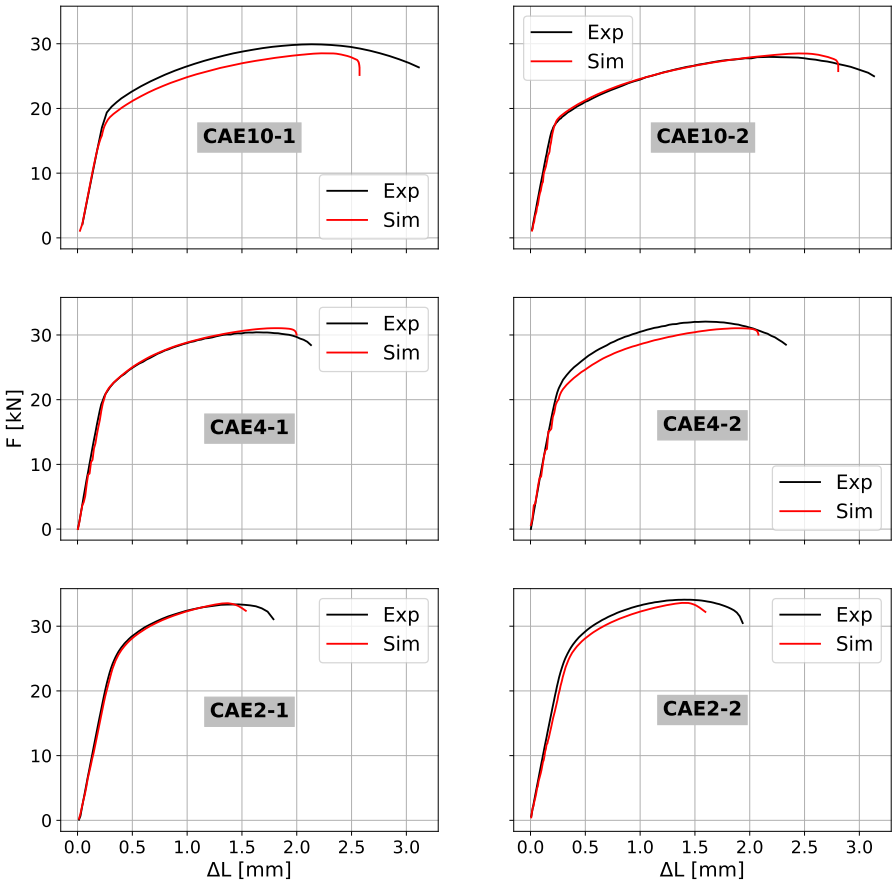

Figure 5.8: Simulation of the axisymmetric specimens using the parameters identified via FEMU on test PAE2-1. The simulations stopped because of a convergence issue arising once the critical void volume fraction value $f_r = 0.127$ is reached.

5.4.2 Validation on the second group of specimens

The second group of geometries considered for the validation of the identified parameters are inspired from the first two editions of the Sandia Fracture Challenge [18, 19]. The challenges consisted in simulating the ductile failure of specimens characterized by an unusual arrangement of geometrical non-linearities (notches and holes that induce a complex failure). In this work, the geometrical features of the original geometries are kept, while their size is scaled to allow the machining within the 30 mm round bar available (see the plans in figure 5.4.2). These geometries will be referred to as Sandia 1 and Sandia 2.

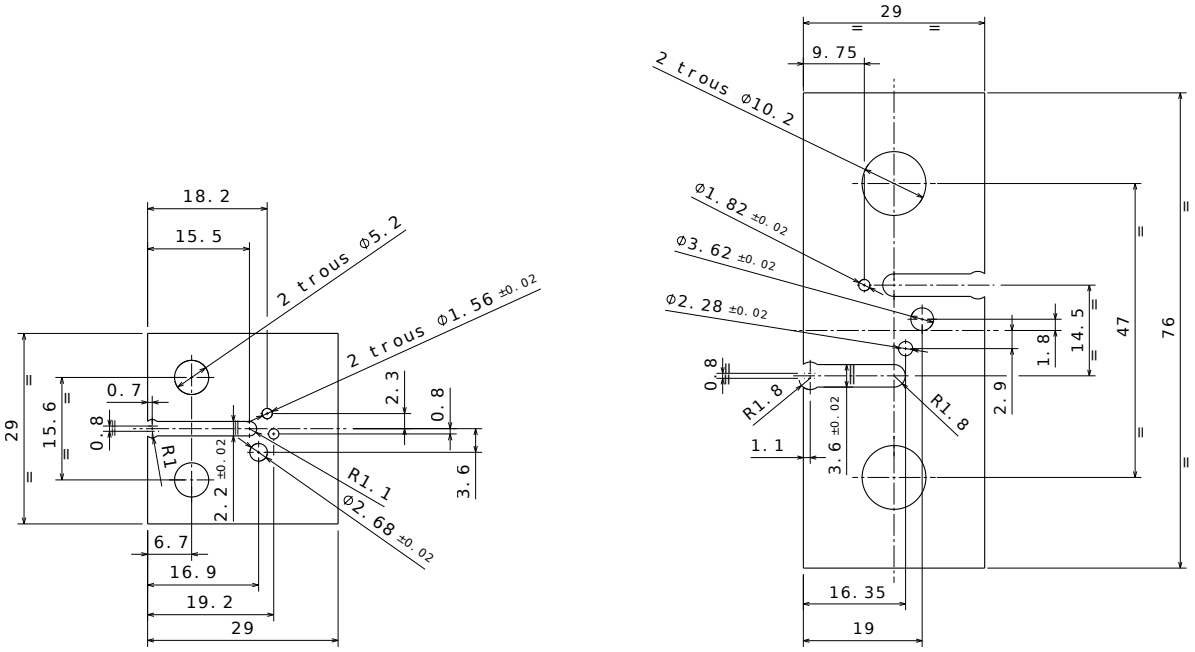

(a) Sandia 1 (b) Sandia 2

Figure 5.9: Sketches of specimens Sandia 1 and Sandia 2, both inspired from the Sandia Fracture Challenges. Specimens are 2 mm thick.

Experimental tests The evolution of the measured force versus the prescribed machine displacement is showed in figure 5.10(a) for Sandia 1 and in figure 5.11(a) for Sandia 2. Unlike the tests described in chapter 1, the Sandia specimens do not show a considerable scattering at failure. The experimental response is reproducible. The difference between the macroscopic response of the third Sandia 1 specimens compared to the other tests on the same geometry, is due to a different crack path, as visible in figure 5.10(b). It is interesting to note that a first crack appeared in specimen Sandia1-3 at the same location of the other Sandia1 specimens, but this first crack stopped and a second crack propagated up to failure through a different hole. Instead, the crack propagation for the Sandia 2 specimens was similar for each tests, as visible in figure 5.11(b).

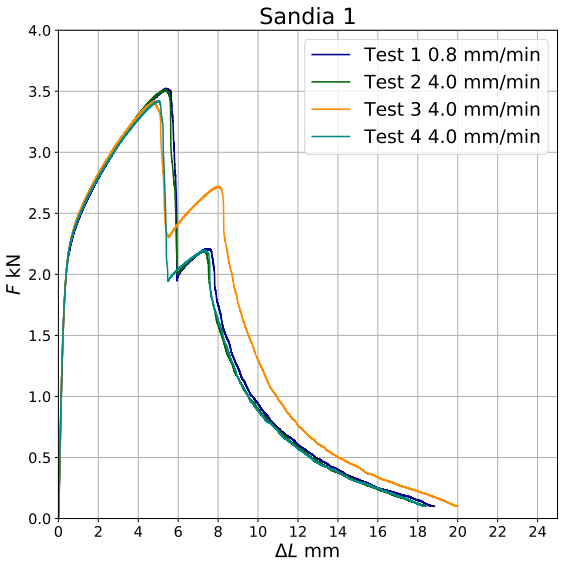

(a) Force vs. machine displacement

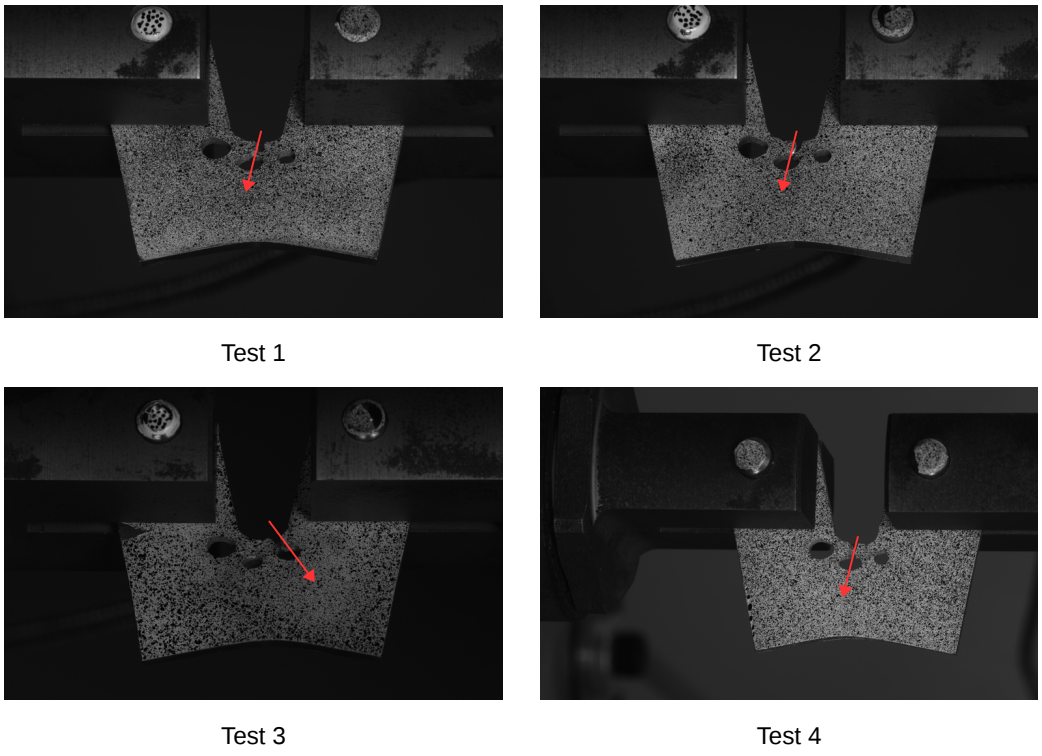

(b) Crack paths

Figure 5.10: Experimental results for geometry Sandia 1. Four tests have been performed considering 2 different loading rates. The curves show a negligible scattering of the response. The different crack paths (indicated with red arrows) explain the discrepancy between the results.

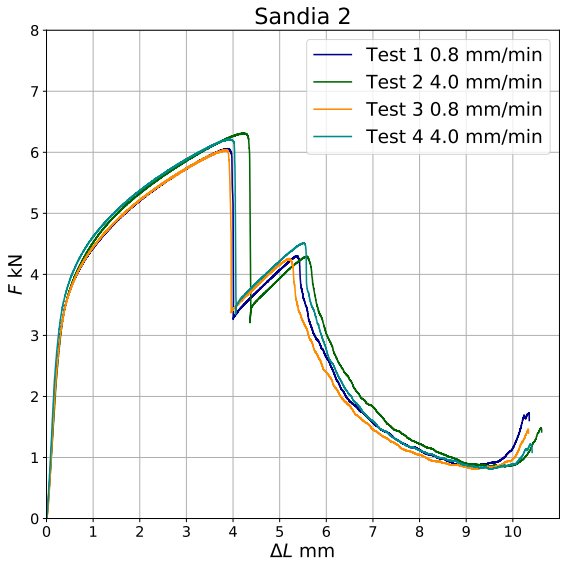

(a) Force vs. machine displacement

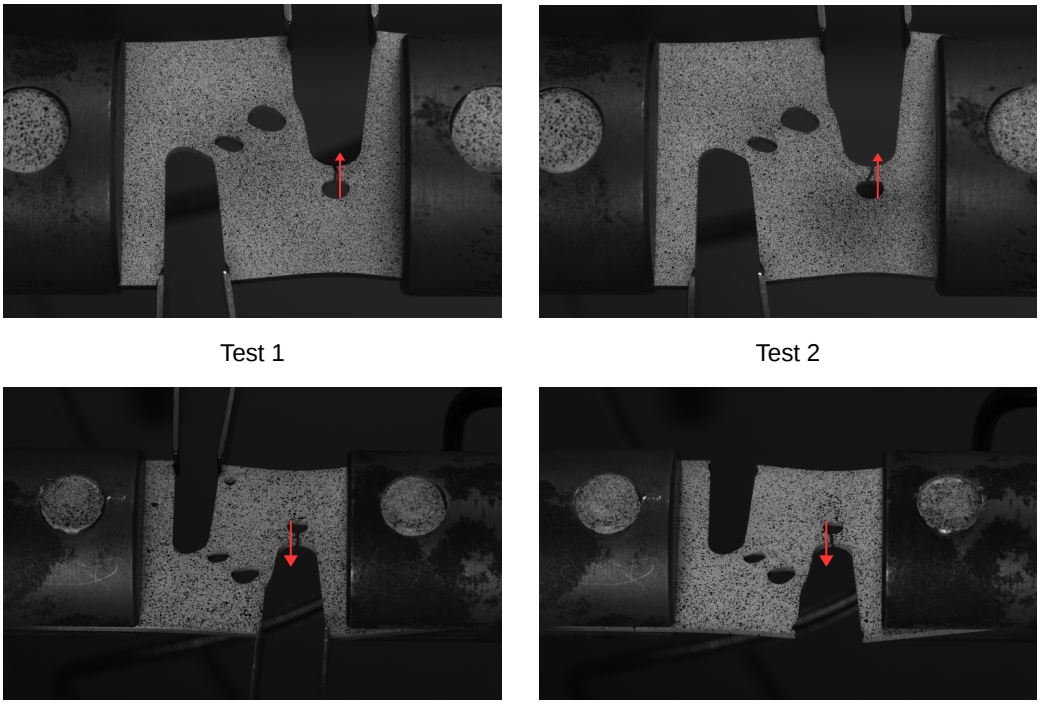

(b) Crack paths

Figure 5.11: Experimental results for geometry Sandia 2. Four tests have been performed considering 2 different loading rates. The curves show a negligible scattering of the response. All tests show similar crack paths (indicated with red arrows).

Simulations Figures 5.12 and 5.13 compare the experimental responses with their simulated counterparts for both Sandia specimens. Although the experimental scattering within the hardening regime of specimen Sandia 1 is negligible, it is not the case for the numerical responses. Such a difference is attributed to the prescription of measured boundary conditions, which is altered by the matching uncertainty (see appendix B) because of the high displacement gradient in correspondence with the mesh boundaries (the relatively small dimension of the specimen accentuate the error). Therefore, in the following, solely the Sandia 2 specimens are evaluated. The simulation of the onset of fracture is satisfactory. Moreover, the positions of the simulated maxima of void volume fraction is in agreement with the actual positions of the cracks, which initiate from the interior of the holes towards the notch roots (see figure 5.11(b)).

The experimental failure of the Sandia 2 specimens is highly repeatable. Consequently, the corresponding boundary conditions applied for the simulations of each specimen are very similar. This explains why the simulations lead to similar macroscopic responses: every time, the simulated fracture point is underestimated with respect to the experimental one. It would be interesting to check whether this difference is consistent with a confidence interval (which needs to be determined).

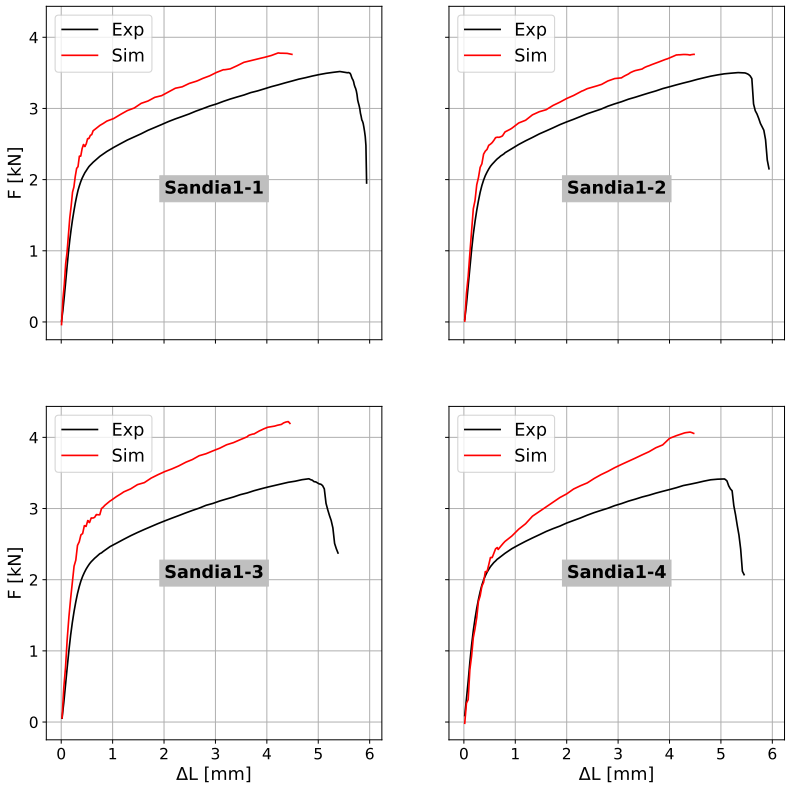

Figure 5.12: Comparison between simulation and experiment for the Sandia 1 specimen. The simulations stopped because of a convergence issue arising once the critical void volume fraction value $f_r = 0.127$ is reached. The differences between the simulated loads are mainly attributed to the matching uncertainty (see appendix B).

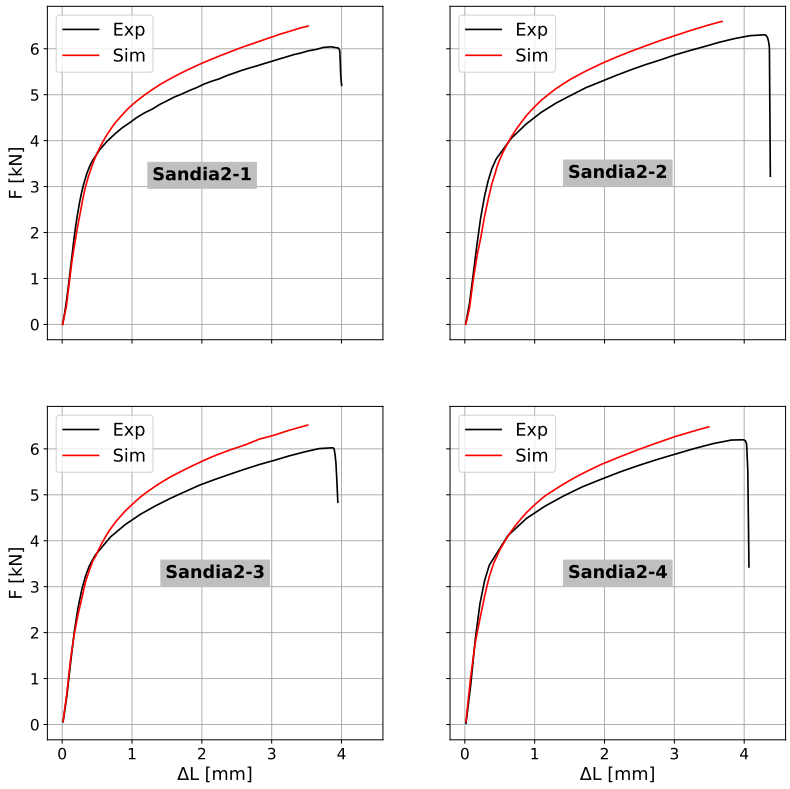

Figure 5.13: Comparison between simulation and experiment for the Sandia 2 specimen. The simulations stopped because of a convergence issue arising once the critical void volume fraction value $f_r = 0.127$ is reached. The differences between the simulated loads are mainly attributed to the matching uncertainty (see appendix B).

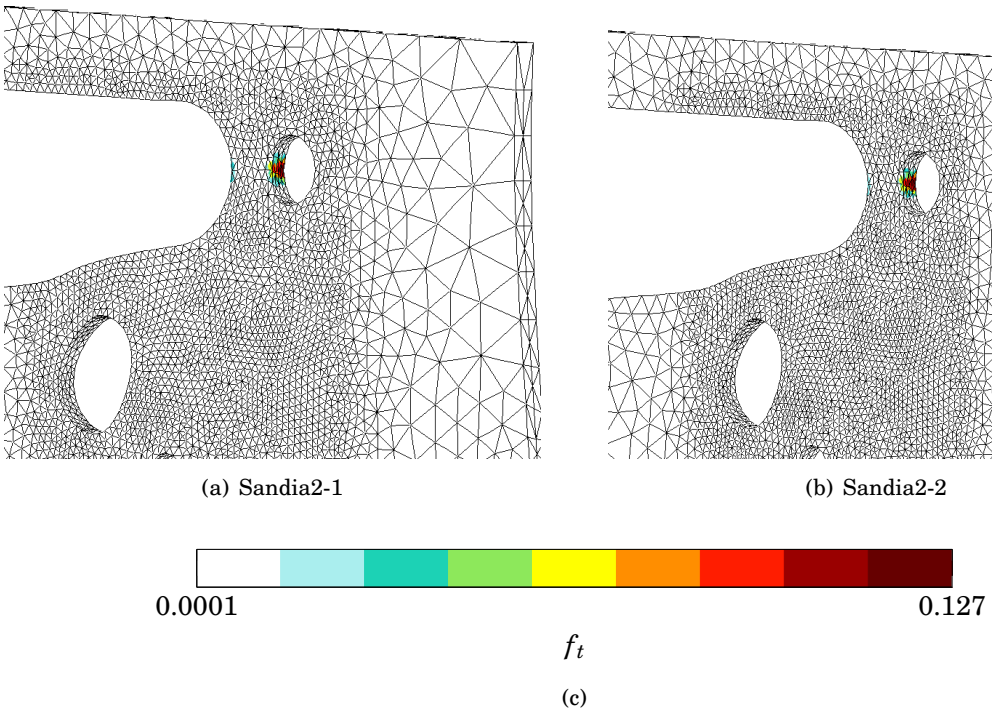

(a) Sandia2-1 (b) Sandia2-2

(c)

Figure 5.14: Simulated void volume fraction for two Sandia 2 specimens. The simulations stopped because of a convergence issue arising once the critical void volume fraction value $f_r = 0.127$ is reached. The simulated location of void volume fraction is in agreement with the real cracks showed in figure 5.11(b).

The results on the flat specimens confirm the FEMU method as a potential approach for the identification of the damage parameters to satisfactorily simulate the onset of fracture. Furthermore, they confirm the necessity to take into account the experimental scattering at failure by considering several tests for the identification process, and to define a confidence interval. The results on the axisymmetric specimens confirm the necessity to take into account different levels of stress triaxiality for the identification of the ductile damage parameters. Therefore, before investigating unmodeled phenomena, it is necessary to utilise the entire database.

Résumé

Dans ce dernier chapitre, la stratégie d'identification développée est utilisée pour identifier des paramètres du modèle d'endommagement GTN pour l'Inconel625. Une seule éprouvette plane entaillée est utilisée pour cette opération afin de réduire les temps de calcul.
L'analyse de sensibilité montre que tous les paramètres du modèle GTN sont en compétition dans la zone d'intérêt sur l'éprouvette et que cela provoque une indétermination sur l'identification des paramètres. Afin de réduire cette indétermination, les valeurs des paramètres liés à la croissance des cavités sont choisies a priori car ce phénomène n'est pas prépondérant pour l'Inconel625. Les paramètres inconnus restants sont identifiés par FEMU et validés par comparaison essai-calcul. Parmi ceux-ci, seul le paramètre de régularisation du modèle non-local n'a pas pu être identifié jusqu'à amorçage pour l'Inconel625, car ce matériau est manifestement peu sensible au paramètre dans ces conditions.
Plusieurs résultats sont tirés de la validation sur l'essai ayant servi pour l'identification des paramètres. D'une part, l'instant d'amorçage de la fissure est bien reproduit malgré la dispersion expérimentale du matériau, qui n'est pas prise en compte. D'autre part, le site d'amorçage est bien prédit malgré l'indétermination générée par la symétrie de l'éprouvette, et ce grâce à l'imposition des conditions limites réelles. Des conclusions similaires sont obtenues pour les simulations des autres essais sur la même géométrie avec des conditions aux bords différentes et sur les autres géométries planes.

Conclusion

The present work proposes a parameter identification strategy for plastic behaviour and damage up to the onset of fracture. The strategy uses both load and full-field measurements. It is developed into a regularized damage framework. The proposed approach is based on a Finite Element Model Updating (FEMU) technique, according to which the parameters are identified by minimizing the discrepancy between experiment and simulation, quantified by means of a cost function.

There are two main particularities that characterize the proposed identification strategy with respect to other FEMU-based strategies. The first particularity concerns the cost function, which quantifies the discrepancy between experiment and simulation in terms of load and displacement. These two different quantities are combined into a unique scalar value by means of appropriate weights. Furthermore, the use of integral formulations allows to obtain values independent on external factors, as the number of nodes. The second particularity concerns the management of the boundary conditions, which might be considered as the principal issue regarding FEMU. The measured displacements are prescribed as boundary conditions for the finite element problem, in order to ensure the consistency of the simulation with respect to the experiment. It is shown that prescribing boundary conditions polluted by the measurement uncertainty has a negative effect on the finite element solution. An innovative filtering technique based on the Robin boundary condition is proposed and tested together with classical filtering approaches, as the moving least squares and polynomial approximations.

Although the strategy intends to be general, a specific material is chosen to perform the tests. The superalloy Inconel 625, used in the aeronautic industry, is retained. The specimens' geometries are selected to generate a heterogeneous spatial distribution of the kinematic fields, in order to fully use the richness of information of the Digital Image Correlation (DIC) measurements. The efficient DIC algorithm FOLKI-D is used to obtain dense (pixel-wise) results without any post-filtering operation on the computed fields. Ten different geometries (flat and axisymmetric), with two to four specimens for each geometry, are tested up to fracture, for a total number of 26 tests.

Fractographic observations allow to confirm the isotropic character of the material behaviour. Further microscopic observation is used to determine the initial void volume fraction. The microscopic analysis also permits to assume that failure of Inconel 625 is due to a strong nucleation of new voids occurring at a high cumulated plasticity level. The experimental macroscopic responses show a considerable scattering both within the plastic domain and at failure.

The observed ductile behaviour is modelled using an Hosford yield criterion and a Voce-like isotropic hardening law. Damage is modelled using the well-known GTN model, able to reproduce the observed sequence of strong void nucleation and coalescence. The simulation of a softening behaviour requires a non-local regularization, which is here obtained by introducing the gradient

of the cumulated plasticity into the free Helmholtz energy density. Furthermore, the well known volumetric locking problem is solved by means of mixed displacement-pressure-volume variation elements. Because of the large deformations reached by Inconel 625, an additive logarithmic formulation is considered. All the computations involve an unstructured 3D mesh, and are performed with an implicit solver (locally and globally).

The elastic modulus and the 5 hardening parameters are identified by means of a classical approach (*i.e.* curve fitting). The GTN parameters q_1 and q_2 are fixed according to the literature, as microscopic observations have evidenced very little void growth, which means that their identification is prone to be difficult. The same observations allow to determine the initial void volume fraction and guess values for the remaining unknown parameters.

The 6 remaining parameters are identified using the proposed FEMU technique, which implementation is validated by comparing the previous hardening parameters with the FEMU identified ones. The feasibility of the identification is assessed based on a sensitivity analysis. It is indeed necessary to verify that the observed quantities (force, displacement) are sensitive with respect to the unknown parameters. The identification is considered as possible if a small perturbation of the parameters induces an absolute variation of force and displacement which is at least comparable with the uncertainty of the measurement instrument.

This analysis indicates that the transversal displacement (with respect to the loading direction) is, for the flat specimens, the most sensitive with respect to the Hosford exponent, while the same parameter has a negligible influence on the force response. For this reason the Hosford exponent is identified by minimizing the transversal displacement discrepancy using the FEMU method.

The same sensitivity analysis shows that the regularization parameter of the considered non-local model does not induce a significant variation neither on force nor on displacement. Although the regularization parameter cannot be identified, the non-local model gives to the finite element solution the regularization necessary to obtain results independent from the mesh size and dimension.

The sensitivity analysis of the 4 remaining GTN parameters shows that it is possible to identify them by considering both force and displacement on flat specimens. The identification via FEMU of these parameters is then carried out on a unique specimen, to limit the computational time.

The identification strategy is validated based on the comparison between experiment and simulation for all the 8 notched geometries. The identified parameters are consistent with the microscopic observations. Indeed, they allow to simulate the minimal void growth prior to the onset of softening and the subsequent rapid failure due to void nucleation. For the flat specimens, the onset of softening is satisfactorily predicted and the positions of the simulated maxima of void volume fraction are in agreement with the actual positions of the cracks, even when several locations are possible.

The simulations of specimen Sandia 1 underline the difficulties of the alignment between the DIC coordinate system and the FE coordinate system when the mesh boundaries correspond to high displacement gradient areas. The identification results confirm the necessity to take into account the experimental scattering at failure and different stress triaxiality levels, especially for ductile behaviours. This can be achieved by utilising several specimens for the identification of the damage parameters.

Perspectives

Several challenges still need to be faced to obtain a more robust parameter identification using the proposed strategy, from the numerical point of view as well from the experimental point of view.

First of all, the stability of the approach should be verified testing several guess values for the damage parameters, as done for the plasticity parameters. Such an operation, which requires a significant amount of computational time, is indispensable to verify that the solution is a global minimum. Moreover, the stability and robustness of the approach, should be tested by performing parameter identification on materials characterized by different failure mechanisms (*e.g.* with a significant void growth).

Furthermore, the accuracy of the method needs to be increased by improving the technique for the alignment of the coordinate systems. In fact, such an operation is actually based on the selection of points that are generally on the border of a specimens, where the quality of the image might not be excellent. Printing a regular and specific speckle (totally or partially) appears to be a possible solution. In this way, the proposed identification technique might be used to investigate scale effects, since the comparison between experiment and simulation on small specimens will be more accurate.

The computational time of the identification should be reduced, and this operation is not feasible solely by means of parallel computation. The computation of the Jacobian matrix appears to be the heaviest operation, so the investigation of semi-analytical calculations could have a beneficial impact on the identification time.

The simulations of this work are run up to the onset of failure. A robust damage-to-fracture transition tool appears then necessary to run the simulations up to the complete failure. The proposed identification approach might then be used to identify the parameters related to crack insertion.

It would also be interesting to work on shape optimization techniques to improve test definition. In fact, as it is shown in this work, the concurring influence of the various parameters often leads to an indetermination: there exists a multitude of combinations of parameters which gives a unique spatial distribution of displacement. Shape optimization might lead to specimen geometries (and relative loading conditions) that isolate the influence of each parameter on a different zone.

Finally, it would be interesting to study the propagation of the material scattering from the experimental responses to the identified parameters. In this way, it would be possible to identify not only a set of parameters, but also a confidence interval.

Résumé

Cette thèse propose une approche d'identification des paramètres de plasticité et d'endommagement jusqu'à amorçage. L'approche proposée prend en compte à la fois les efforts et les mesures de champ denses issues de la corrélation d'images. La stratégie d'identification est développée en considérant un modèle d'endommagement régularisé. Elle est fondée sur une méthode de type recalage de modèle éléments finis (FEMU), selon laquelle les paramètres sont identifiés en minimisant l'écart entre une mesure et son pendant simulé.
Une attention particulière est mise sur la gestion des conditions au bord: les déplacements mesurés sont utilisés pour piloter le calcul éléments finis afin d'en assurer la cohérence avec la mesure expérimentale. Cette opération génère des problèmes sur la solution mécanique à cause des incertitudes de mesure. Une technique de filtrage innovante et automatique est proposée, basée sur la condition au bord de Robin.
L'implantation de la stratégie d'identification est validée sur la base de l'identification des paramètres d'écrouissage par comparaison avec les résultats d'une technique standard. La stratégie est ensuite utilisée pour identifier un critère de plasticité de type Hosford et les paramètres d'endommagement du modèle GTN les plus influents. Les valeurs obtenues sont validées par comparaison de l'instant et du site d'amorçage entre essai et calcul.
Plusieurs pistes sont possibles pour poursuivre le développement de la stratégie proposée. Tout d'abord, pour prendre en compte la dispersion expérimentale il faudrait mener l'identification sur plusieurs essais afin d'obtenir un jeu de paramètres moyens et un intervalle de confiance associé. De plus, plusieurs valeurs de départ pour l'optimisation devraient être testées afin de vérifier l'unicité de la solution. Ensuite, il serait intéressant d'améliorer la technique pour l'alignement des repères éléments finis et corrélation d'images, afin d'augmenter la robustesse de la comparaison essai-calcul. Enfin, une dernière amélioration concerne l'optimisation des géométries pour réduire la compétition entre paramètres sur une même zone de l'éprouvette.

APPENDIX A

CHARACTERISTICS OF THE STUDIED INCONEL 625

This appendix provides a brief description of Inconel 625. The material was annealed at 1025°C, held 30 minutes, and furnace cooled. It was supplied in form of bars of 30 mm diameter. The chemical composition is reported in table A.1, as declared by the supplier. The microstructure was investigated at the Scanning Electron Microscope (SEM). It was observed an average grain size of around 30 μm as in figure A.1(a). Moreover, the SEM analysis showed the presence of equally distributed micro-voids and intermetallic precipitates as in figure A.1(b). This observation is consistent with the literature on the nickel-based superalloys [16, 119]. However, in this work the various precipitates are considered as a unique phase and quantified by means of their fraction of occupied volume.

Al	C	Cb(Nb)+Ta	Co	Cr	Fe	Mn	Mo
0.24	0.02	3.61	< 0.10	21.99	0.52	0.27	8.75
Ni	P	S	Si	Ti			
Balance	< 0.005	< 0.002	0.08	0.2			

Table A.1: Chemical composition of Inconel 625. Source: Haynes International

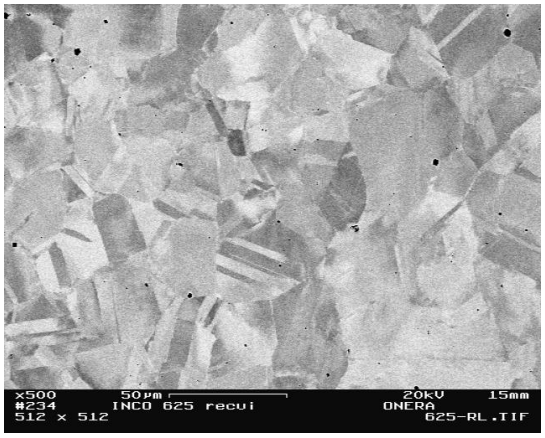

(a) Microstructure of an annealed Inconel 625. The grain size varies from a minimal value of $5\mu m$ to a maximal value of $50\mu m$

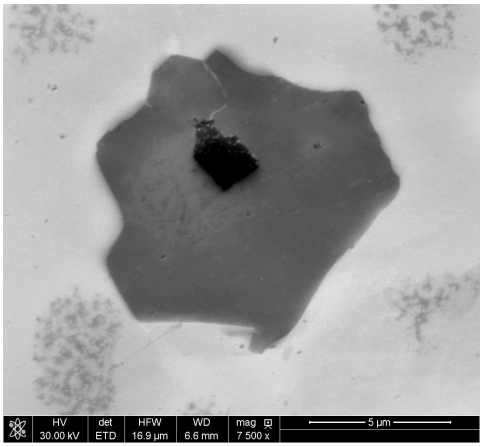

(b) Generic intermetallic precipitate of an annealed Inconel 625.

Figure A.1: Microstructure observation

APPENDIX B

COMPARISON OF THE EXPERIMENTAL DISPLACEMENT FIELDS WITH THEIR SIMULATED COUNTERPARTS

This appendix describes the technique used both to transfer the measured boundary conditions on the finite element mesh and to compare the experimental displacement fields with their simulated counterparts. Indeed, these latter quantities are, in general, not available within the same coordinate system. An alignment procedure is then essential to accomplish the comparison. Furthermore, an additional transfer is usually necessary since the nodes of the finite element mesh are not located at the center of a pixel in the image.

B.1 Alignment of the experimental (DIC) and numerical (FE) spatial coordinates systems

A straightforward approach to align the DIC coordinate system with the FE coordinate system consists in meshing the geometry reconstructed from the DIC measurements, as made in reference [115]. In this way, the real geometry of the specimen is potentially taken into account. However, this technique might lead to a mesh which edges are not consistent with the real edges of the specimen, since the DIC algorithms do not provide a result within a finite zone around the boundaries (the dimension of this zone depends on the considered algorithm). As a consequence, the mismatch between FE model and real geometry leads to compute an external reaction which is not comparable with the experimental force. Since this inconvenient alters the identification result of FEMU, this approach is not taken into account.

Instead, an indirect approach is considered, which applications might be found within the literature about parameter identification [97, 109], and consists in performing a feature-based pose estimation [125]. It can be seen as an extrinsic calibration problem, in opposition with the intrinsic calibration of the DIC system. This approach requires the selection of a certain number of remarkable features on the CAO model. These features are then matched (manually or automatically) on the reference image, where the DIC results are available. In the present case the choice is restricted to corner points which are manually matched within the reference

image. The matched points allow to identify, usually by optimizing a least-squares criterion, the parameters of the underlying transformation model (translation, rotation, etc.).

Two transformation models are considered in this study: an homography transformation and a Perspective-n-Points (PnP) transformation. Both are capable to represent the relative displacement of the reference image with respect to the CAE model, although the latter one should be considered as first choice. The principle of these models is described in the following paragraphs, while the details about the mathematical modelling are let to reference [125][1]. Let us underline that the choice of the transformation model determines also the minimum number of features necessary to solve the identification problem. Hence, this minimal number of remarkable features should be taken into account when preparing the specimens: if the number of native features as corners is not enough, a certain number of artificial markers need to be added at known positions. Finally, let us observe that if the speckled painted on the surface was instead printed according to a fixed pattern (grid, regular spots, ...), the speckle itself could be used to solve the matching problem (in the same manner that the speckled is used to solve the correlation problem between images), providing a more accurate alignment of the coordinate systems.

Homography Homography is a planar transformation, associated to a non linear model, which maps a set of 2D coplanar points from the CAE model to a set of 2D points on the reference image, preserving straight lines. It requires at least 4 correspondences to estimate the parameters. Although the homography requires coplanar features, a possible workaround to manage axisymmetric geometries can consist in defining a virtual planar geometry associated to the original 3D one. Such a virtual geometry is defined as the projection of the 3D geometry on a plane, similarly to the DIC reference image which is the two dimensional projection of the considered specimen. However, the possible errors that might follow from this approximation have not been investigated.

Perspective-n-Point (PnP) Perspective-n-Point is a quasi-3D transformation, associated to a non linear model, which maps a set of 3D points from the CAE model to a set of 2D points on the reference image. It requires at least 3 correspondences to estimate the parameters. According to [125], it is probably the most suitable approach (flexible and accurate) to estimate the pose. However, in practice the estimation of the pose might not be satisfactory in two cases. The first one when the points along the thick direction are not clear on the reference image due to the quasi-perpendicular camera orientation (the PnP estimation is then not accurate). The second one when a set of coplanar features is selected on the CAE model rather than a three-dimensional set (the PnP model is then over-parametrized). Therefore, in such cases the homography relation provides a better estimation of the pose.

B.2 Uncertainty of the matching uncertainty

When the alignment procedure is based on the matching of features, the accuracy of the matching operation, denoted E, has an indirect influence on the accuracy of the identification via FEMU. In fact, an incorrect positioning of the mesh nodes leads to prescribe the wrong boundary conditions and leads to a non representative comparison with the experimental quantities. Therefore, an indicator the accuracy of the matching needs to be estimated. Supposing that the matching

[1]The implementations provided by the OpenCV library [21] are considered. See functions `findHomography` and `solvePnP` of OpenCV 3.2.0

position for a generic feature is located at the center of a specific pixel, the largest matching error is committed when the effective position of the feature is located on a corner of the pixel [109]. Hence, the matching error values at most half of the diagonal length of the pixel:

$$E = \pm \frac{1}{\sqrt{2}} \text{ pixel} \tag{B.1}$$

Actually, it might not be possible to locate the considered feature within a unique pixel because of the lack of sharpness of the image (see figure B.1).

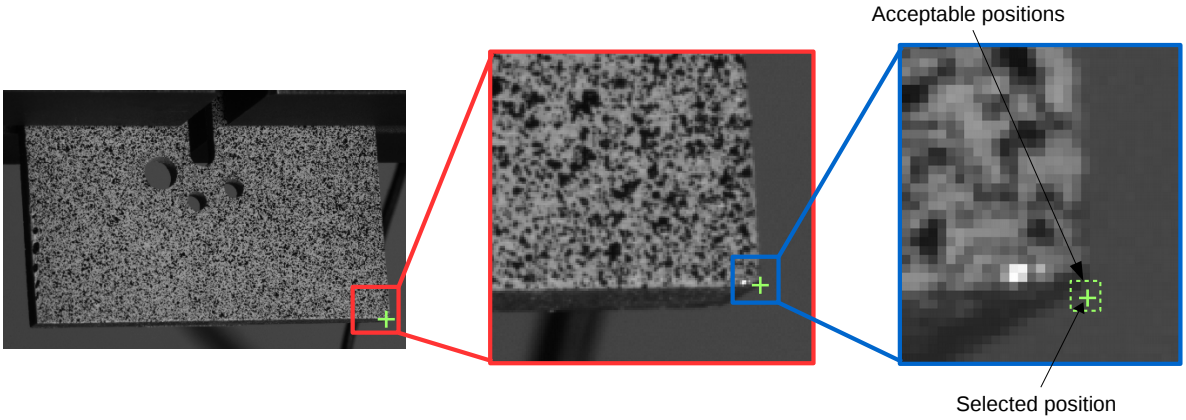

Figure B.1: Uncerntainty of the matching operation. Because of the lack of sharpness of the image, it might be difficult to locate the considered feature within a single pixel on the image.

In those cases, the matching error increases of a factor k:

$$E = \pm k \frac{1}{\sqrt{2}} \text{ pixel} \tag{B.2}$$

where k represents the minimum range of pixels within which is possible to locate the targeted feature. Such a value depends on the experimental set-up (camera orientation, illumination, etc.). In this work, a value $k = 3$ was considered as average value according to the recorded images.

Nevertheless, a proper evaluation of the matching error needs to be based on metrical quantities. Here, two different quantities are considered to define two error indicators: the resolution of the image and the gradient of the displacement field.

The resolution of the image, denoted r and expressed in terms of millimeter per pixel, defines the following error indicator:

$$E_1 = \pm k r \frac{1}{\sqrt{2}} \text{ mm} \tag{B.3}$$

which expresses how much the dimension of the geometry is altered by the matching uncertainty. In general, the resolution depends on external factors, as camera positioning and lighting of the room, so that the values of E_1 are generally constant for a common test equipment, as reported in table B.1. A practical criterion is to accept values of E_1 of the same order of magnitude than the dimensional tolerance prescribed for the machining of the specimen. Nevertheless, the value of E_1

needs to be evaluated with respect to the absolute size of the specimen. Let us also observe that the resolution of the image might not be constant over the entire surface for non-flat specimens.

The gradient of the displacement field, denoted $\nabla||u||$ and expressed in terms of millimeter per pixel[2], defines the following error indicator:

$$E_2 = \pm k \nabla ||u|| \frac{1}{\sqrt{2}} \text{ mm} \tag{B.4}$$

which expresses how much the matching operation affects the transferred values. The value of E_2 varies with respect to the considered geometry, as reported in table B.1. For a specific geometry, the value of E_2 varies with respect to the applied load. Moreover, two evaluations of E_2 are significant to evaluate the matching uncertainty. The first one is the maximum value assumed over the entire surface, denoted $E_{2,s}$, since within the FEMU algorithm, the matching errors propagate with a factor proportional to the local gradient of the displacement. The second one is the maximum value assumed over the zone where the measured displacement is prescribed as boundary condition, denoted $E_{2,bc}$. This latter value impacts directly the possibility of performing a simulation consistent with the experiment since it affects the boundary conditions. As an example, let us consider the Sandia 1 geometry which FE boundaries are located where displacement is not constant, with respect to the PAE2 geometry which FE boundaries are located where the displacement is quasi-constant (null gradient): the boundary conditions of the Sandia 1 geometry are clearly altered, as shown in table B.1.

Matching Error ($k = 3$)			
Test	E_1 [mm]	$E_{2,s}$ [mm]	$E_{2,bc}$ [mm]
PAE2-1	0.06	0.02	0.0025
Sandia1-2	0.06	0.036	0.019
Sandia2-1	0.06	0.025	0.003

Table B.1: Values of the matching uncertainties.

B.3 Values interpolation

The DIC results are transferred at the finite element nodes position using a bi-cubic spline interpolation of the full field map. The interpolation error is here assumed to be negligible since the pixel grid is, thanks to the dense result provided by FOLKI-D (1 value per pixel), much finer than finite element mesh. Let us note that the spline interpolation allows to extrapolate the measured values at the nodes located where DIC did not provide a result (*i.e.* edges and untextured zones).

Finally, an alternative, and probably more robust, approach would be to perform a transfer using the finite element shape functions. However, this approach has not been investigated in this study.

[2]The gradient is here calculated as the gradient of the DIC result with respect to the pixels of the image.

APPENDIX C

MINIMIZATION OF THE COST FUNCTION

The identification problem is solved as a minimization problem as:

$$\min_{\underline{\theta}} \psi(\underline{\theta}) \quad \text{with} \quad \underline{\theta}_{min} \leq \underline{\theta} \leq \underline{\theta}_{max} \tag{C.1}$$

where function $\psi(\underline{\theta})$ is here assumed of the particular form:

$$\psi(\underline{\theta}) = \frac{1}{2} \sum_j r_j^2(\underline{\theta}) \tag{C.2}$$

where vector $\underline{r}$ is a residual vector.

The bounds on the parameters are here considered as scalar values representing the minimum and maximum accepted values, forming an hypercube in the space of parameters. Such a problem is approached as a convex optimization problem [20]. In fact, the cost function is supposed to be locally convex over a convex set. Within this framework, the theory is consolidated and there exists a large variety of algorithms [20]. Part of the PhD work of Kleinermann [70] is focused on the comparison of minimization algorithms for parameter identification. They are compared based on the result of identification. The PhD work of Silva [121] also provides a review of the most used algorithms for parameter identification. Based on their remarks, two algorithms to solve our minimization problem have been selected in this study: the Nelder-Mead algorithm and the Levenberg-Marquardt algorithm. Both algorithms are natively formulated for unconstrained problems. Constraints on the parameter are really important for parameter identification in mechanics, since a non-physical parameter (*e.g.* a negative elastic modulus together with a positive yield stress) would lead to the impossibility to compute a finite element solution. Thus, a simple solution to impose bounds to unbounded algorithms consists in replacing the cost function by a pseudo-function which imposes a severe penalty when parameters are outside the bounds:

$$\psi(\underline{\theta}) = \begin{cases} \psi(\underline{\theta}) & \text{if} \quad \underline{\theta}_{min} \leq \underline{\theta} \leq \underline{\theta}_{max} \\ \psi' & \text{otherwise} \end{cases} \qquad \text{with} \quad \psi(\underline{\theta}) \ll \psi' \quad \forall \underline{\theta} \tag{C.3}$$

where Θ denotes the set of admissible parameters.

Nelder-Mead algorithm The Nelded-Mead algorithm [103] is a first order algorithm which is part of the simplex methods, a popular class of techniques for linear optimization. They are based on the hypothesis that the cost function might be approximated (locally) by a linear function. The solution is searched in a progressively decreasing domain (the simplex). The values assumed by the cost function at the vertex of the simplex are evaluated at each iteration. Afterwards, the simplex is then shrunk based on the rank of such values. The simplex methods are known to be robust, but their efficiency decreases with the number of unknowns. Nevertheless, these methods are derivative-free. Thus, the Nelder-Mead algorithm might be a convenient choice if the numerical computation of derivative cannot be trusted because of the experimental uncertainties.

Levenberg-Marquardt algorithm The Levenberg-Marquardt algorithm is a second order algorithm which is part of gradient-based methods. Supposing the objective functions as convex, the solution is given by the set of parameter for which the gradient is null. Proposed by Levenberg [82] and improved by Marquardt [94] later, this algorithm overcomes the conditioning issue of the Gauss-Newton algorithm. If the numerical derivative can be trusted, this algorithm should be the first choice as minimization technique. The considered update rule of the Levenberg-Marquardt algorithm reads:

$$\underline{\theta}_{i+1} = \underline{\theta}_i - \left[\underset{\sim}{J}^T(\underline{\theta}_i)\underset{\sim}{J}(\underline{\theta}_i) + \lambda \mathrm{diag}\left(\underset{\sim}{J}^T(\underline{\theta}_i)\underset{\sim}{J}(\underline{\theta}_i)\right)\right]^{-1} \nabla\psi(\underline{\theta}_i) \tag{C.4}$$

where λ is a scaling factor and $\underset{\sim}{J}$ is the Jacobian matrix of the residuals, which is here calculated by changing one factor at time the parameters, according to the forward finite difference formula:

$$J_{mn} = \frac{r_m(\theta_n + \delta\theta_n) - r_m(\theta_n)}{\delta\theta_n} \tag{C.5}$$

APPENDIX D

VALIDITY OF THE ASYMPTOTIC DEVELOPMENT

Let us recall the variational formulation of the mechanical problem with Robin boundary conditions:

$$a(\underset{\sim}{u}_{l_R}, \underset{\sim}{v}) + \frac{1}{l_R S_\Gamma} \int_\Gamma (\underset{\sim}{u}_{l_R} - \underset{\sim}{u}_b) \underset{\sim}{v} \, \mathrm{dS} = l(\underset{\sim}{v}) \tag{D.1}$$

where Γ is the portion of boundary $\partial\Omega$ where the Robin boundary condition is prescribed, $\underset{\sim}{v}$ is a test function, $l(\underset{\sim}{v})$ the work of the external forces, and $a(\underset{\sim}{u}_{l_R}, \underset{\sim}{v})$ a bilinear form. In the following, notation $\partial\Omega_D$ refers to the portion of boundary where a Dirichlet boundary condition is prescribed, while $\partial\Omega_N$ refers to the portion of boundary where a Neumann boundary condition is prescribed ($\partial\Omega \equiv \Gamma \cup \partial\Omega_N \cup \partial\Omega_D$). Let us recall also the asymptotic development of equation 3.20:

$$\underset{\sim}{u}_{l_R} = \underset{\sim}{u}_0 + l_R \underset{\sim}{u}_1 + l_R^2 \underset{\sim}{u}_2 + \cdots + l_R^n \underset{\sim}{u}_n \tag{D.2}$$

which is proposed (ansatz) as a possible approximation of $\underset{\sim}{u}_{l_R}$ around $l_R = 0$, assuming $\underset{\sim}{u}_0|_{\partial\Omega_D} = U_D$ and $\underset{\sim}{u}_i|_{\partial\Omega_D} = 0$ for $i \geq 1$. Since here l_R has a dimension, it means that the terms $\underset{\sim}{u}_i$ for $i \geq 1$ are not to be read as displacement components and no physical meaning should be found.

If it is possible to determine all the $\underset{\sim}{u}_n$ terms, the asymptotic development is an acceptable approximation of $\underset{\sim}{u}_{l_R}$ around $l_R = 0$.

The variational formulation of the Robin problem is approximated as:

$$\begin{aligned} \frac{1}{l_R S_\Gamma} \int_\Gamma (\underset{\sim}{u}_0 - \underset{\sim}{u}_b) \underset{\sim}{v} \, \mathrm{dS} + \left[a(\underset{\sim}{u}_0, \underset{\sim}{v}) + \frac{1}{S_\Gamma} \int_\Gamma \underset{\sim}{u}_1 \underset{\sim}{v} \, \mathrm{dS} \right] + \ \ldots \\ \ldots \ + l_R \left[a(\underset{\sim}{u}_1, \underset{\sim}{v}) + \frac{1}{S_\Gamma} \int_\Gamma \underset{\sim}{u}_2 \underset{\sim}{v} \, \mathrm{dS} \right] + l_R^2 a(\underset{\sim}{u}_2, \underset{\sim}{v}) + \ \cdots = l(\underset{\sim}{v}) \end{aligned} \tag{D.3}$$

which gives, by separating the terms according to the l_R exponents order, the following system of equations:

$$\text{(D.4)}\qquad \begin{cases} \frac{1}{l_R} : & \int_\Gamma (\underset{\sim}{u}_0 - \underset{\sim}{u}_b)\underset{\sim}{v}\,\mathrm{d}S = 0 & \forall \underset{\sim}{v} \in C(0) \text{ on } \partial\Omega_D \\ 0 : & a(\underset{\sim}{u}_0, \underset{\sim}{v}) + \frac{1}{S_\Gamma}\int_\Gamma \underset{\sim}{u}_1\underset{\sim}{v}\,\mathrm{d}S = l(\underset{\sim}{v}) & \forall \underset{\sim}{v} \in C(0) \text{ on } \partial\Omega_D \\ l_R : & a(\underset{\sim}{u}_1, \underset{\sim}{v}) + \frac{1}{S_\Gamma}\int_\Gamma \underset{\sim}{u}_2\underset{\sim}{v}\,\mathrm{d}S = 0 & \forall \underset{\sim}{v} \in C(0) \text{ on } \partial\Omega_D \\ & \vdots & \\ l_R^n : & a(\underset{\sim}{u}_n, \underset{\sim}{v}) + \frac{1}{S_\Gamma}\int_\Gamma \underset{\sim}{u}_{n+1}\underset{\sim}{v}\,\mathrm{d}S = 0 & \forall \underset{\sim}{v} \in C(0) \text{ on } \partial\Omega_D \end{cases}$$

where notation $C(0)$ is a set of the displacements kinematically admissible to zero. The first equation of the system gives:

$$\text{(D.5)}\qquad \underset{\sim}{u}_0|_\Gamma = \underset{\sim}{u}_b$$

Then, the second equation gives at first:

$$\text{(D.6)}\qquad a(\underset{\sim}{u}_0, \underset{\sim}{v}) = l(\underset{\sim}{v}) \qquad \forall v \in C(0) \text{ sur } \partial\Omega_D \cup \Gamma$$

considering a narrow set of test functions (*i.e.* kinematically admissible also on Γ). Knowing from the first equation that $\underset{\sim}{u}_0|_\Gamma = \underset{\sim}{u}_b$, this latter equation it implies that $\underset{\sim}{u}_0$ is the solution of the variational problem where $\underset{\sim}{u}_b$ is prescribed as Dirichlet boundary condition on Γ. Hence:

$$\text{(D.7)}\qquad a(\underset{\sim}{u}_0, \underset{\sim}{v}) = \int_{\partial\Omega_N \cup \Gamma} \left(\underset{\sim}{\underset{\sim}{\sigma}}(\underset{\sim}{u}_0)\cdot n\right)\underset{\sim}{v}\,\mathrm{d}S \qquad \forall \underset{\sim}{v} \in C(0) \text{ on } \partial\Omega_D$$

which, together with the second equation of the system gives:

$$\text{(D.8)}\qquad \int_\Gamma \left(\underset{\sim}{\underset{\sim}{\sigma}}(\underset{\sim}{u}_0)\cdot n\right)\underset{\sim}{v}\,\mathrm{d}S + \frac{1}{S_\Gamma}\int_\Gamma \underset{\sim}{u}_1\underset{\sim}{v}\,\mathrm{d}S = 0 \qquad \forall \underset{\sim}{v} \in C(0) \text{ on } \partial\Omega_D$$

Hence:

$$\text{(D.9)}\qquad \underset{\sim}{u}_1|_\Gamma = -S_\Gamma \underset{\sim}{\underset{\sim}{\sigma}}(\underset{\sim}{u}_0)|_\Gamma \cdot n$$

The third equation gives, at first:

$$\text{(D.10)}\qquad a(\underset{\sim}{u}_1, \underset{\sim}{v}) = 0 \qquad \forall \underset{\sim}{v} \in C(0) \text{ on } \partial\Omega_D \cup \Gamma$$

which implies (knowing $\underset{\sim}{u}_1|_\Gamma$ from the previous step) that $\underset{\sim}{u}_1$ is the solution to the variational problem where $\underset{\sim}{u}_1|_\Gamma$ is applied as Dirichlet boundary condition. Hence:

$$\text{(D.11)}\qquad a(\underset{\sim}{u}_1, \underset{\sim}{v}) = \int_\Gamma \left(\underset{\sim}{\underset{\sim}{\sigma}}(\underset{\sim}{u}_1)\cdot n\right)\underset{\sim}{v}\,\mathrm{d}S \qquad \forall \underset{\sim}{v} \in C(0) \text{ on } \partial\Omega_D$$

which gives, together with the third equation of the system:

$$\text{(D.12)}\qquad \underset{\sim}{u}_2|_\Gamma = -S_\Gamma \underset{\sim}{\underset{\sim}{\sigma}}(\underset{\sim}{u}_1)|_\Gamma \cdot n$$

At this point, applying the same mechanism (*i.e.* tightening and widening the set of test functions), it is possible to obtain all the terms of the asymptotic development:

$$\text{(D.13)}\qquad \underset{\sim}{u}_n|_\Gamma = -S_\Gamma \underset{\sim}{\underset{\sim}{\sigma}}(\underset{\sim}{u}_{n-1})|_\Gamma \cdot n$$

which proves its validity.

APPENDIX E

SENSITIVITY ANALYSIS

The sensitivity analysis represents in this work a basic step of parameter identification. It is used to estimate *a priori* the feasibility of the identification. A sensitivity analysis consists in quantifying the perturbation of the model's output (displacement and force for instance) produced by a variation of the model's inputs (material's parameters for instance). The identification of a certain parameter is here considered as feasible if a reasonable perturbation of the parameter induces a significant variation of force and displacement. A perturbation is here considered as reasonable if it is lower than 5%, while the variation of the output is considered as significant if it is at least equivalent to the uncertainty of the measurement system (*i.e.* approximatively ±200 N regarding the force and approximatively ±0.001 mm regarding the displacement[1]). Finally, let us underline that the sensitivity analysis is specific for each specimen, since both the geometry and the loading conditions play a role.

When performing a sensitivity analysis, the following situations might be met:

- a mutual influence of the parameters, if the output's variation produced by different parameters is located on the same zone of the specimen, at the same stage of loading. In that case, the possible effect of the variation of one parameter might be compensated by another parameter, leading to an indetermination of the identified values. Furthermore, in such a situation all the concurrent competing should be taken into account within the minimization (except if some of them have already been identified in a different manner or fixed at arbitrary values). This was the case of displacement with respect to the hardening parameters in the present study;

- an absence of sensitivity of a geometry with respect to a specific parameter. In this case, that parameter needs to be excluded from the identification on that geometry and be identified on a different geometry. Let us note that this case might be beneficial to simplify the identification of those parameters which would have a mutual influence on the output

[1] Although these values can be used to interpret all the sensitivity analyses of the present study, they might be, in general, different for each test. Indeed, the uncertainty of the load cell depends on its calibration and on the range of measurable values, while the uncertainty of the DIC measurements depends on the camera orientation and on the quality of the speckle on the surface.

of a different geometry. This was the case of force with respect to the Hosford exponent in the present study.

E.1 Methodology

Many factors should to be considered when performing a sensitivity analysis, as the computational cost or the non-linearities of the system [26]. Therefore, there exist as many techniques to perform the analysis. However, one of the simplest and most common approaches consists in changing one factor at a time (OAT) and to quantify the variation on the output. Such an approach is considered in this study because of its simplicity and because the same technique is used to calculate the Jacobian matrix of the identification problem, as described in appendix C. Table E.1 reports the reference set of parameters considered for all the sensitivity analysis presented here after. Each parameter was perturbed of +5%. The sensitivity analysis are presented in terms of

Reference parameters for the sensitivity analysis					
Plasticity					
R_0 [MPa]	Q_1 [MPa]	b_1	Q_2 [MPa]	b_2	n
460	62	315	2820	0.794	8
Damage					
f_c	f_r	k	p_s	c [N]	
0.05	0.15	0.5	0.5	40	

Table E.1: Reference parameters for the sensitivity analysis.

spatial fields for the displacement gap and in terms of force versus displacement of the machine for the force gap.

E.2 Results

The sensitivity analysis illustrated and discussed below, consider geometries CAE4 and PAE2 as representative of the axisymmetric and flat geometries respectively. At first, the sensitivity analysis is carried out on the plasticity parameters, which include the hardening parameters and the Hosford exponent, and then on the GTN parameters. Finally, the influence of regularization parameter of the non-local model is analysed.

E.2.1 Plasticity parameters

The first parameters analysed are the hardening parameters, denoted R_0, Q_1, b_1, Q_2, b_2. The sensitivity fields are evaluated both at the late stages of hardening, where the absolute value of displacement is maximum, and at the early stages of hardening, where the influence of parameters Q_1 and b_1 is more relevant.

The result at the late stages of hardening shows that parameters R_0, Q_2, b_2 have a significant influence on displacement, while Q_1 and b_1 have not, as visible in figures E.1 and E.2. The result at the early stages of hardening shows that parameters Q_1 and b_1 still have a negligible influence, as visible in figure E.3.. Furthermore, let us note that the influence of the hardening parameters is located on a common zone of the geometry. To not incur into an indetermination

of the parameters, the identification of the hardening coefficients was carried out omitting the displacements from the cost function.

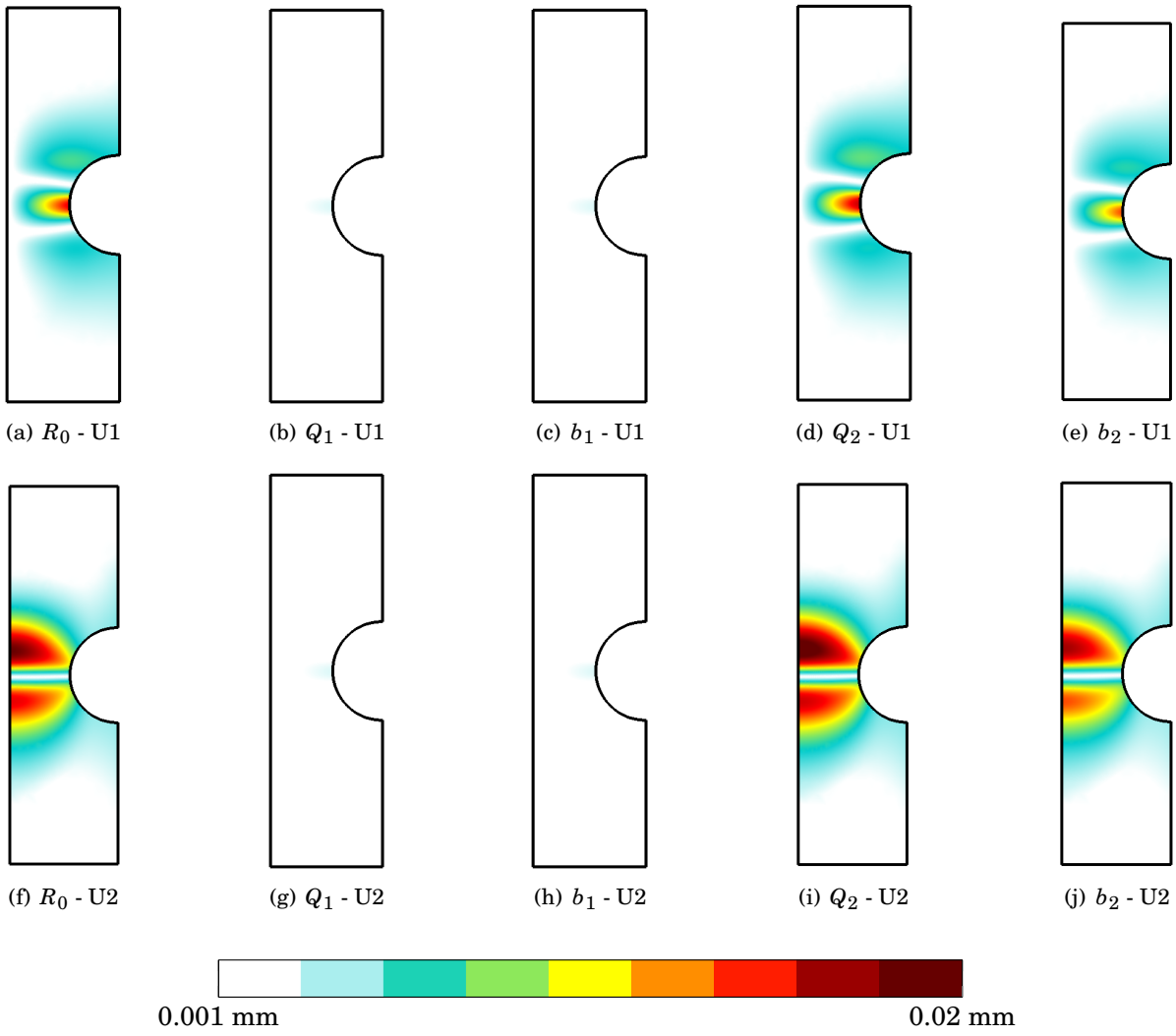

(a) R_0 - U1 (b) Q_1 - U1 (c) b_1 - U1 (d) Q_2 - U1 (e) b_2 - U1

(f) R_0 - U2 (g) Q_1 - U2 (h) b_1 - U2 (i) Q_2 - U2 (j) b_2 - U2

(k)

Figure E.1: Sensitivity of the horizontal (U_1) and vertical (U_2) displacement fields with respect to the hardening parameters on the CAE4 axisymmetric geometry. The boundary conditions are issued from test CAE4-2 (figure 1.10(c)). The displacement gap fields are shown at the late stages of hardening. It is possible to notice the influence of the parameters located on a common zone, which leads to an indetermination if solely the displacement gap is considered for the identification. Moreover, the sensitivity with respect to parameters Q_1 and b_1 is negligible at this loading stage.

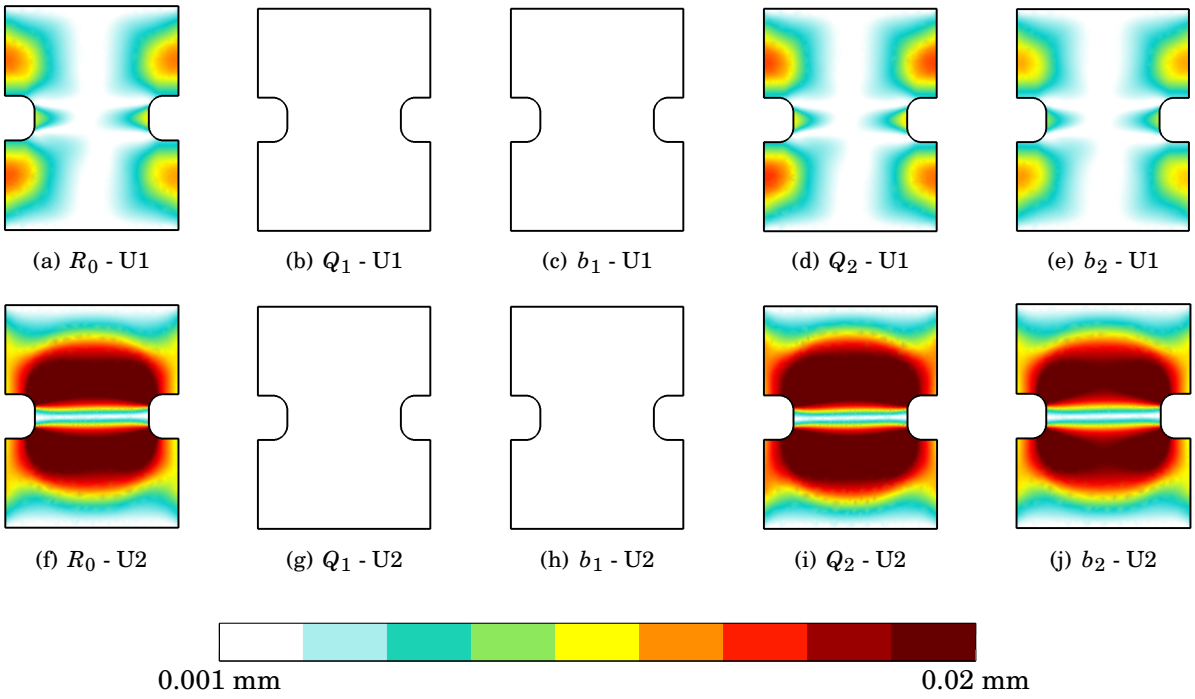

(a) R_0 - U1 (b) Q_1 - U1 (c) b_1 - U1 (d) Q_2 - U1 (e) b_2 - U1

(f) R_0 - U2 (g) Q_1 - U2 (h) b_1 - U2 (i) Q_2 - U2 (j) b_2 - U2

(k)

Figure E.2: Sensitivity of the horizontal (U_1) and vertical (U_2) displacement fields with respect to the hardening parameters on the PAE2 flat geometry. The boundary conditions are issued from test PAE2-1 (figure 1.11(c)). The displacement gap fields are shown at the late stages of hardening. It is possible to notice the influence of the parameters located on a common zone, which leads to an indetermination if solely the displacement gap is considered for the identification. Moreover, the sensitivity with respect to parameter b_1 is negligible at this loading stage.

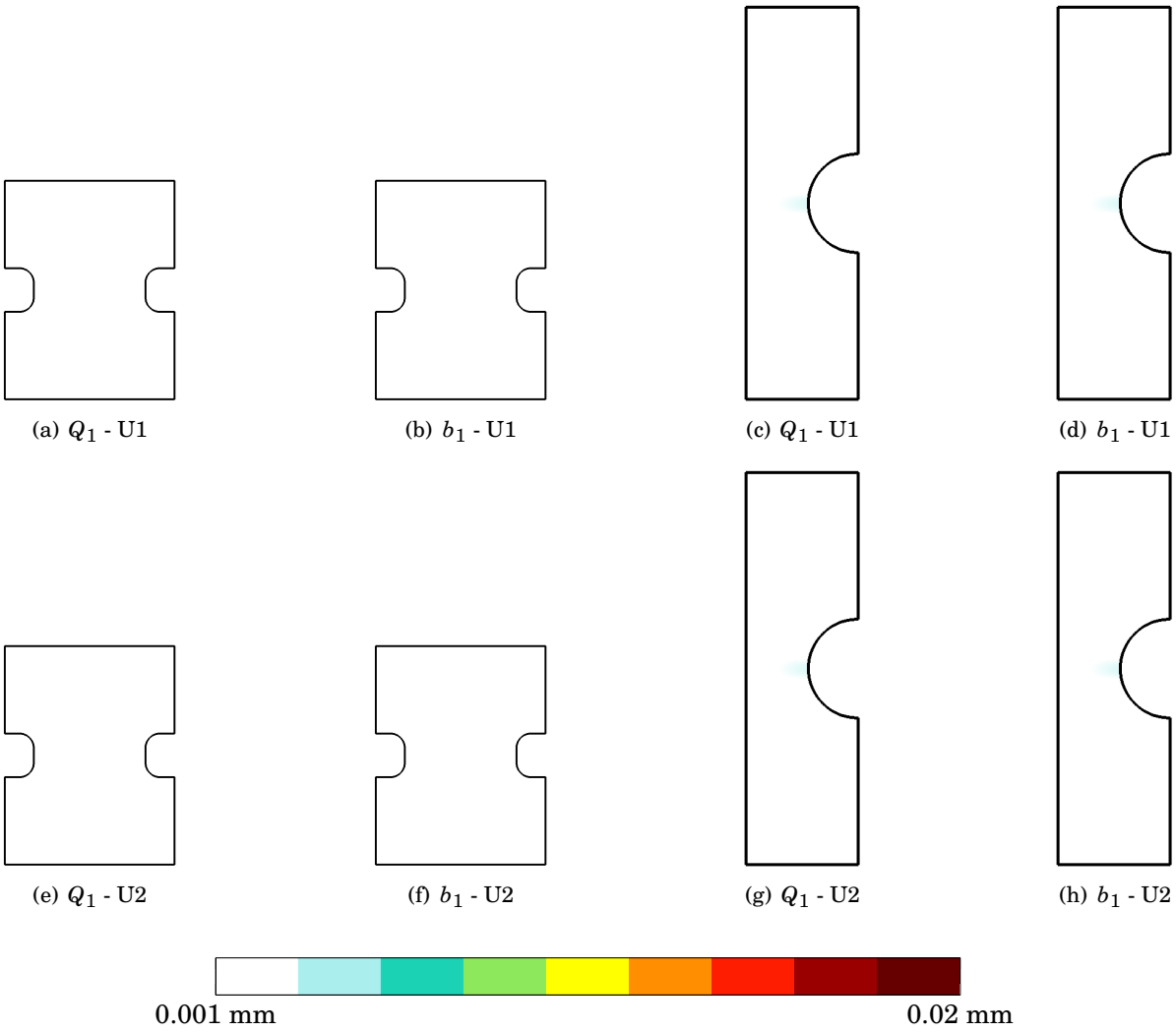

(a) Q_1 - U1 (b) b_1 - U1 (c) Q_1 - U1 (d) b_1 - U1

(e) Q_1 - U2 (f) b_1 - U2 (g) Q_1 - U2 (h) b_1 - U2

(i)

Figure E.3: Sensitivity of the horizontal (U_1) and vertical (U_2) displacement fields with respect to the hardening parameters Q_1 and b_1. The displacement gaps are evaluated at the early stages of hardening. The sensitivity is negligible also at this loading step.

The subsequent parameter which influence was analysed is the Hosford exponent. As figures E.4 and E.5 show, the influence of this parameter can be considered as negligible on the force for both geometries. Instead, the influence on displacement is significant for the flat geometries, especially along the transversal direction (with respect to the loading direction).

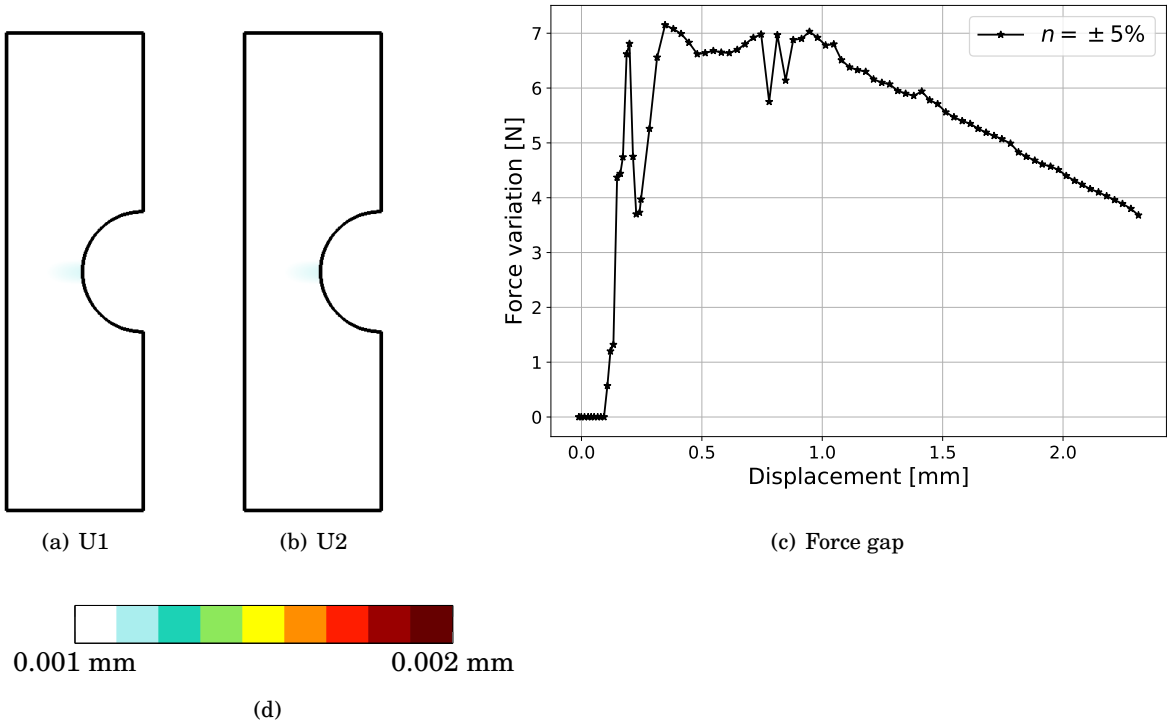

(a) U1 (b) U2 (c) Force gap

(d)

Figure E.4: Sensitivity of force and displacement fields (U_1, U_2) with respect to the Hosford exponent on the CAE4 axisymmetric geometry. The boundary conditions are issued from test CAE4-2 (figure 1.10(c)). The displacement gap fields are shown at the late stages of hardening, where the absolute values of displacement is the highest. The influence of the Hosford exponent is negligible both on force and displacement.

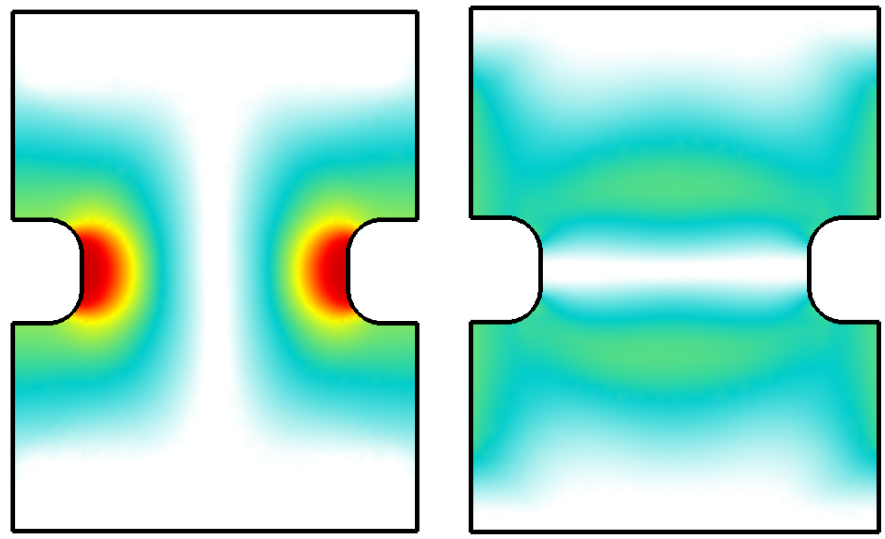

(a) U1 (b) U2

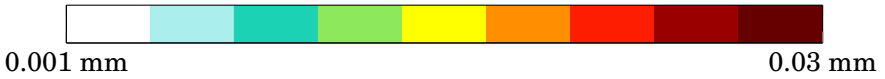

(c)

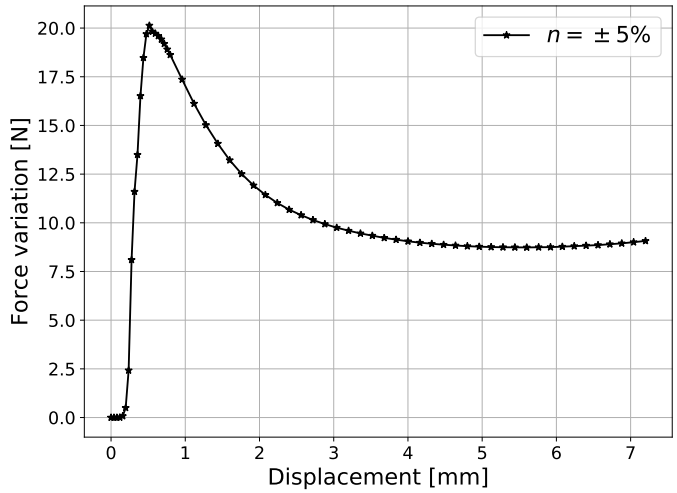

(d)

Figure E.5: Sensitivity of force and displacement fields (U_1, U_2) with respect to the Hosford exponent on the PAE2 flat geometry. The boundary conditions are issued from test PAE2-1 (figure 1.11(c)). The displacement gap fields are shown at the late stages of hardening, where the absolute values of displacement is the highest. The influence of the Hosford exponent on force is negligible, while the influence on displacement is considerable.

E.2.2 Damage parameters

The approach presented here above is now applied to evaluate the influence of the GTN model parameters. Solely the flat geometry is considered. The simulations are then run up to the onset of softening and the results are shown at the last converged loading step. The influence of all the GTN parameters is considerable on the displacement fields, as shown in figures E.6 and E.7. There is a clear concurrence between all the parameters on a common zone. Furthermore, the influence of the parameters governing void nucleation is higher compared to the remaining parameters, since the reference values are calibrated to reproduce a strong void growth.

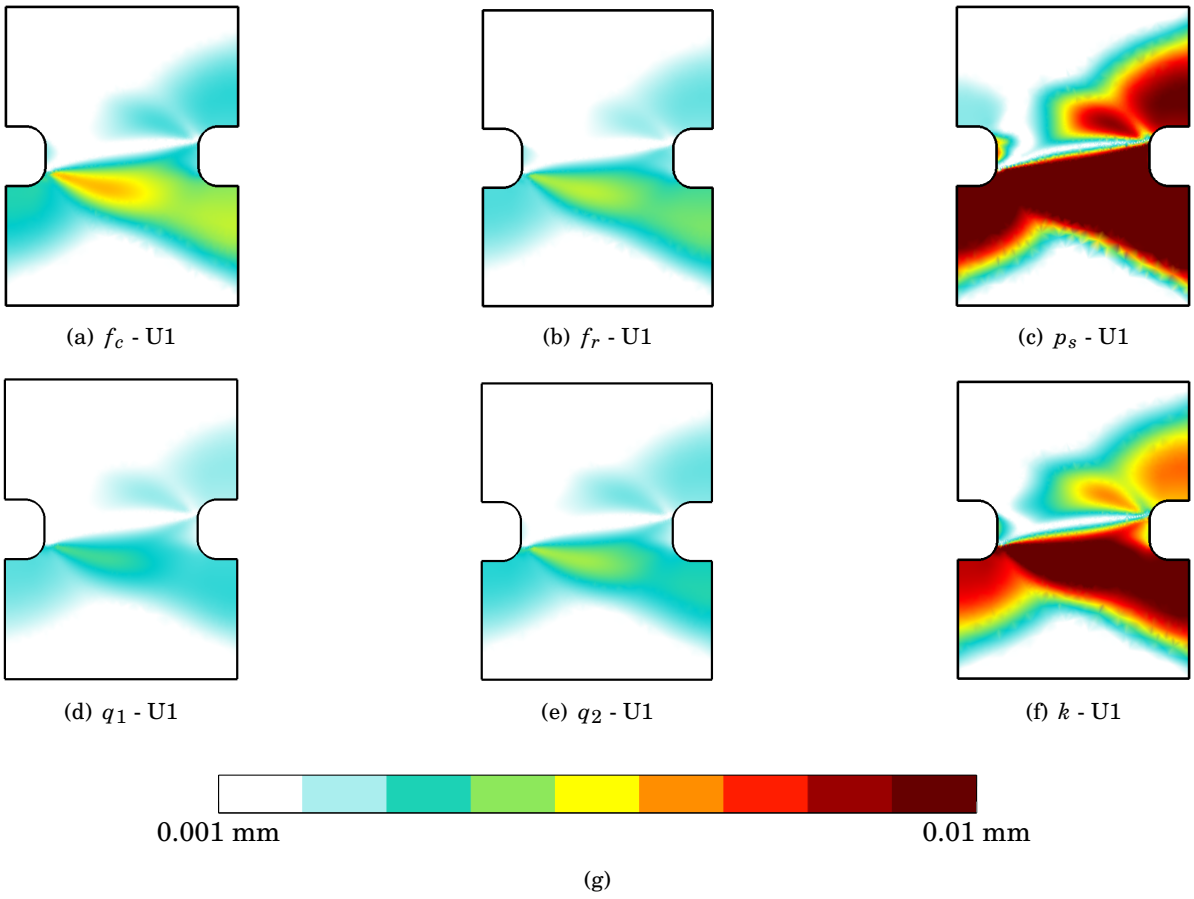

(a) f_c - U1 (b) f_r - U1 (c) p_s - U1

(d) q_1 - U1 (e) q_2 - U1 (f) k - U1

(g)

Figure E.6: Sensitivity of the horizontal (U_1) displacement field with respect to the damage parameters on the PAE2 flat geometry. The boundary conditions are issued from test PAE2-1. The displacement gap fields are shown at the onset of softening.

The same analysis can be applied for the sensitivity of the vertical field, as in figure E.7:

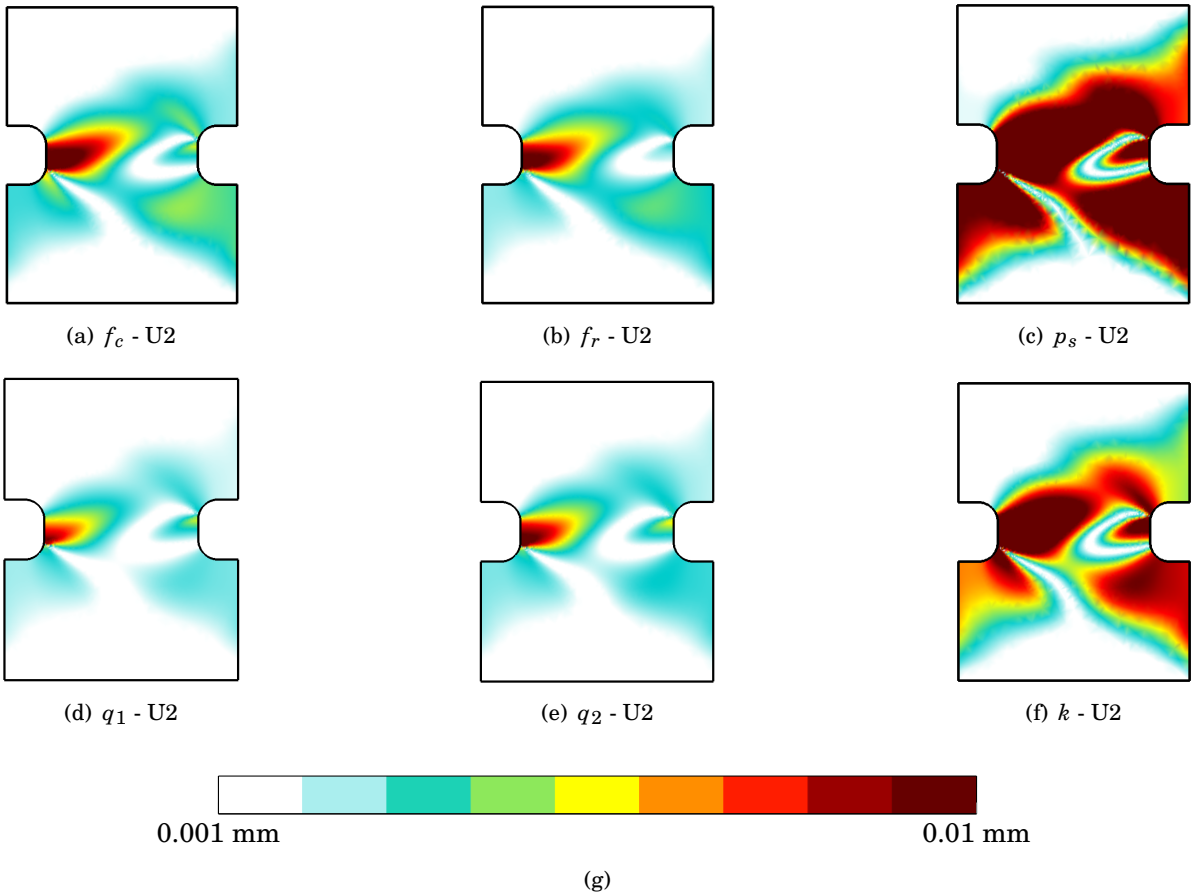

(a) f_c - U2 (b) f_r - U2 (c) p_s - U2

(d) q_1 - U2 (e) q_2 - U2 (f) k - U2

(g)

Figure E.7: Sensitivity of the vertical (U_2) displacement field with respect to the damage parameters on the PAE2 flat geometry. The boundary conditions are issued from test PAE2-1. The displacement gap fields are shown at the onset of softening.

Influence of the regularization parameter Although the role of the regularization parameter is to regularize the numerical model when softening occurs, its identification within the plastic regime was investigated since the regularization is made on the cumulated plasticity field, which starts developing before softening. The sensitivity analysis showed that the variation on force and displacement provoked by such a parameter (for the considered model, described in chapter 2) is not significant enough to be measured neither by the load cell nor the DIC system (see figure E.8).

Finally, let us observe that the vertical displacement field becomes sensitive with respect to the regularization parameter during the softening phase, as visible in figure E.9.

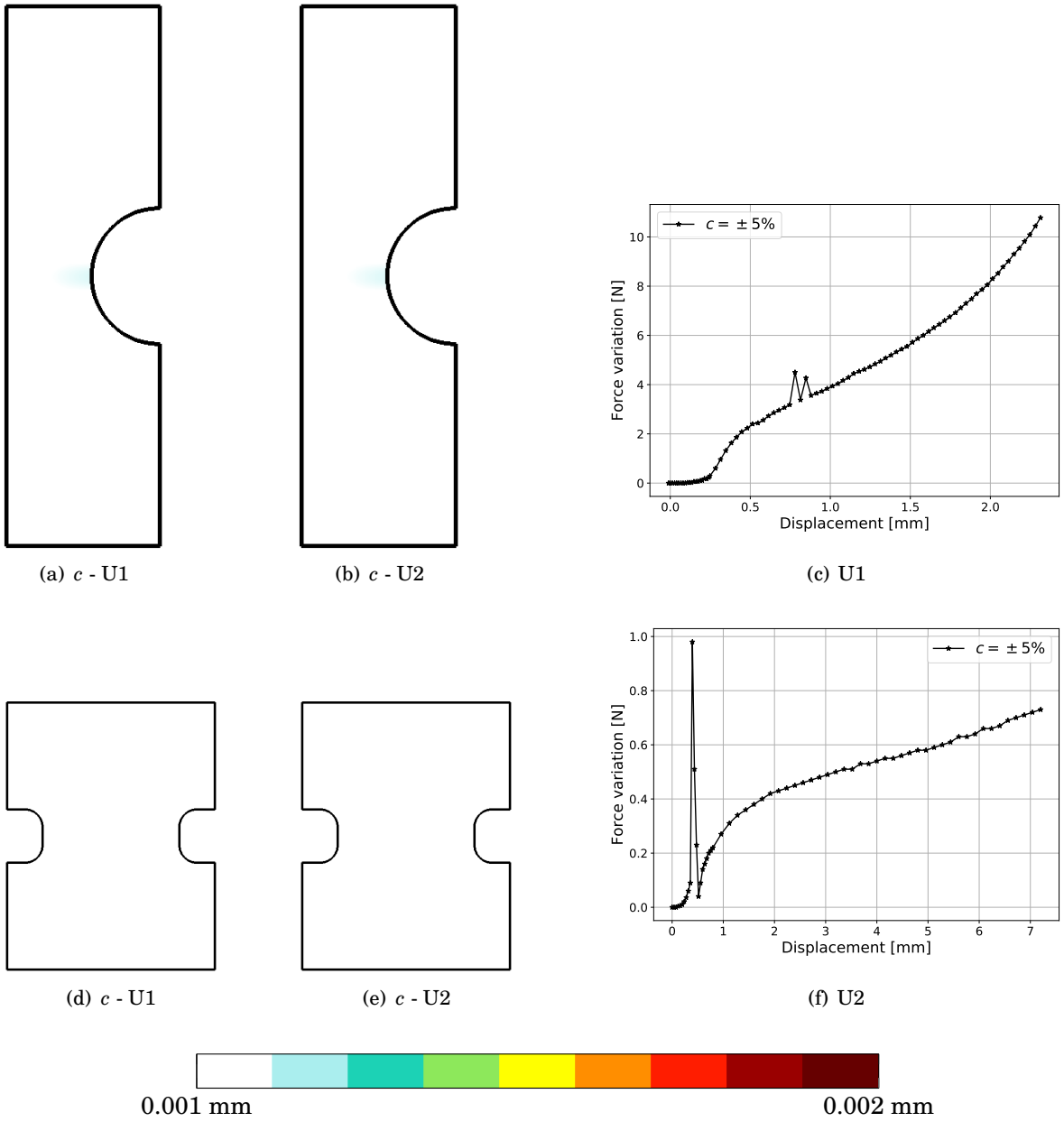

(a) c - U1 (b) c - U2 (c) U1

(d) c - U1 (e) c - U2 (f) U2

(g)

Figure E.8: Sensitivity of force and displacement fields (U_1, U_2) with respect to the regularization parameteron both axisymmetric (CAE4) and flat geometries (PAE2) within the plastic regime. The boundary conditions are issued from tests CAE4-2 and PAE2-1. The displacement gap fields are shown at the late stages of hardening, where the absolute values of displacement is the highest. The influence of the regularization parameter exponent is negligible both on force and displacement.

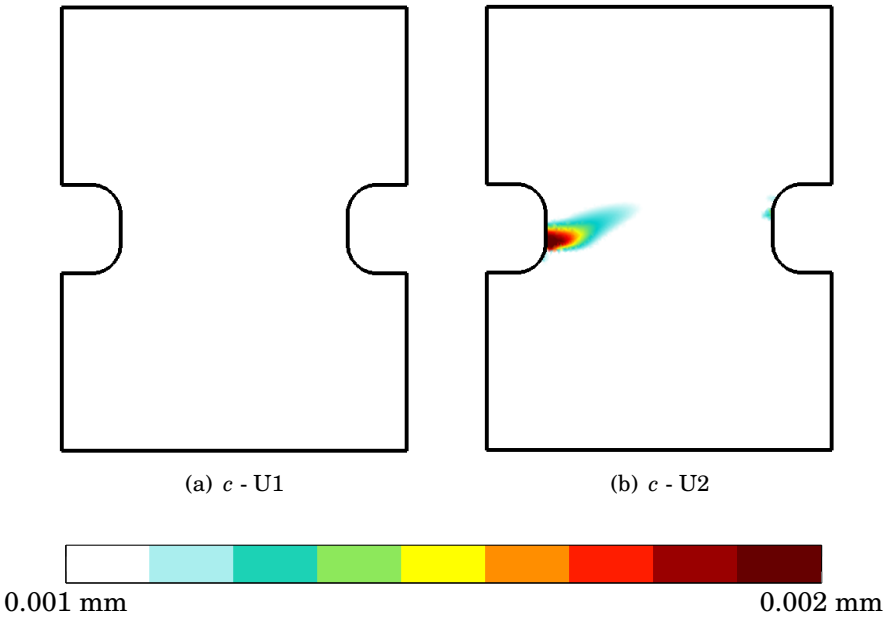

(a) c - U1 (b) c - U2

(c)

Figure E.9: Sensitivity of the displacement fields (U_1, U_2) with respect to the regularization parameter on the flat geometries (PAE2) within the softening (damage) phase.

BIBLIOGRAPHY

[1] *Alloy 625 data sheet*, tech. rep., Jacquet Metal Service.

[2] F. ABBASSI, T. BELHADJ, S. MISTOU, AND A. ZGHAL, *Parameter identification of a mechanical ductile damage using artificial neural networks in sheet metal forming*, Materials and Design, 45 (2013), pp. 605 – 615.

[3] E. AERO AND E. KUVSHINSKII, *Fundamental equations of the theory of elastic media with rotationally interacting particles*, Soviet Physics-Solid State, 2 (1960), pp. 1272–1281.

[4] F. AMIOT, F. HILD, AND J. ROGER, *Identification of elastic property and loading fields from full-field displacement measurements*, International Journal of Solids and Structures, 44 (2007), pp. 2863 – 2887.

[5] S. ANDRIEUX, T. N. BARANGER, AND A. BEN ABDA, *Solving cauchy problems by minimizing an energy-like functional*, Inverse Problems, 22 (2006), p. 115.

[6] S. AVRIL, M. BONNET, A.-S. BRETELLE, M. GRÉDIAC, F. HILD, P. IENNY, F. LATOURTE, D. LEMOSSE, S. PAGANO, E. PAGNACCO, AND F. PIERRON, *Overview of identification methods of mechanical parameters based on full-field measurements*, Experimental Mechanics, 48 (2008), pp. 381–402.

[7] S. AVRIL AND F. PIERRON, *General framework for the identification of constitutive parameters from full-field measurements in linear elasticity*, International Journal of Solids and Structures, 44 (2007), pp. 4978 – 5002.

[8] S. AVRIL, F. PIERRON, M. A. SUTTON, AND J. YAN, *Identification of elasto-visco-plastic parameters and characterization of lüders behavior using digital image correlation and the virtual fields method*, Mechanics of Materials, 40 (2008), pp. 729 – 742.

[9] I. BABUŠKA, *Error-bounds for finite element method*, Numerische Mathematik, 16 (1971), pp. 322–333.

[10] D. BANABIC, *Sheet Metal Forming Processes: Constitutive Modelling and Numerical Simulation*, Springer, 2010.

[11] Z. P. BAŽANT AND M. JIRÁSEK, *Nonlocal integral formulations of plasticity and damage: Survey of progress*, Journal of Engineering Mechanics, 128 (2002), pp. 1119–1149.

[12] A. BENALLAL AND V. TVERGAARD, *Nonlocal continuum effects on bifurcation in the plane strain tension-compression test*, Journal of the Mechanics and Physics of Solids, 43 (1995), pp. 741 – 770.

[13] N. BENSEDDIQ AND A. IMAD, *A ductile fracture analysis using a local damage model*, International Journal of Pressure Vessels and Piping, 85 (2008), pp. 219 – 227.

[14] J. BESSON, *Continuum models of ductile fracture: A review*, International Journal of Damage Mechanics, 19 (2010), pp. 3–52.

[15] J. BESSON, M. BLÉTRY, G. CAILLETAUD, J. CHABOCHE, AND S. FOREST, *Non-Linear Mechanics of Materials*, Solid Mechanics and Its Applications, Springer Netherlands, 2009.

[16] J. BLACK AND R. KOHSER, *DeGarmo's Materials and Processes in Manufacturing*, Wiley, 10th ed., 2010.

[17] M. BONNET AND A. CONSTANTINESCU, *Inverse problems in elasticity*, Inverse Problems, 21 (2005).

[18] B. L. BOYCE, S. L. B. KRAMER, T. R. BOSILJEVAC, E. CORONA, J. A. MOORE, K. ELKHODARY, C. H. M. SIMHA, B. W. WILLIAMS, A. R. CERRONE, A. NONN, J. D. HOCHHALTER, G. F. BOMARITO, J. E. WARNER, B. J. CARTER, D. H. WARNER, A. R. INGRAFFEA, T. ZHANG, X. FANG, J. LUA, V. CHIARUTTINI, M. MAZIÈRE, S. FELD-PAYET, V. A. YASTREBOV, J. BESSON, J.-L. CHABOCHE, J. LIAN, Y. DI, B. WU, D. NOVOKSHANOV, N. VAJRAGUPTA, P. KUCHARCZYK, V. BRINNEL, B. DÖBEREINER, S. MÜNSTERMANN, M. K. NEILSEN, K. DION, K. N. KARLSON, J. W. FOULK, A. A. BROWN, M. G. VEILLEUX, J. L. BIGNELL, S. E. SANBORN, C. A. JONES, P. D. MATTIE, K. PACK, T. WIERZBICKI, S.-W. CHI, S.-P. LIN, A. MAHDAVI, J. PREDAN, J. ZADRAVEC, A. J. GROSS, K. RAVI-CHANDAR, AND L. XUE, *The second sandia fracture challenge: predictions of ductile failure under quasi-static and moderate-rate dynamic loading*, International Journal of Fracture, 198 (2016), pp. 5–100.

[19] B. L. BOYCE, S. L. B. KRAMER, H. E. FANG, T. E. CORDOVA, M. K. NEILSEN, K. DION, A. K. KACZMAROWSKI, E. KARASZ, L. XUE, A. J. GROSS, A. GHAHREMANINEZHAD, K. RAVI-CHANDAR, S.-P. LIN, S.-W. CHI, J. S. CHEN, E. YREUX, M. RÜTER, D. QIAN, Z. ZHOU, S. BHAMARE, D. T. O'CONNOR, S. TANG, K. I. ELKHODARY, J. ZHAO, J. D. HOCHHALTER, A. R. CERRONE, A. R. INGRAFFEA, P. A. WAWRZYNEK, B. J. CARTER, J. M. EMERY, M. G. VEILLEUX, P. YANG, Y. GAN, X. ZHANG, Z. CHEN, E. MADENCI, B. KILIC, T. ZHANG, E. FANG, P. LIU, J. LUA, K. NAHSHON, M. MIRAGLIA, J. CRUCE, R. DEFRESE, E. T. MOYER, S. BRINCKMANN, L. QUINKERT, K. PACK, M. LUO, AND T. WIERZBICKI, *The sandia fracture challenge: blind round robin predictions of ductile tearing*, International Journal of Fracture, 186 (2014), pp. 5–68.

[20] S. BOYD AND L. VANDENBERGHE, *Convex Optimization*, Berichte über verteilte messysteme, Cambridge University Press, 2004.

[21] G. BRADSKI, *Opencv*, Dr. Dobb's Journal of Software Tools, (2000).

[22] F. BREZZI, *On the existence, uniqueness and approximation of saddle-point problems arising from lagrangian multipliers*, Revue française d'automatique, informatique, recherche opérationnelle. Analyse numérique, 8 (1974), pp. 129–151.

[23] G. B. BROGGIATO, F. CAMPANA, AND L. CORTESE, *Identification of material damage model parameters: an inverse approach using digital image processing*, Meccanica, 42 (2007), pp. 9–17.

[24] M. BRUNET, F. MORESTIN, AND H. WALTER, *Damage identification for anisotropic sheet-metals using a non-local damage model*, International Journal of Damage Mechanics, 13 (2004), pp. 35–57.

[25] L. BRUNO, G. FELICE, L. PAGNOTTA, A. POGGIALINI, AND G. STIGLIANO, *Elastic characterization of orthotropic plates of any shape via static testing*, International Journal of Solids and Structures, 45 (2008), pp. 908 – 920.

[26] D. G. CACUCI, M. IONESCU-BUJOR, AND I. M. NAVON, *Sensitivity and uncertainty analysis, volume II: applications to large-scale systems*, vol. 2, CRC press, 2005.

[27] H. CHALAL, S. AVRIL, F. PIERRON, AND F. MERAGHNI, *Experimental identification of a nonlinear model for composites using the grid technique coupled to the virtual fields method*, Composites Part A: Applied Science and Manufacturing, 37 (2006), pp. 315 – 325.

[28] F. CHAMPAGNAT, A. PLYER, G. LE BESNERAIS, B. LECLAIRE, S. DAVOUST, AND Y. LE SANT, *Fast and accurate piv computation using highly parallel iterative correlation maximization*, Experiments in Fluids, 50 (2011), p. 1169.

[29] A. CIMETIÈRE, F. DELVARE, M. JAOUA, AND F. PONS, *Solution of the cauchy problem using iterated tikhonov regularization*, Inverse Problems, 17 (2001), p. 553.

[30] D. CLAIRE, F. HILD, AND S. ROUX, *A finite element formulation to identify damage fields: the equilibrium gap method*, International journal for numerical methods in engineering, 61 (2004), pp. 189–208.

[31] S. COOREMAN, *Identification of the plastic material behaviour through full- field displacement measurements and inverse methods*, PhD thesis, Vrije Universitet Brussel, 2008.

[32] E. COSSERAT AND F. COSSERAT, *Théorie Des Corps Déformables*, Hermann et fils, 1909.

[33] N. COTTIN, H. P. FELGENHAUER, AND H. G. NATKE, *On the parameter identification of elastomechanical systems using input and output residuals*, Ingenieur-Archiv, 54 (1984), pp. 378–387.

[34] L. CROUZEIX, J. N. PÉRIÉ, F. COLLOMBET, AND B. DOUCHIN, *An orthotropic variant of the equilibrium gap method applied to the analysis of a biaxial test on a composite material*, Composites Part A: Applied Science and Manufacturing, 40 (2009), pp. 1732 – 1740.

[35] S. CUVILLIEZ, *Passage d'un modèle d'endommagement continu régularisé à un modèle de fissuration cohésive dans le cadre de la rupture quasi-fragile*, PhD thesis, École Nationale Supérieure des Mines de Paris, 2012.

[36] A. DOGUI AND F. SIDOROFF, *Rhéologie anisotrope en grandes déformations*, in Rhéologie des matériaux anisotropes, 1986, pp. 69–78.

[37] J. DOURNAUX, S. BOUVIER, A. AOUAFI, AND P. VACHER, *Full-field measurement technique and its application to the analysis of materials behaviour under plane strain mode*, Materials Science and Engineering: A, 500 (2009), pp. 47 – 62.

[38] D. DRUCKER, *A definition of stable inelastic material*, ASME Journal of Applied Mechanics, 26 (1959), pp. 101 – 195.

[39] A. L. EDWARD, *The invention and definition of alloy 625*, The Mineral, Metals and Materials Society, (1991).

[40] R. A. ENGELEN, M. G. GEERS, AND F. P. BAAIJENS, *Nonlocal implicit gradient-enhanced elasto-plasticity for the modelling of softening behaviour*, International Journal of Plasticity, 19 (2003), pp. 403 – 433.

[41] J. FALESKOG, X. GAO, AND C. F. SHIH, *Cell model for nonlinear fracture analysis – i. micromechanics calibration*, International Journal of Fracture, (1998).

[42] C. FARHAT AND F. M. HEMEZ, *Updating finite element dynamic models using an element-by-element sensitivity methodology*, AIAA journal, 31 (1993).

[43] R. FEDELE, B. RAKA, F. HILD, AND S. ROUX, *Identification of adhesive properties in glare assemblies using digital image correlation*, Journal of the Mechanics and Physics of Solids, 57 (2009), pp. 1003 – 1016.

[44] S. FELD-PAYET, *Amorçage et propagation de fissures dans les milieux ductiles non locaux*, PhD thesis, École Nationale Supérieure des Mines de Paris, 2010.

[45] M. A. FISCHLER AND R. C. BOLLES, *Random sample consensus: A paradigm for model fitting with applications to image analysis and automated cartography*, Commun. ACM, 24 (1981), pp. 381–395.

[46] E. FLORENTIN AND G. LUBINEAU, *Using constitutive equation gap method for identification of elastic material parameters: technical insights and illustrations*, International Journal on Interactive Design and Manufacturing (IJIDeM), 5 (2011), pp. 227–234.

[47] S. FOREST, *Micromorphic approach for gradient elasticity, viscoplasticity, and damage*, Journal of Engineering Mechanics, 135 (2009), pp. 117–131.

[48] X. GAO, J. FALESKOG, C. SHIH, AND R. DODDS, *Ductile tearing in part-through cracks: experiments and cell-model predictions*, Engineering Fracture Mechanics, 59 (1998), pp. 761 – 777.

[49] N. GERMAIN, *Modélisation non locale de l'endommagement dans les structure composites*, PhD thesis, 2006.

[50] M. GOLOGANU, J.-B. LEBLOND, AND J. DEVAUX, *Approximate models for ductile metals containing non-spherical voids—case of axisymmetric prolate ellipsoidal cavities*, Journal of the Mechanics and Physics of Solids, 41 (1993), pp. 1723 – 1754.

[51] M. GREDIAC AND F. HILD, *Full-Field Measurements and Identification in Solid Mechanics*, ISTE, Wiley, 2012.

[52] M. GRÉDIAC, F. PIERRON, AND Y. SURREL, *Novel procedure for complete in-plane composite characterization using a single t-shaped specimen*, Experimental Mechanics, 39 (1999), pp. 142–149.

[53] M. GRÉDIAC, *Principe des travaux virtuels et identification*, in Comptes rendus de l'académie des sciences, vol. 309, 1989, pp. 1–5.

[54] M. GRÉDIAC, *The use of full-field measurement methods in composite material characterization: interest and limitations*, Composites Part A: Applied Science and Manufacturing, 35 (2004), pp. 751 – 761.

[55] M. GRÉDIAC, E. TOUSSAINT, AND F. PIERRON, *Special virtual fields for the direct determination of material parameters with the virtual fields method. 1–principle and definition*, International Journal of Solids and Structures, 39 (2002), pp. 2691 – 2705.

[56] ——, *Special virtual fields for the direct determination of material parameters with the virtual fields method. 3–application to the bending rigidities of anisotropic plates*, International Journal of Solids and Structures, 40 (2003), pp. 2401 – 2419.

[57] A. L. GURSON, *Continuum theory of ductile rupture by void nucleation and growth: Part i—yield criteria and flow rules for porous ductile media*, Journal of Engineering Materials and Technology, 99 (1977), pp. 2–15.

[58] K. GUSTAFSON, *Domain decomposition, operator trigonometry, robin condition*, Contemporary Mathematics, 218 (1998), pp. 432–437.

[59] J. HADAMARD, *Le problème de Cauchy et les équations aux dérivées partielles linéaires hyperboliques: leçons professées à l'Université Yale*, Hermann et cie, 1932.

[60] H. HADDADI AND S. BELHABIB, *Improving the characterization of a hardening law using digital image correlation over an enhanced heterogeneous tensile test*, International Journal of Mechanical Sciences, 62 (2012), pp. 47 – 56.

[61] E. HERIPRE, M. DEXET, J. CREPIN, L. GELEBART, A. ROOS, M. BORNERT, AND D. CALDEMAISON, *Coupling between experimental measurements and polycrystal finite element calculations for micromechanical study of metallic materials*, International Journal of Plasticity, 23 (2007), pp. 1512–1539.

[62] F. HILD, A. BOUTERF, L. CHAMOIN, H. LECLERC, F. MATHIEU, J. NEGGERS, F. PLED, Z. TOMIČEVIĆ, AND S. ROUX, *Toward 4d mechanical correlation*, Advanced Modeling and Simulation in Engineering Sciences, 3 (2016), p. 17.

[63] R. HILL, *A general theory of uniqueness and stability in elastic-plastic solids*, Journal of the Mechanics and Physics of Solids, 6 (1958), pp. 236 – 249.

[64] W. F. HOSFORD, *A generalized isotropic yield criterion*, ASME Journal of Applied Mechanics, 39 (1972), pp. 607–609.

[65] J. W. HUTCHINSON, *Fundamentals of the phenomenological theory of nonlinear fracture mechanics*, Journal of Applied Mechanics, 50 (1983), pp. 1042–1051.

[66] L. KACHANOV, *Time of the rupture process under creep conditions*, Izvestiya Akademii Nauk SSSR, 8 (1958), pp. 26–31.

[67] J. KAJBERG AND G. LINDKVIST, *Characterisation of materials subjected to large strains by inverse modelling based on in-plane displacement fields*, International Journal of Solids and Structures, 41 (2004), pp. 3439 – 3459.

[68] J. KAJBERG AND B. WIKMAN, *Viscoplastic parameter estimation by high strain-rate experiments and inverse modelling – speckle measurements and high-speed photography*, International Journal of Solids and Structures, 44 (2007), pp. 145 – 164.

[69] P. KELLY, *Solid Mechanics Lecture Notes*, The University of Auckland, 2013.

[70] J. KLEINERMANN, *Identification paramétrique et optimisation des procédés de mise à forme par problèmes inverses*, PhD thesis, University of Liege, Liege, Belgium, 2000.

[71] V. KOZÁK AND L. VLČEK, *Parameters identification for gtn model and their verification on 42crmo4 steel*, in Materials Science Forum, vol. 482, Trans Tech Publ, 2005, pp. 335–338.

[72] E. KRÖNER, *Elasticity theory of materials with long range cohesive forces*, International Journal of Solids and Structures, 3 (1967), pp. 731–742.

[73] P. LADEVÈZE, N. MOËS, AND B. DOUCHIN, *Constitutive relation error estimators for (visco)plastic finite element analysis with softening*, Computer Methods in Applied Mechanics and Engineering, 176 (1999), pp. 247 – 264.

[74] W. LAI, D. RUBIN, D. RUBIN, AND E. KREMPL, *Introduction to Continuum Mechanics*, Elsevier Science, 2009.

[75] G. LE BESNERAIS AND F. CHAMPAGNAT, *Dense optical flow by iterative local window registration*, IEEE, 2005, pp. 137–140.

[76] G. LE BESNERAIS, Y. LE SANT, AND D. LÉVÊQUE, *Fast and dense 2d and 3d displacement field estimation by a highly parallel image correlation algorithm*, Strain, 52 (2016), pp. 286–306.

[77] Y. LE SANT, B. DELÉGLISE, AND Y. MEBARKI, *An automatic image alignment method applied to pressure sensitive paint measurements*, in Instrumentation in Aerospace Simulation Facilities, 1997. ICIASF'97 Record., International Congress on, IEEE, 1997, pp. 57–65.

[78] Y. LE SANT, V. TODOROFF, A. BERNARD-BRUNEL, G. LE BESNERAIS, F. MICHELI, AND D. DONJAT, *Multi-camera calibration for 3dbos*, in 17th international symposium on applications of laser techniques to fluid mechanics, 2014.

[79] D. LECOMPTE, A. SMITS, H. SOL, J. VANTOMME, AND D. VAN HEMELRIJCK, *Mixed numerical–experimental technique for orthotropic parameter identification using biaxial tensile tests on cruciform specimens*, International Journal of Solids and Structures, 44 (2007), pp. 1643 – 1656.

[80] E. H. LEE, *Elastic-plastic deformation at finite strains*, Journal of Applied Mechanics, 36 (1969), pp. 1–6.

[81] J. LEMAITRE AND J. CHABOCHE, *Mechanics of Solid Materials*, Cambridge University Press, 1994.

[82] K. LEVENBERG, *A method for the solution of certain non-linear problems in least squares*, Quarterly of applied mathematics, 2 (1944), pp. 164–168.

[83] D. LEVIN, *The approximation power of moving least squares*, Mathematics of Computation, 67 (1998), pp. 1517–1531.

[84] H. LI, M. FU, J. LU, AND H. YANG, *Ductile fracture: Experiments and computations*, International Journal of Plasticity, 27 (2011), pp. 147 – 180.

[85] E. LORENTZ, *Constitutive relations with gradients of internal variables : derivation, variational formulation and numerical setting*, PhD thesis, Université Pierre et Marie Curie - Paris VI, 1999.

[86] E. LORENTZ AND S. ANDRIEUX, *Analysis of non-local models through energetic formulations*, International Journal of Solids and Structures, 40 (2003), pp. 2905–2936.

[87] E. LORENTZ AND A. BENALLAL, *Gradient constitutive relations: numerical aspects and application to gradient damage*, Computer Methods in Applied Mechanics and Engineering, 194 (2005), pp. 5191 – 5220.

[88] E. LORENTZ AND V. GODARD, *Gradient damage models: Toward full-scale computations*, Computer Methods in Applied Mechanics and Engineering, 200 (2011), pp. 1927–1944.

[89] J. LUBLINER, *Plasticity Theory*, Dover Publications, 2008.

[90] R. MAHNKEN, *Aspects on the finite-element implementation of the gurson model including parameter identification*, International Journal of Plasticity, 15 (1999), pp. 1111 – 1137.

[91] ——, *A comprehensive study of a multiplicative elastoplasticity model coupled to damage including parameter identification*, Computers and Structures, 74 (2000), pp. 179 – 200.

[92] R. MAHNKEN AND E. STEIN, *Parameter identification for finite deformation elasto-plasticity in principal directions*, Computer Methods in Applied Mechanics and Engineering, 147 (1997), pp. 17 – 39.

[93] E. MARKIEWICZ, P. DUCROCQ, AND P. DRAZETIC, *An inverse approach to determine the constitutive model parameters from axial crushing of thin-walled square tubes*, International Journal of Impact Engineering, 21 (1998), pp. 433 – 449.

[94] D. W. MARQUARDT, *An algorithm for least-squares estimation of nonlinear parameters*, Journal of the society for Industrial and Applied Mathematics, 11 (1963), pp. 431–441.

[95] B. MAX, *Comportement mécanique et couplage mécanique-oxydation dans l'alliage 718: effet des éléments en solution solide*, PhD thesis, 2014.

[96] M. MEUWISSEN, C. OOMENS, F. BAAIJENS, R. PETTERSON, AND J. JANSSEN, *Determination of the elasto-plastic properties of aluminium using a mixed numerical–experimental method*, Journal of Materials Processing Technology, 75 (1998), pp. 204 – 211.

[97] M. M. MEUWISSEN, *An inverse method for the mechanical characterisation of metals*, PhD thesis, Technische Universiteit Eindhoven, 1998.

[98] C. MIEHE, N. APEL, AND M. LAMBRECHT, *Anisotropic additive plasticity in the logarithmic strain space: modular kinematic formulation and implementation based on incremental minimization principles for standard materials*, Computer Methods in Applied Mechanics and Engineering, 191 (2002), pp. 5383 – 5425.

[99] R. V. MISES, *Mechanik der festen körper im plastisch- deformablen zustand*, Nachrichten von der Gesellschaft der Wissenschaften zu Göttingen, Mathematisch-Physikalische Klasse, (1913), pp. 582–592.

[100] V. A. MOROZOV, *On the solution of functional equations by the method of regularization*, Soviet Mathematics Doklady, 7 (1966), p. 414 – 417.

[101] N. MOËS, C. STOLZ, P.-E. BERNARD, AND N. CHEVAUGEON, *A level set based model for damage growth: The thick level set approach*, International Journal for Numerical Methods in Engineering, 86 (2011), pp. 358–380.

[102] S. MURAKAMI, *Continuum Damage Mechanics: A Continuum Mechanics Approach to the Analysis of Damage and Fracture*, Solid Mechanics and Its Applications, Springer Netherlands, 2012.

[103] J. A. NELDER AND R. MEAD, *A simplex method for function minimization*, The computer journal, 7 (1965), pp. 308–313.

[104] D. NOTTA-CUVIER, B. LANGRAND, F. LAURO, AND E. MARKIEWICZ, *An innovative procedure for characterising a coupled elastoplastic damage model of behaviour using the virtual fields method*, International Journal of Solids and Structures, 69–70 (2015), pp. 415 – 427.

[105] B. PAN, K. QIAN, H. XIE, AND A. ASUNDI, *Two-dimensional digital image correlation for in-plane displacement and strain measurement: a review*, Measurement Science and Technology, 20 (2009).

[106] P. PAPADOPOULOS AND J. LU, *A general framework for the numerical solution of problems in finite elasto-plasticity*, Computer Methods in Applied Mechanics and Engineering, 159 (1998), pp. 1 – 18.

[107] R. H. J. PEERLINGS, R. DE BORST, W. A. M. BREKELMANS, AND J. H. P. DE VREE, *Gradient enhanced damage for quasi-brittle materials*, International Journal for Numerical Methods in Engineering, 39 (1996), pp. 3391–3403.

[108] G. PERRIN AND J. LEBLOND, *Analytical study of a hollow sphere made of plastic porous material and subjected to hydrostatic tension-application to some problems in ductile fracture of metals*, International Journal of Plasticity, 6 (1990), pp. 677 – 699.

[109] T. POTTIER, *Constitutive parameter identification using finite element updating method associated with kinematic and thermal full field measurements*, PhD thesis, Université de Savoie, 2010.

[110] J. N. PÉRIÉ, H. LECLERC, S. ROUX, AND F. HILD, *Digital image correlation and biaxial test on composite material for anisotropic damage law identification*, International Journal of Solids and Structures, 46 (2009), pp. 2388 – 2396.

[111] Y. RABOTNOV, *Creep problems in structural members*, North Holland, (1969).

[112] J. RICE, *A path independent integral and the approximate analysis of strain concentration by notches and cracks*, Journal of Applied Mechanics, 35 (1968), pp. 379–386.

[113] J. RICE AND J. RUDNICKI, *A note on some features of the theory of localization of deformation*, International Journal of solids and structures, 16 (1980), pp. 597–605.

[114] J. R. RICE AND D. M. TRACEY, *On the ductile enlargement of voids in triaxial stress fields*, Journal of Mechanics Physics of Solids, 17 (1969), pp. 201–217.

[115] L. ROBERT, V. VELAY, N. DECULTOT, AND S. RAMDE, *Identification of hardening parameters using finite element models and full-field measurements: some case studies*, The Journal of Strain Analysis for Engineering Design, 47 (2012), pp. 3–17.

[116] D. ROGULA, *Nonlocal Theory of Material Media*, CISM International Centre for Mechanical Sciences, Springer Vienna, 2014.

[117] G. ROUSSELIER, *Ductile fracture models and their potential in local approach of fracture*, Nuclear Engineering and Design, 105 (1987), pp. 97 – 111.

[118] C. RUNGE, *Über empirische funktionen und die interpolation zwischen äquidistanten ordinaten*, Zeitschrift für Mathematik und Physik, 46 (1901), pp. 224–243.

[119] V. SHANKAR, K. B. SANKARA RAO, AND S. MANNAN, *Microstructure and mechanical properties of inconel 625 superalloy*, Journal of Nuclear Materials, 288 (2001), pp. 222 – 232.

[120] A. SHUTOV AND J. IHLEMANN, *Analysis of some basic approaches to finite strain elastoplasticity in view of reference change*, International Journal of Plasticity, 63 (2014), pp. 183 – 197.

[121] G. SILVA, *Identification of material properties using finite elements and full-field measurements with focus on the characterization of deterministic experimental errors*, PhD thesis, Ph. D. Thesis, Ecole des Mines de Saint Etienne, France, 2009.

[122] K. SPRANGHERS, I. VASILAKOS, D. LECOMPTE, H. SOL, AND J. VANTOMME, *Identification of the plastic behavior of aluminum plates under free air explosions using inverse methods and full-field measurements*, International Journal of Solids and Structures, 51 (2014), pp. 210–226.

[123] M. SPRINGMANN AND M. KUNA, *Identification of material parameters of the gurson–tvergaard–needleman model by combined experimental and numerical techniques*, Computational Materials Science, 32 (2005), pp. 544 – 552.

[124] ——, *Determination of ductile damage parameters by local deformation fields: Measurement and simulation*, Archive of Applied Mechanics, 75 (2006), p. 775.

[125] R. SZELISKI, *Computer Vision: Algorithms and Applications*, Texts in Computer Science, Springer London, 2010.

[126] B. TANGUY, T. LUU, G. PERRIN, A. PINEAU, AND J. BESSON, *Plastic and damage behaviour of a high strength {X100} pipeline steel: Experiments and modelling*, International Journal of Pressure Vessels and Piping, 85 (2008), pp. 322 – 335.

[127] A. TIKHONOV AND V. ARSENIN, *Solutions of ill-posed problems*, Scripta series in mathematics, Winston, 1977.

[128] S. TIMOSHENKO, *Theory of Elasticity*, Engineering societies monographs, McGraw-Hill, 1934.

[129] E. TOUSSAINT, M. GRÉDIAC, AND F. PIERRON, *The virtual fields method with piecewise virtual fields*, International Journal of Mechanical Sciences, 48 (2006), pp. 256 – 264.

[130] V. TVERGAARD, *Mechanical modelling of ductile fracture*, Meccanica, 26 (1991), pp. 11–16.

[131] V. TVERGAARD AND A. NEEDLEMAN, *Analysis of the cup-cone fracture in a round tensile bar*, Acta metallurgica, 32 (1984), pp. 157–169.

[132] E. VOCE, *The relationship between stress and strain for homogeneous deformations*, Journal of the Institute of Metals, 74 (1948), pp. 537–562.

[133] K. WASHIZU, *On the variational principles of elasticity and plasticity*, tech. rep., Massachusetts Inst. of Tech., Cambridge. Aeroelastic and Structures Research Lab, 1955.

[134] Z. WEI, X. DENG, M. A. SUTTON, J. YAN, C.-S. CHENG, AND P. ZAVATTIERI, *Modeling of mixed-mode crack growth in ductile thin sheets under combined in-plane and out-of-plane loading*, Engineering Fracture Mechanics, 78 (2011), pp. 3082–3101.

[135] L. XUE AND T. WIERZBICKI, *Ductile fracture initiation and propagation modeling using damage plasticity theory*, Engineering Fracture Mechanics, 75 (2008), pp. 3276 – 3293.

[136] Y. ZHANG, *Modélisation et simulation numérique robuste de l'endommagement ductile*, PhD thesis, Paris Sciences et Lettres, 2016.

[137] Y. ZHANG, E. LORENTZ, AND J. BESSON, *Ductile damage modelling with locking-free regularized gtn model*, International Journal for Numerical Methods in Engineering, (2017).

[138] Z. ZHANG, C. THAULOW, AND J. ØDEGÅRD, *A complete gurson model approach for ductile fracture*, Engineering Fracture Mechanics, 67 (2000), pp. 155 – 168.

Résumé

Cette thèse a pour objectif le développement d'une stratégie d'identification des paramètres de plasticité et d'endommagement jusqu'à amorçage, pour des métaux ductiles.
Un formalisme logarithmique est utilisé pour simuler les grandes déformations subies par les éprouvettes et une formulation non-locale multi-champ permet de simuler l'adoucissement indépendamment du maillage utilisé et d'éviter le verrouillage volumique.
La Corrélation d'Images Digitales est utilisée pour obtenir des mesures hétérogènes plein champ à partir d'éprouvettes entaillées.
La stratégie proposée s'appuie sur des observations microscopiques et sur une approche d'identification par recalage de modèle éléments finis (FEMU), visant à minimiser l'écart entre une mesure et son pendant simulé. L'écart est exprimé en termes de force et déplacement grâce à une normalisation appropriée. L'application de la FEMU est guidée par des analyses de sensibilité.
La robustesse de la comparaison essai-calcul est assurée par l'application de conditions au bord mesurées. L'effet négatif de l'incertitude de mesure est mis en évidence et une solution de filtrage innovante est proposée.
La stratégie est appliquée pour l'identification des paramètres de l'alliage Inconel625. Elle permet de reproduire l'amorçage pour des éprouvettes planes, en termes de réponse macroscopique et de localisation des sites d'amorçage.

Mots Clés

Endommagement ductile, FEMU, Identification des paramètres, Conditions au bord mesurées, Grandes déformations, Corrélation d'images digitales

Abstract

This thesis proposes an identification strategy for plastic behaviour and damage up to the onset of fracture, for an application to ductile metals.
A logarithmic finite strain formulation is used to simulate the large deformations undergone by the specimens, while a locking-free non-local formulation allows a mesh independent simulation of the softening behaviour.
Digital Image Correlation is used to obtain heterogeneous full-field measurements from tensile tests on notched specimens.
The identification strategy is based both on microscopic observations and on a Finite Element Model Updating (FEMU) technique, according to which the parameters are identified by minimizing the discrepancy between experiment and simulation. The discrepancy is quantified both in terms of displacement and force thanks to an appropriate normalization. The application of FEMU is guided using sensitivity analysis.
The robustness of the comparison between simulation and measurement is ensured by prescribing measured displacements as boundary conditions for the simulation. The negative effect of the measurement uncertainty is underlined, and an innovative filtering approach is proposed.
The proposed strategy is used to identify the materials' parameters of alloy Inconel625. It allows to reproduce the onset of fracture for flat specimens, both in terms of macroscopic response and crack initiation location.

Keywords

Ductile damage, FEMU, Parameter identification, Measured boundary conditions, Finite strain, Digital image correlation